KT-SCALE INTERACTIONS OF ETHYLENE OXIDE AND ZWITTERIONIC COPOLYMERS WITH BLOOD PROTEINS AND MUCUS

by
Eugenie Amjad Jumai'an

A dissertation submitted to Johns Hopkins University in conformity with the requirements for the degree of Doctor of Philosophy

Baltimore, Maryland

July 2022

ABSTRACT

Mucus linings and immune system protein coronas limit entry, targeting, and bioavailability of therapeutics. A common strategy to circumvent these barriers is to sterically stabilize therapeutics. This approach is based on fundamental work in colloid science but is often neglected in terms of mechanisms and interactions with biological macromolecules such as mucus and immune system proteins. A challenge is to understand polymer interactions and architectures in face of mucus and blood proteins to assess their stability to design colloidal therapeutics with enhanced bioavailability, safety, and targeting. In this dissertation, total internal reflection microscopy is used to directly, sensitively, and nonintrusively measure adsorbed PEG and zwitterionic (ZI) layer interactions against specific ions, proteins, and mucus. The use of TIRM offers kT-scale and nanometer resolution to offer unique insights needed for stabilizing colloidal therapeutics.

For the first goal, we report direct measurements of solution behaviour of adsorbed PEG and ZI triblock copolymers as a function of specific ions. Our findings indicate qualitatively different and unique behavior for each polymer, where: PEO layers are [NaCl] independent but collapse with increasing [MgSO4]; PMAPS layers extend with increasing [NaCl] but becomes less repulsive with increasing [MgSO4], and PMPC layers are completely insensitive to both salts. A competition between solvated molecular interactions and structures explains the unique response of each polymer to non-specific and specific ion effects.

For the second goal, we show how serum albumin and immunoglobin G, interact with PEG and ZI layers. Our results provide unambiguous evidence of exclusion of

proteins from adsorbed PEG. Low molecular weight zwitterionic coatings were displaced by both BSA and IgG unlike PEG. Measured interactions and corresponding exclusion states were fitted theoretically to reflect penetration and exclusion of both proteins.

Finally, we report kT-scale interactions of ZI and PEG coatings with mucin in various conditions such as low pH, mucolytic agents, and calcium chloride. Our results demonstrate that PEG and ZI coatings are repulsive towards mucin and provide a template for tuning polymer coatings to specifically adhere to mucus to achieve a balance of mucopenetration and mucoadhesion behavior for successful permeability through mucus.

Committee:

Prof. Michael A. Bevan (academic advisor, ChemBE)

Prof. Honggang Cui (ChemBE)

Prof. Chao Wang (ChemBE)

Prof. Howard Fairbrother (Chemistry)

Prof. Laura Ensign (School of Medicine)

ACKNOWLEDGEMENTS

Words are not enough to describe how grateful I am for my parents' and sister's unwavering love and guidance. You have set an example for success through honest work, integrity, respect, perseverance, and a dedication to upholding standards on how to treat others. I would not have achieved anything, personally or professionally, it wasn't for you. I also want to thank Nicolas, whose intellect, perspective, kindness, and devotion, have endowed me with support and love I couldn't imagine possible, and I look forward to supporting you when you finish your PhD and sharing more adventures with you for the rest of our lives. I'd like to thank the friends I made in my time at JHU and in Baltimore: Yorgos, my 707 sisters, Helya, Omkar, David, Seth, the Encrypted Lampshade, the Levantines, the Greeks, and my lab buddies Nikki, Luke, and Rachel.

I would like to thank my PhD advisor, Dr. Michael Bevan, who has given me a plethora of knowledge on polymer and interfacial science, colloidal interactions, guidance on thinking critically about my research, approaching problems with rigor without losing sight of the big picture, and helping me becoming an expert in my field (in addition to giving some good movie recommendations). Dr. Herrera-Alonso and her students, Elena Garcia, and Karla Hernandez, who have been excellent collaborators whose expertise has been instrumental for the richness of my dissertation. My annual review and thesis committee members who have offered insightful advice and feedback on project directions and further insights over the years. Bevan lab members, alumni, and present members, who have supported me with technical, personal, professional advice, 5 lb. buckets of animal crackers, and many coffee breaks.

TABLE OF CONTENTS

LIST OF FIGURES

1 INTRODUCTION

1.1 Background

Research in therapeutic delivery is concerned with strategies to increase transport rates across biological barriers such as the immune system (macrophage uptake and clearance), the mucosa, tissue barriers, and cellular trafficking, with the major goal of increasing and sustaining bioavailability of novel therapeutic materials.[1] The two primary barriers are the immune system proteins and mucosa that rapidly eliminate foreign particles and render novel therapeutics ineffective if cleared from the body or become tagged with new macromolecules that impede their targeting moieties.[2-5] Strategies to circumvent such barriers explore variations in surface chemistries, particle topology, particle morphology, and the use of more dynamic and novel materials.[1] However, there is not one solution to render therapeutics "stealthy" against the immune system protein response and the mucosal barrier; therefore, the persisting open engineering challenge is to develop a method to render colloidal therapeutics stable against aggregation, deposition, and recognition by the immune system.

Steric stabilization of colloidal therapeutics is considered an attractive solution for preventing therapeutics from nonspecific aggregation, deposition, and clearance by biological macromolecules.[6] A growing body of work has shown significant interest in utilizing nonionic, ethylene oxide polymer coatings, most notably poly(ethylene glycol) or PEG, that have been extensively characterized in terms of their solution behavior, thermodynamics,[7-8] promise for penetrating biological hydrogels,[9-10] and potential inertness to immune system responses.[11] However, conflicting reports of PEG coating often

challenge the notion that they possess "stealth' properties. Some studies have shown that PEG-coated particles may be toxic,[12-13] can induce an immune system response (seen most recently with the COVID vaccine),[14-15] and can adhere to mucus,[16] which impairs the ability of particles with such coatings to successfully permeate this barrier.

More promising polymers being explored are zwitterionic polymer coatings, which possess negatively and positively charged moieties on each repeat unit that are net neutral at a wide range of pH, and thus are stimuli responsive, adaptive materials.[17-20] Two commonly explored zwitterionic materials are phosphorylcholine and sulfobetaine polymers that are increasingly known for their superhydrophilicity, promise for true protein repellency properties (anti-fouling), and excellent biocompatibility.[20-24] These polymers with repeating dipoles offer significant advantages in terms of their solvation behavior and potential repellence to blood proteins compared to PEG. However, for both materials, conflicting reports of their efficacy create misconceptions and are closely related with the experimental assays used and their corresponding limitations, which limit our understanding of the mechanisms behind their solution behavior and thus impede our ability to tune properties to achieve true "stealth" against biological barriers.

Surveying the breadth of literature reveals two main categories of the state-of-the-art experimental techniques that have been used in attempt to probe steric coating behavior in presence of blood proteins and mucus. Indirect methods, which focus on spectroscopic techniques such as surface plasmon resonance (SPR)[25] and SDS-PAGE[26-27] offer statistical insights on macroscopic ensemble behavior of polymer coatings on nanoparticles with a wide array of biomaterials but can be intrusive experimentally and thus not representative of innate processes. Furthermore, these techniques encompass a range of limitations in

resolution which make understanding interactions at the level with molecular detail and thus can be subject to misinterpretations of data. More direct techniques such as surface force apparatus (SFA) and atomic force microscopy (AFM) offer substantially more sensitive probing/scanning advantages since they offer resolution of forces on the order of micro-Newtons and surface separation resolution on the order of nanometers.[28-29] However, the range of forces probed with these techniques is at least five-six orders of magnitude stronger than interactions that occur at the biological scale (~pN).[30-31] Often seen in literature, a combination of these techniques in used to understand polymer interactions with proteins and mucus, but there is not one technique so far that can offer a quantitative and sensitive analysis of these processes.

Therefore, an open challenge is finding an experimental technique that can offer the best of both scanning probe microscopy and spectroscopy: directness, sensitivity, scanning, statistics, and non-intrusiveness. A key aim is to use such a technique to develop a deeper understanding of the dimensions, architecture, and stability of polymer coatings and directly probe their interactions with blood proteins and mucus on the order of fN or ~kT. The goal is to use this understanding of colloidal interactions to reconcile misconceptions and guide the design of colloidal therapeutics that effectively and universally prevent nonspecific adhesion of blood proteins and can partition into and permeate the mucosal barrier.

In this dissertation, we establish the use of a direct, non-intrusive, and sensitive assay, Total Internal Reflection Microscopy (TIRM), to measure interactions and layer dimensions of adsorbed zwitterionic and PEG copolymers mediated by specific ions, presence of large abundant blood proteins, and against mucus layers. TIRM is a tool that

combines the best of nonintrusive, sensitive, and ensemble-averaged properties to measure colloidal interactions and layer dimensions. The experimental system involved measuring interactions between hydrophobic colloids and surfaces with adsorbed triblock copolymers with central poly(propylene oxide) (PPO) blocks and end blocks of the following: poly(ethylene oxide) (PEO), poly(3-(N-2-methacryloyloxyethyl-N,N-dimethyl) ammonatopropanesulfonate) (PMAPS), and poly(2-methacryloyloxyethyl phosphorylcholine) (PMPC). We compare their solution behavior when physiosorbed onto hydrophobic surfaces, since physisorption is an attractive, scalable, and simple technique for forming polymer brushes via lateral crowding for steric stabilization against aggregation and deposition.

Three-dimensional Brownian motion tracking of an ensemble of micron-sized colloidal probes above planar surfaces via video microscopy, and evanescent wave light scattering measuring motion normal to surfaces with nanometer resolution. Additionally, equilibrium analysis provides in situ, direct evidence of how the two most abundant blood proteins, serum albumin and IgG, at blood levels and solvated mucin layers interact with zwitterionic and PEG copolymers in varying solution conditions. Using this technique, we probe qualitative and quantitative differences in the behavior and stability of both coatings and reconcile the contradicting notions in literature about their interactions with biomacromolecules such as blood proteins and mucin networks.

1.2 Objective

This dissertation is devoted to several aspects of ethylene oxide and zwitterionic copolymer solution behavior and thermodynamics mediated by ion-specific effects, and the presence of blood proteins and mucins.

The first objective is to directly probe the dimensions, layer architectures, and interactions of zwitterionic copolymer coatings compared to PEG coatings in solutions of mono- and di-valent ions. Previous works focused on solution behavior of ethylene oxide polymers in NaCl solutions suggesting a nonspecific effect using monovalent ions. Additionally, zwitterionic polymers exhibit an antipolyelectrolyte effect with NaCl where their dimensions increase with increasing ionic strengths nonspecifically. A comparison on the use of specific ions that knowingly alter water structure and its effect on layer dimensions and interactions of zwitterionic polymer layers is examined via TIRM.

The second objective is to employ TIRM to measure PEG and zwitterionic copolymer layer dimensions and architectures mediated by the presence of high concentrations of blood proteins such as serum albumin and IgG. The goal is to examine how PEG and zwitterionic materials respond to blood proteins *in situ* and test what protein layer architectures are formed using a combination of experimentation and rigorous modeling of weak colloidal interactions.

The last objective is to measure asymmetric weak interactions between PEG and zwitterionic coated colloids and mucin layers to reconcile varying accounts on the degree of attractive or repulsive interactions between these materials in varying, physiologically relevant, solution conditions in situ.

1.3 Dissertation Overview

This dissertation is divided into chapters. *Chapter 2* reports specific ion mediated layer collapse of zwitterionic and PEG copolymers adsorbed on hydrophobic surfaces. We performed a series of measurements that include varying the amount of divalent specific ions such as MgSO4, which is known to break water structure, and NaCl to examine layer

thickness variations and its effect on symmetric layer interactions. By incorporating three-dimensional equilibrium trajectory analysis via evanescent wave scattering of microparticles and rigorous modeling of attractive and repulsive interactions of particle ensembles, we unveiled the well-known nonspecific effect of NaCl on PEG dimensions, the well-known anti-polyelectrolyte effect for PMAPS. Moreover, experiments revealed the dimensional collapse of PEG and PMAPS layers with increasing MgSO4, demonstrating a specific ion effect. Interesting enough, the other zwitterionic polymer used PMPC revealed a nonspecific effect with both NaCl and MgSO4, remaining highly extended in a wide range of mono- and di-valent ionic strengths. We used a superposition of attractive van der Waals and repulsive steric interactions to calculate layer thickness and observe a dimensional collapse. We found that the polymer layer collapse was mediated by polymer attraction at the periphery of the brushes. We concluded that a balance of entropic and enthalpic effects are responsible for the specific ion collapse of PEG and PMAPS whereas presumably the reversed dipole orientation of PMPC could be responsible for its outcompeting specific ions for solvation in water.

Chapter 3 reports the exclusion of blood proteins, serum albumin and immunoglobulin G from PEG layers. We systematically added and equilibrated physiological concentrations of albumin and IgG to a system of PEG-coated colloids and wall. We observed a systematic increase in the amount of exclusion of these proteins which lead to depletion-induced attraction between PEG layers. We used rigorous theoretical modeling to show that the thickness of PEG remained constant, indicating the lack of corona formation. We also developed a there=optical approximation of the exclusion or depletion of soft proteins from soft polymer layers by systematically adjusting the osmotic

pressure difference (partitioning) and the excluded volume (penetration of protein into polymer layer) from known theory. This work clearly shows that PEG does not form a corona with two abundant blood proteins but rather mediated exclusion of these proteins, weakened slightly by a dynamic, partial insertion of these proteins into PEG layers, consistent with theoretical models in literature.

Chapter 4 extends the previous study and reports the exclusion of blood proteins, serum albumin (BSA) from high molecular weight PMPC layers, but BSA corona formation on high molecular weight PMPC layers. IgG sequentially displaced both high molecular weight PMPC and PMAPS layers. Symmetric interaction measurements between low molecular weight PMPC and PMAPS layers confirms the moelcular0weight driven displacement by large blood proteins but highlights the importance and role of competitive molecular interactions (enthalpy) and entropic considerations as a potential explanation for these displacements. These results highlight that zwitterionic copolymers more easily desorb compared to the irreversible adsorption of PEG layers in face of blood proteins and arise from more complex interactions due to the complex structures of these zwitterionic species. However, our results suggest that chemically grafting zwitterionic copolymers might be competitive with PEG layers but require more direct and sensitive interaction measurements to compare their solution behavior.

Chapter 5 reports asymmetric interactions between PEG and zwitterionic coatings with adsorbed mucins, the most abundant component of mucus. We use total internal reflection microscopy (TIRM) to directly measure carrier-mucus interactions via direct kT-scale measurements of biomaterial interactions. We use our interaction measurements to probe polymer molecular weight and mucus networking effects by varying pH, calcium,

and adding mucolytic agents (Figure 1 G-I) to systematically and rigorously show that all these variations lead to net repulsive, weak interactions between the polymer coated colloid and mucin.

Chapter 6 reports the use of PEG-coated microparticles in a collaboration project to probe kT-scale energy landscapes on polymerized liquid crystal layers. A combination of video microscopy and inverse Monte Carlo simulations of concentrated diffusing colloids highlight the van der Waals energy landscape over liquid crystal defects and our results and analysis serve a basis for designing liquid crystal films for colloidal self-assembly.

Finally, *Chapter 7* summarizes major accomplishments and findings, and discuses several potential directions and outlooks.

2 SPECIFIC ION EFFECTS ON ADSORBED ZWITTERIONIC COPOLYMERS*

2.1 Abstract

We report direct measurements of interactions, dimensions, and solution behavior of adsorbed nonionic and zwitterionic triblock copolymers as a function of aqueous [NaCl] and [MgSO4] in the range 0-1M. Total internal reflection microscopy is used to measure kT and nanometer scale interactions between hydrophobic colloids and surfaces with adsorbed triblock copolymers with central poly(propylene oxide) (PPO) blocks and end blocks of: poly(ethylene oxide) (PEO), poly(3-(N-2-methacryloyloxyethyl-N,N-dimethyl) ammonatopropanesulfonate) (PMAPS), and poly(2-methacryloyloxyethyl phosphorylcholine) (PMPC). Findings indicate qualitatively different and unique behavior for each polymer, where: PEO layers are [NaCl] independent but collapse and become less repulsive and eventually attractive with increasing [MgSO4]; PMAPS layers are increasingly repulsive and extended with increasing [NaCl] but becomes less repulsive/extended with increasing [MgSO4], and PMPC layers are completely insensitive to both [NaCl] and [MgSO4]. A competition between solvated molecular interactions and structures appear to explain the unique response of each polymer to non-specific and specific ion effects as a function of aqueous salt solution composition.

2.2 Introduction

Polymers adsorbed to colloids and surfaces are commonly used to prevent aggregation with each other as well as other dispersed and solvated species in liquid media.[32-33] Colloidal particles with adsorbed polymers can also inhibit their deposition on biological[34-38] and synthetic[39-42] material substrates. The key mechanism to colloidal stabilization by adsorbed polymers is generation of net repulsive interactions in changing chemical and physical solution conditions. Repulsive interactions must be realized in diverse applications and material systems encountered in industrial formulations, the natural environment, and biomedical therapeutics and diagnostics. Using drug particles as an example, it is important to prevent drug particles from aggregating with each other or depositing on surfaces during their synthesis, processing, and storage, often with changing physicochemical conditions. In their application, drug particles are introduced into blood or mucus barriers, which requires stability against aggregation, adhesion to immune system species, and deposition on tissues.[43] In short, adsorbed layers have an essential role in colloidal particle synthesis, processing, storage, and performance in applications while encountering diverse physical and chemical conditions.

To engineer adsorbed polymers to stabilize colloidal particles, it is essential to understand how intra- and inter- molecular interactions between solvated polymers depend on solution conditions, or solvent quality.[32-33] Solvent quality is determined by the free energy of polymers in solution involving polymer segment and solvent interactions (enthalpy) and configurations (entropy). In addition, solvent quality is determined by temperature, pressure, and co-solutes that influence net interactions and favorability of configurations. In aqueous media, when polymer segments have favorable interactions

with water molecules *and* fit within water structure, solvent quality is "good", which yields: (1) net intra- and inter- molecular repulsion (*e.g.*, positive second virial coefficients), (2) expanded polymer dimensions (*e.g.*, increased radius of gyration), and (3) polymer solubility (*e.g.*, single phase solutions). Conversely, unfavorable changes to a solution's enthalpy or entropy (*i.e.*, "poor" solvent quality) leads to net attraction between polymers, dimensional collapse, and phase separation. Although adsorbed polymer thermodynamics are perturbed by interfacial interactions and configurations, net polymer interactions are still primarily determined by solvent quality.[44-45] In short, polymeric colloidal stabilization in aqueous media requires polymers that have favorable interactions with, and fit into the structure of, water while being insensitive to physical and chemical changes that can alter solvent quality.

Aqueous polymer solvent quality depends on polymer type and how they respond to changing solution conditions. For example, polyethylene oxide (PEO) is one of few alkylene oxide polymers that fit into water structure. Increasing or decreasing temperature changes water structure and decreases solvent quality and PEO solubility in water.[8, 39, 46] Although PEO is uncharged, and NaCl does not affect its solubility, it is well established that $MgSO_4$ causes PEO to become insoluble in water,[7] and renders it ineffective at stabilization of colloidal particles.[40, 47-48] $MgSO_4$ is often discussed in the context of the Hofmeister series[49-50] for salt induced protein aggregation via specific ion effects; such effects indicate ion-mediated behaviors that are not easily captured alone by electrostatic interactions independent of ion type.

Aqueous polyelectrolyte solution behavior is generally captured by considering screening of charge moieties,[51-52] where increasing salt screens intra-molecular repulsion

to decrease chain dimensions. In contrast, zwitterionic polymers have moieties with closely spaced cationic and anionic groups that are net neutral but have strong dipoles; these polymers often display the opposite trend where increasing salt screens intra-molecular dipolar attraction to increase chain dimensions (the "anti-polyelectrolyte effect").[53-65] _ENREF_34_ENREF_29 Although ion effects are documented for many aqueous neutral polymers and polyelectrolytes, significant gaps remain for understanding ion mediated polymer solvent quality and solution thermodynamics. However, for aqueous zwitterionic polymers, non-specific ion effects are still the subject of ongoing study,[64] and specific ion effects have only been investigated in a few preliminary studies with conflicting findings.[66-67]

Here, we report direct measurements of interactions between net neutral aqueous copolymers adsorbed to colloidal particles and planar substrates vs. [NaCl] and [$MgSO_4$] (**Fig. 2-1**). Systematic investigation of different polymer types provides a basis to understand how non-specific and specific ion effects determine polymer interactions, dimensions, phase behavior, and their role in colloidal stability. We investigate adsorbed triblock copolymers with different end blocks of PEO, PMAPS, and PMPC. Each end block is investigated based on its importance to biomedical applications and significant prior fundamental study,[23, 53, 68-72] which provides important benchmarks and open questions. While prior studies have investigated some specific ion dependent responses for certain polymers[67, 73-77]the systematic study in this work of changes in interactions and dimensions for different polymers and salts provides new information for each system as well as useful comparisons of qualitatively different responses. We employ total internal reflection microscopy (TIRM) to non-intrusively measure interactions of copolymers

adsorbed to colloids and surface with *kT*- and nm- scale resolution.[34-42] By using TIRM, our results provide a sensitive measurement of layer dimensions due to osmotic repulsion generated upon overlap of segments in the periphery of adsorbed layers.

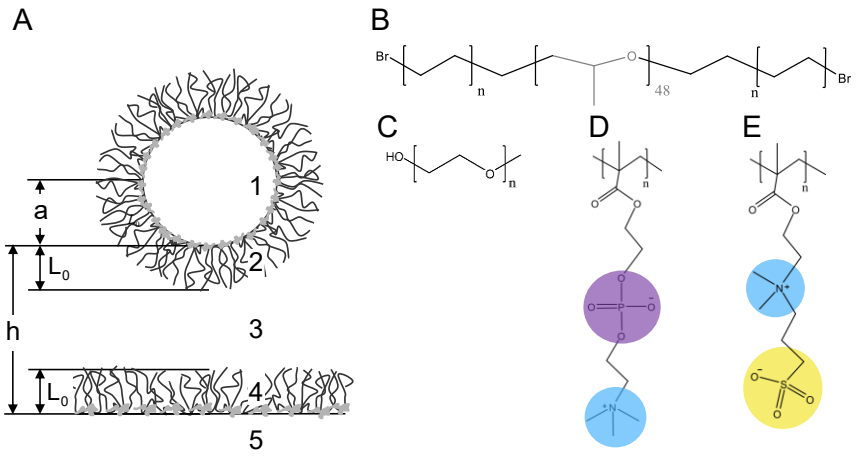

Figure 2-1 **Schematic for measurements of interactions between adsorbed copolymers on colloids and surfaces.** (A) Variables define dimensions, and numbers define materials: (1) hydrophobically modified silica colloids of radius, *a*, at a surface separation, *h*, from (5) a hydrophobically modified glass microscope slide, with both surfaces having (2,4) adsorbed triblock copolymers of thickness, L_0, in (3) aqueous NaCl and MgSO4 solutions. (B) Triblock copolymer architecture for three copolymers studied, all with a central PPO48 block, and blocks on either side, including: (C) neutral PEO_{148}, (D) zwitterionic $PMPC_{80}$, and (E) zwitterionic $PMAPS_{95}$. Throughout figures, groups are represented by: (purple) phosphate, (blue) amine, (yellow) sulfate, and (gray) insoluble PPO block.

2.3 Theory

2.3.1 Interaction Potentials

The net potential energy, u_N, for colloids interacting with a planar substrate can be given by a superposition of potentials due to van der Waals, u_V, steric, u_S, and gravity, u_G, as,[35, 42, 65]

$$u_N(h) = u_V(h) + u_S(h) + u_G(h) \tag{3.1}$$

where h is particle-wall separation (Fig. 1). The gravitational potential energy is given by,

$$u_G(h) = Gh$$
$$G = (4/3)\pi a^3(\rho_p - \rho_f)g \tag{3.2}$$

where G is buoyant particle weight, a is particle radius, ρ_p and ρ_f are particle and fluid densities, and g is acceleration due to gravity. The van der Waals interaction for a sphere and plate is,[78]

$$u_V(h) = 2\pi a \int_h^\infty \frac{-A(l)}{12\pi l^2} dl \tag{3.3}$$

where $A(l)$ can be obtained from Lifshitz theory[79] to include retardation and screening,[80] including for the silica colloids and glass substrates in this work.[81] Steric repulsion between adsorbed macromolecules can be modeled as,[35]

$$u_s(h) = \Gamma \exp(-\delta h) \tag{3.4}$$

where δ is a decay length, and Γ is obtained from fits (and models in some cases[82]).

2.4 Methods

2.4.1 Polymers

The commercial PEO_{141}-PPO_{51}-PEO_{141} (F108) copolymer (M_w/M_n=1.2[83]) was donated by BASF. The zwitterionic copolymers, $PMAPS_{95}$-PPO_{48}-$PMAPS_{95}$ (M_w/M_n=1.4) and $PMPC_{80}$-PPO_{48}-$PMPC_{80}$ (M_w/M_n=1.3), were synthesized using electron transfer-atom transfer radical polymerization (ARGET-ATRP) and characterized using NMR and static light scattering as described in our prior work.[42, 65] PMAPS indicates poly(3-(N-2-

methacryloyloxyethyl-N,N-dimethyl)ammonatopropanesulfonate) and PMPC indicates poly(2-methacryloyloxyethyl phosphorylcholine). Each copolymer is compactly referenced throughout the paper based on the end blocks as PEO, PMAPS, PMPC.

2.4.2 Colloids and Surfaces

Glass microscope slides (Fisher) were soaked in acetone, 100 mM KOH, rinsed with DI water, and dried with filtered clean dry air. Clean slides were rendered hydrophobic by spin coating a 3% w/w solution of polystyrene in toluene at 3000 RPM for 30 seconds. Silica colloids of nominal 2.2 μm, 3 μm, and 4 μm diameter (Bangs Laboratories) were rendered hydrophobic by coating with 1-octadecanol (Sigma-Aldrich) using a literature method.[84]

2.4.3 Polymer Adsorption

Polymer adsorbed layers on silica particles were adsorbed to silica particles by, first, dissolving the copolymers in good solvent conditions: PMAPS and PMPC at 1000 ppm in 100 mM NaCl and the PEO in DI. Hydrophobically modified silica colloids were added to each polymer solution and placed on a shaker for 4 hours. 1000 ppm copolymer solutions were added O-rings on polystyrene coated slides. The O-rings were sealed with glass coverslips for 4 hours. Free polymer was removed from particles and O-rings by 5 cycles of removal and addition of 100 mM NaCl with 30 ppm PMAPS and PMPC (to minimize desorption) and DI water for PEO. Finally, O-rings and particles were washed by 3 cycles in the final solution condition and allowed to equilibrate for 1 hour prior to measurements.

2.4.4 Total Internal Reflection Microscopy

Ensemble TIRM was used to measure interactions between polymer coated colloids and slide as described in previous work.[34-35] In summary, an evanescent wave is generated via reflection of a 633 nm HeNe laser (Melles Griot) onto a prism at 68 degrees. Images are captured using a 40× objective (LD Plan-NEOFLUAR), using a 12-bit CCD Camera (Hamamatsu Orca-ER) at 4 binning, 4 ms exposure, and a frame rate of 28 frames per second. In the TIRM experiment,[85-86] scattering intensity, I, of a spherical colloidal particle in an evanescent wave is used to determine relative particle-wall separation, h, as,[87] $h - h_m = \beta^{-1} \ln\left(I/I_m\right)$, where subscript *m* indicates the most probable value, and β^{-1} is the evanescent wave decay length (which depends on solution refractive index, which is a weak function of salt concentration). With a large enough number of observations, a histogram of measured heights, $p(h)$, can be inverted using Boltzmann's equation to obtain a measured potential energy profile, $u(h)$, as, $\frac{u(h)-u(h_m)}{kT} = \ln\left[\frac{p(h_m)}{p(h)}\right]$, measurements of single particle potentials are averaged to obtain ensemble average potentials.[85]

2.5 Results & Discussion

2.5.1 Adsorbed Polymer Interactions & Dimensions

In this work, we measured the interactions and layer dimensions of adsorbed nonionic and zwitterionic triblock copolymers as a function of aqueous [NaCl] and [$MgSO_4$]. The colloid-surface geometry and adsorbed triblock polymers are schematically illustrated (**Fig. 2-1A**) including triblock copolymer structures and compositions (**Figs. 2-**

1B). All polymers investigated contain a central insoluble PPO block of 48 repeat units. The soluble end blocks investigated in this work include PEO_{141}, as a benchmark nonionic polymer (**Fig. 2-1C**), as well as, zwitterionic blocks of $PMPC_{80}$ (**Fig. 2-1E**) and $PMAPS_{95}$ (**Fig. 2-1F**). TIRM is used to measure interactions and layer dimensions between layers physisorbed to colloids and surfaces vs. [NaCl] and [$MgSO_4$]. TIRM enables non-intrusive measurements of the three-dimensional Brownian motion of ensembles of colloids above surfaces via video microscopy to track lateral motion and evanescent wave light scatting to measure motion normal to surfaces with nanometer resolution. Such measurements are commonly used to obtain particle-wall interactions,[85] but can also be used to measure local binding events,[34-35, 37, 88] often due to heterogeneous surfaces. Example data from the current study shows how 3D trajectories show such local binding events **(Fig. 2-2A**), which can be excluded from analyses of particle-wall potentials. By measuring the equilibrium histogram of heights sampled by particles above surfaces, particle-wall interaction potentials are obtained (via Boltzmann's equation) with nm- and *kT*- resolution (**Fig. 2-2B**). By fitting measured potentials to well established theoretical models (Eq. 2-1) (**Fig. 2-2C**), the steric interactions between polymer layers are obtained to reveal their dimensions for given solution conditions (**Fig. 2-2D**).

Given the importance of steric interactions and layer dimensions in this work, we provide more detail of the analysis using the specific example (**Fig. 2-2**), which is applied in the same manner for all measurements in this work. Based on the superposition of interactions, the steric interaction is obtained in each case by subtracting the gravitational potential energy and van der Waal interactions. These potentials have been extensively measured and modeled, so that gravity is easily subtracted as a simple linear function with

no adjustable parameters, and van der Waals is subtracted based on prior measurements and rigorous models[39, 42, 65, 78, 81, 89] to obtain the absolute particle-wall surface separation. Given the simplicity of subtracting the linear gravitational potential, and since it is due to body force that is easily separable from colloidal and macromolecular interactions, the remainder of profiles are shown without gravity.

The adsorbed polymer layer thickness, L_0, on the particle and wall surfaces is taken to be half the surface separation at which the onset of steric repulsion is observed (~0.1kT repulsion). This provides a kT-scale measurement of layer thicknesses due to osmotic repulsion generated by the very initial overlap of segments in the periphery of adsorbed layers. It should be noted that the ionic strength of all of the measurements in this study causes electrostatic double layer repulsion to be much shorter range than the measured steric interactions. For the example in **Fig. 2-2**, the most probable particle-wall surface separation when including all interactions is 38 nm (**Fig. 2-2C**), and after gravity and van der Waals are subtracted, the PMAPS layer thickness is found to be L_0= 22 nm in 0.05M NaCl (**Fig. 2-2D**). This example illustrates the analysis used to model interactions and layer dimensions for all measurements in this work.

2.5.2 Adsorbed Polymer Interactions vs. [NaCl]

To establish a baseline before investigating $MgSO_4$ that is known to introduce specific ion effects, we first measured layer dimensions of adsorbed copolymers vs. [NaCl] (**Fig. 2-3A-C**). For adsorbed PEO copolymer interactions in [NaCl] = 0.05-1M, the range and form of the repulsive interactions shows no observable dependence on [NaCl] in the range tested (**Fig. 2-3A**). The range of the steric interactions reveals the adsorbed layer

thickness was found to be L_0 = 20 nm for all [NaCl] concentrations. Such behavior is consistent with NaCl not showing specific ion effects on the dimensions or interactions of PEO chains. There also does not appear to be any non-specific ion effects associated with electrostatic interactions, which is expected since PEO is nonionic. We next report measurements of adsorbed PMAPS interactions on two different sized colloids in the same range of in [NaCl] = 0.05-1M NaCl (**Fig. 2-3B**). Below 0.05M NaCl, particles with adsorbed PMAPS deposit on surfaces with adsorbed PMAPS, which indicates net attraction between the layers rather a repulsive stabilizing interaction. This finding is also consistent with prior and literature results showing PMAPS to be insoluble at such low [NaCl].[53, 56, 66] In the range of 0.05-0.15 M NaCl, using 2 μm colloidal probes, the range of the repulsion increases with

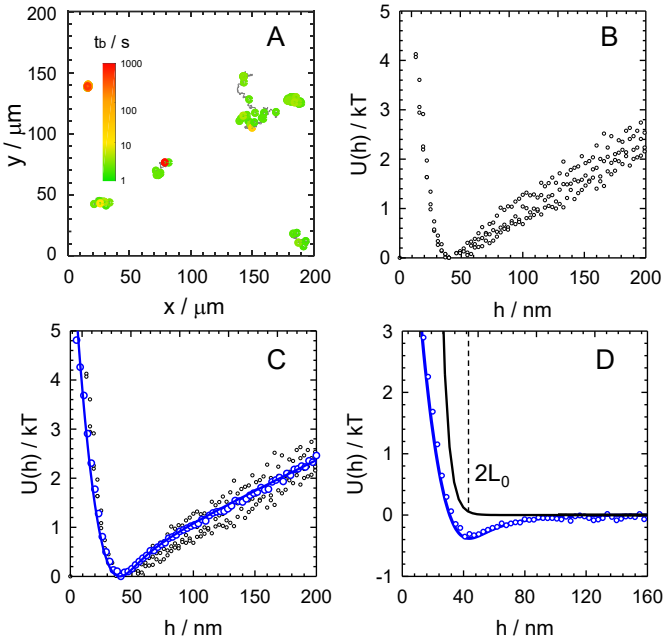

Figure 2-2 **Colloidal trajectories on surfaces resolve kT- and nm- scale interactions.** (A) 2D trajectories of 2 µm silica colloids with adsorbed PMAPS in 50 mM NaCl, where color indicates binding lifetimes. (B) Single particle potential energy profiles for particles with only short binding lifetimes. (C) Ensemble average potential energy profile (blue points) fit to theoretical potential, which is convoluted using a Gaussian kernel to include measurement noise.[42] (D) Net potential with gravity subtracted and steric repulsion shown separately. The separation for contact of two layers is marked as $2L_0$ when the steric repulsion decays to $0.1kT$.

increasing ionic strength, which correspond to a small but consistent increase in L_0 from 21 to 23 nm. At the highest concentration of 0.3M NaCl, using a 3 µm colloid with longer range van der Waals, the layer thickness remains at $L_0 = 23$ nm. These results are consistent with an "anti-polyelectrolyte" effect, where zwitterionic PMAPS chains swell with increasing NaCl concentration from being initially insoluble in deionized water.[53-54] The anti-polyelectrolyte effect is a non-specific ion effect; it is understood as screening of electrostatic attraction between dipolar zwitterionic groups, which does not depend on ion identity but only its charge sign and valence.

The third copolymer in this work, PMPC, was also measured with TIRM to quantify interactions and layer dimensions over the same NaCl range as the PEO and PMAPS copolymers. A repulsive interaction between adsorbed PMPC layers is observed, which

does not change in either shape or range for [NaCl] = 0.05-1M NaCl (**Fig. 2-3C**). The layer dimension is found in all cases to be $2L_0$ = 42 nm. In contrast to PMAPS, we also found the PMPC copolymer to be soluble and produce similar layers dimensions at lower ionic strengths (<0.05M NaCl). The observed [NaCl] independence of PMPC dimensions and interactions is consistent with our prior results and literature studies, where PMPC does not display an anti-polyelectrolyte effect. As short, PMPC does not display non-specific ion effects in the presence of NaCl like PEO, although it seems it should display anti-polyelectrolyte effects like PMAPS based on both being zwitterionic polymers.

The different [NaCl] dependent interactions and dimensions of three net-neutral copolymers suggests the importance of investigating how such polymers respond to a salt that is well established to show specific ion effects. Given that specific ion effects can influence solvent, segment, and ion interactions and entropy in solvated polymer chains, comparison, and contrast with NaCl dependent interactions and dimensions may provide new insights.

2.5.3 Adsorbed Polymer Interactions vs. [NaCl] & [$MgSO_4$]

Using the NaCl results as a foundation, we now add [$MgSO_4$] to [NaCl] background levels already tested in the prior section (**Fig. 2-3D-F**). Practically, in each salt composition, the ionic strength of NaCl was kept constant at the same value in **Fig. 2-3A-C**, and $MgSO_4$ was added to understand its role in addition to NaCl. Based on our prior work on adding $MgSO_4$ to adsorbed PEO layers,[40, 48] we first added 0.3M $MgSO_4$ and 0.05M NaCl to adsorbed PEO copolymers (**Fig. 2-3D),** which results in stronger van der Waals attraction (~0.7kT) compared to only NaCl (~0.5kT) (**Fig. 2-3A**) and a shorter-range

repulsive interactions between PEO layers. A 5 nm reduction in the range of repulsion corresponds to a 2.5 nm dimensional collapse of each adsorbed layer. Increasing to 0.4M $MgSO_4$ and 0.05M NaCl causes particles to deposit on the wall due to attraction between adsorbed PEO layers as a result of poor solvent quality. $MgSO_4$ clearly has a dramatic effect on PEO interactions compared to a complete insensitivity to NaCl, which is consistent with the well-known specific ion effects of $MgSO_4$ on aqueous PEO phase behavior.

Next, we add $MgSO_4$ and NaCl to adsorbed PMAPS copolymers (**Fig. 2-3E**). For PMAPS, a significant range in the reduction of repulsion, and corresponding dimensional collapse, occurs in 0.05M NaCl by adding only 0.005M $MgS0_4$. The layer collapses from $2L_0$ = 43 nm (Fig. 2-3B) to 32 nm (Fig. 2-3E). This is a much larger relative dimensional collapse for PMAPS compared to PEO with a much smaller change in [$MgSO_4$]. However, when adding 0.1M $MgS0_4$ to 0.3M NaCl, the dimensional collapse is much smaller from $2L_0$ = 46 nm to 40 nm. These results show that as more NaCl is added to PMAPS layers, which causes them to expand, more $MgSO_4$ is required to make them collapse. This shows that while NaCl mediates a non-specific ion effect of screening zwitterionic dipolar attraction to produce chain expansion (via the anti-polyelectrolyte effect), $MgSO_4$ causes a layer collapse in PMAPS similar to its effect on PEO. In short, PMAPS displays a non-specific ion dependent response to NaCl, and a specific ion dependent response to $MgSO_4$. While screening zwitterionic dipolar interactions explains the different NaCl dependent behavior of PMAPS and PEO, both polymers collapse and eventually exhibit polymeric attraction in poor solvent conditions due to added $MgSO_4$.

In contrast to both nonionic PEO and zwitterionic PMAPS copolymers, adsorbed

zwitterionic PMPC interactions and dimensions are completely insensitive to all compositions of [NaCl] and [$MgSO_4$] investigated in this work. Practically, there was no change in the functional form or range of the repulsion between adsorbed PMPC layers for [NaCl] = 0.05-1M and [$MgSO_4$] = 0.05-1M (including combined 1M NaCl and 1M $MgSO_4$). The PMPC copolymer does not show classic screening of zwitterionic dipolar interactions, which is a non-specific electrostatic interaction, nor does it show classic specific ion effects exhibited by both nonionic PEO and zwitterionic PMAPS copolymers in the presence of $MgSO_4$. These results demonstrate the unique properties of PMPC, and raise fundamental questions about the mechanisms of specific ion effects in aqueous macromolecular solution behavior.

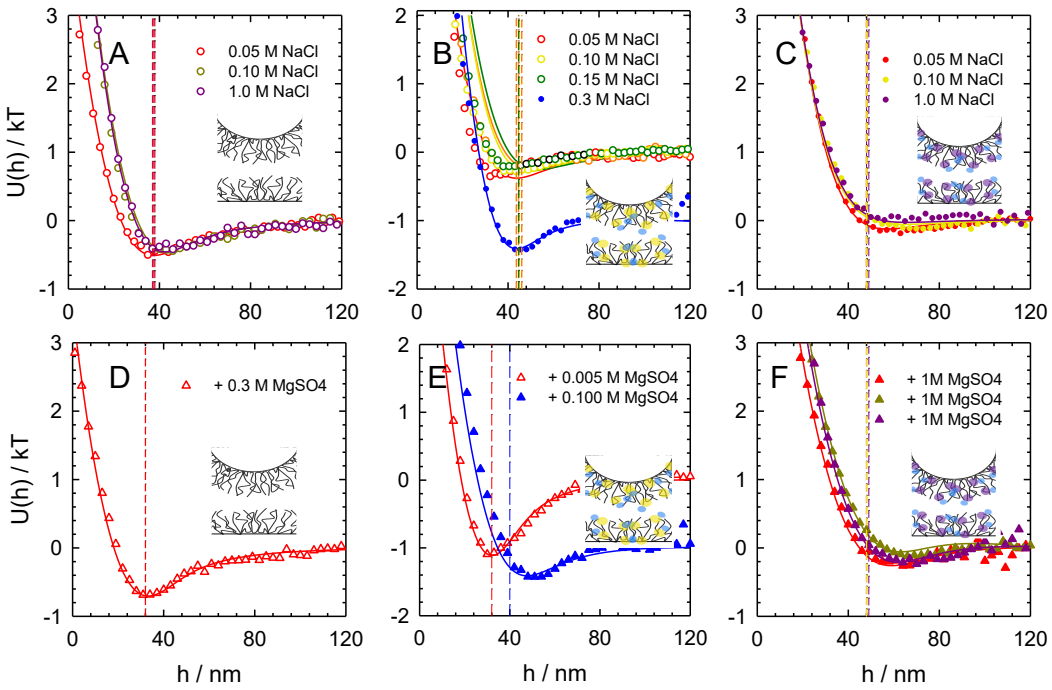

Figure 2-3 **Potential energy profiles for adsorbed copolymers interactions vs. [NaCl] and [$MgSO_4$].** Inset legends indicate: (circles) [NaCl], (triangles) [$MgSO_4$] added to [NaCl] with same color circle, (open symbols) 2um colloids, (filled symbols) 4um colloids. Dashed lines indicate $2L_0$. Interactions vs. [NaCl] between adsorbed copolymers of: (A) PEO, (B) PMAPS, and (C) PMPC. Interactions vs. [NaCl] + [$MgSO_4$] between adsorbed copolymers of: (D) PEO, (E) PMAPS, and (F) PMPC

2.5.4 Adsorbed Layer Dimensions and Phase Behavior vs. [NaCl] and [$MgSO_4$]

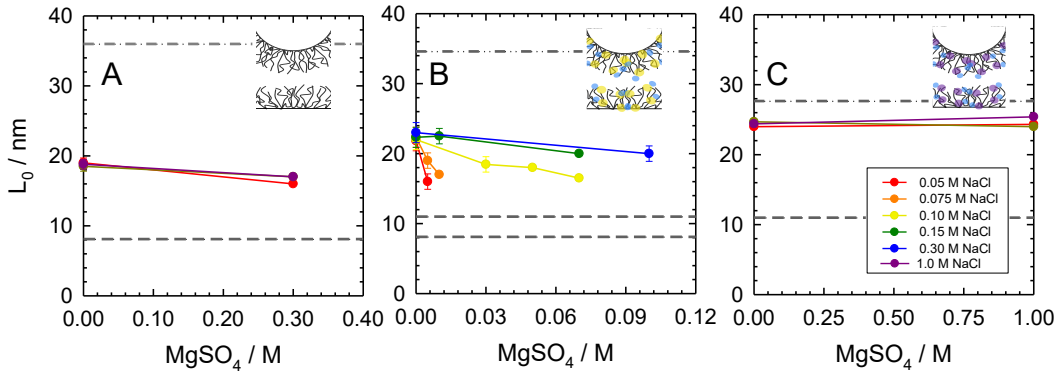

Figure 2-4 **Summary of adsorbed copolymer layer dimensions (steric thickness) vs. [NaCl] and [$MgSO_4$].** Layer thicknesses from onset of steric repulsion determined from Fig. 3, for interactions of adsorbed copolymers of: (A) PEO, (B) PMAPS, and (C) PMPC. The inset legend gives [NaCl], which matches the color scheme used in all other figures. The contour length (weight-averaged molecular weight to account for polydispersity) is shown for each end block (dash-dot). The particle-wall surface separations for 5kT of van der Waals attraction (dashed) for 2um and 4um colloids indicates the minimum layer thickness when particles would deposit on the wall in the presence of layers with repulsive interactions. Error bars are shown for three measurements.

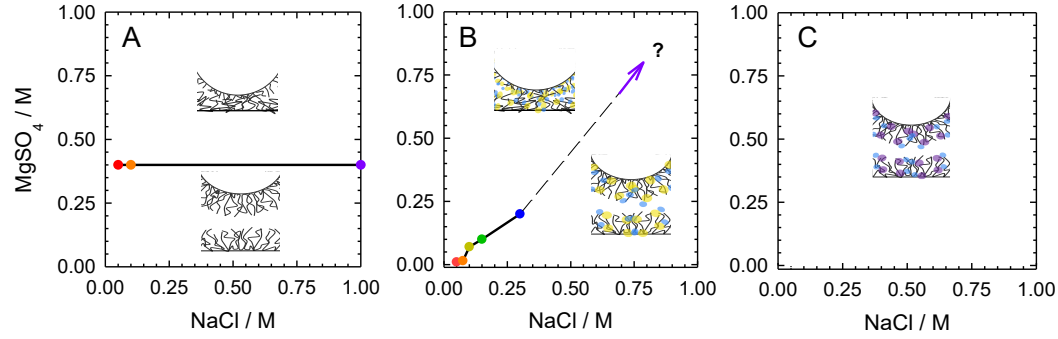

Figure 2-5 **State diagram of aqueous [NaCl] and [$MgSO_4$] compositions when adsorbed copolymer layers are either repulsive/extended or attractive/collapsed.** Colored points correspond to compositions measured in Fig. 3 for: (A) PEO, which has no NaCl dependence, (B) PMAPS, which depends on both NaCl and MgSO4 (where dashed line indicates uncertainty in how far this trend persists), and (C) PMPC, which has repulsive layers for all compositions investigated.

From direct measurements of separation dependent interactions between adsorbed layers in **Fig. 2-3**, we now summarize [NaCl] and [$MgSO_4$] dependent layer dimensions and solution behavior. The layer dimensions, L_0, of PEO, PMAPS, and PMPC copolymers are summarized for the measured $MgSO_4$/NaCl compositions (in **Fig. 2-3**) along with the

contour length for reference in each case (**Fig. 2-4**). The PEO copolymer layer thickness is essentially unchanged for [NaCl] in the range between 0.05-1M. However, the same layers contracts by ~2 nm, or from 60% to 53% of the contour length, when 0.3M $MgSO_4$ is added (**Fig. 2-4A**). For [$MgSO_4$] > 0.3M, PEO layers experience a net attraction and the particle deposits on the wall, which is also expected to correspond to phase separation of such chains in solution (**Fig. 2-5A**).

Adsorbed PMAPS copolymers display a rich and complex dependence on both [NaCl] and [$MgSO_4$] (**Fig. 2-4B**). In the absence of $MgSO_4$, the layers expand by a couple nm to produce highly stretched configurations that are ~90% of the contour length. A small proportion of polydisperse chains within the adsorbed layer might produce the thicker layers and provide some explanation of the significant extension approaching the contour length.[65] Because PMAPS chains are insoluble below 0.05M NaCl, and are then highly extended at higher [NaCl], it is clear they undergo expansion in NaCl, consistent with literature results.[60] However, the anti-polyelectrolyte effect saturates in this [NaCl] range since chains cannot easily extend further, which is consistent with literature studies indicating zwitterionic polymers reaching a threshold extension.[66]

In [NaCl] and [$MgSO_4$] mixtures, PMAPS layers collapse with increasing [$MgSO_4$], but the degree of the collapse depends on [NaCl] (**Fig. 2-4B**). This is apparent from the fact that the [$MgSO_4$] required to collapse layers to the same extent increases as [NaCl] increases. For example, PMAPS layers collapse by: (i) ~6 nm when 0.005M $MgSO_4$ is added to 0.05 M NaCl, (ii) ~5 nm when 0.07M $MgSO_4$ is added to 0.1 M NaCl, and (iii) ~4 nm when 0.1M $MgSO_4$ is added to 0.3 M NaCl. These data show an order of magnitude higher [$MgSO_4$] is needed to achieve similar collapses for doubling [NaCl] at low

concentrations, although the effect saturates at higher [NaCl]. In each case, PMAPS layers collapse from ~90% of their contour length to ~60-80% of their contour length before the adsorbed layers become attractive and the particles deposits on the substrate. PMAPS dimensions depend on both [NaCl] and [$MgSO_4$], which contrasts PEO layers that depend on [$MgSO_4$] but are independent of [NaCl].

Further increasing [$MgSO_4$] at fixed [NaCl] for PMAPS beyond the terminal points of each curve in Fig. 4B cause particles to deposit, which indicates attraction between layers. The last measured layer thickness in each case is well beyond the range of the particle-substrate van der Waals attraction (dashed lines in Fig. 2-4) in all cases, and only a slight addition of [$MgSO_4$] beyond the last point immediately caused particle deposition. Based on these observations, the deposition appears to occur as the result of attraction between PMAPS chains on opposing surfaces rather than a large sudden first-order transition in the layer dimensions that would suddenly allow a large van der Waals attraction between the particle and substrate. Based on this interpretation, we summarize the combinations of [$MgSO_4$] and [NaCl] (**Fig. 2-5B**) that lead to effective phase separation of PMAPS chains via a net intermolecular interaction. This plot clearly illustrates a competition between [$MgSO_4$] and [NaCl], where more [NaCl] appears to favor adsorbed PMAPS solubility and layer expansion, which then requires increasingly high concentration of [$MgSO_4$] to collapse such layers and cause phase separation.

The highly extended dimensions of adsorbed PMPC layers are insensitive to the entire range of [$MgSO_4$] and [NaCl] investigated. Practically, for all concentrations of both salts up to 1M, the adsorbed PMPC layers are extended to ~85% of their contour length computed from the weight-averaged molecular weight (to consider longer chains based on

the polydispersity) (**Fig. 2-4C**). In addition, interactions between adsorbed layers were purely repulsive for all conditions (**Fig. 2-3C**), which also corresponds to a single-phase stable solution for all conditions (**Fig. 2-5C**). Although the insensitivity of PMPC to [NaCl] has been well documented, the insensitivity to [$MgSO_4$] as well as [$MgSO_4$] and [NaCl] mixtures is new and surprising.

2.5.5 Adsorbed Layer Interactions and Phase Behavior

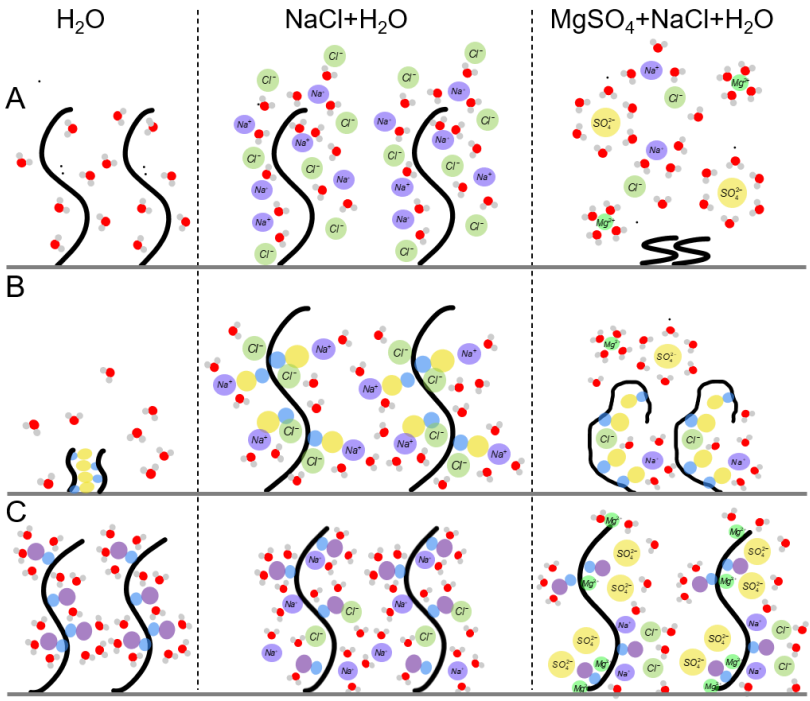

Figure 2-6 **Schematic representations of specific and nonspecific ion effects on adsorbed copolymers inferred from measurements of interactions and layer dimensions**. Schematics are shown for adsorbed copolymers of: (A) PEO, (B) PMAPS, and (C) PMPC. See text for discussion of schematics.

The qualitatively different responses of PEO, PMAPS, and PMPC layer dimensions, interactions, and phase behavior in [$MgSO_4$] and [NaCl] mixtures are not obvious and require a molecular explanation. Several molecular mechanisms must be considered including electrostatic and dipolar interactions as well as entropy of solvated

structures. While we do not directly measure molecular interactions, our *kT*- and nm- scale measurements of macromolecular interactions and dimensions for a series of aqueous neutral polymers with very different behaviors provides a unique data set for understanding molecular mechanisms in a consistent manner.

PEO homopolymer and copolymer thermodynamic solution behavior is generally well documented as depending on the ability of repeat units to favorable fit within water structure[90] (**Fig. 2-6Ai**). This concept is used to understand the solubility of PEO in aqueous media in contrast to nearly all other alkylene oxide polymers (based on molecular structure), as well as, the lower critical solution temperature behavior of PEO solutions (based on thermal expansion of water structure).[8] It is also understood that because NaCl does not have electrostatic interactions with PEO segments in aqueous media, and it does not significantly affect water structure in the presence of PEO (*e.g.*, relatively small positive molar volume and negative entropy of hydration[91]),[7, 92] _ENREF_61 NaCl has essentially no influence on PEO solubility (**Fig. 2-6Aii**).

However, in the presence of $MgSO_4$, PEO is known to phase separate (**Fig. 2-6Aiii**), which is considered to result from $MgSO_4$ altering water structure not unlike thermal effects on water structure and PEO solubility.[40] In short, NaCl does not have any effect on PEO (non-specific or specific), whereas $MgSO_4$ has a specific ion effect by changing water structure (*e.g.*, negative partial molar volume, relatively large negative entropy of hydration[91]), which is thought to compete with PEO solubility. This understanding of PEO solubility in the presence of NaCl and $MgSO_4$ is consistent with our direct measurements of layer interactions, dimensions, and phase behavior (**Figs. 2-3A to 2-5A**) and provides a basis for comparison and contrast with zwitterionic PMAPS and PMPC polymers.

PMAPS polymers are well known to display the anti-polyelectrolyte effect common in zwitterionic polymers. Whereas polyelectrolytes contract with increasing [NaCl] due to screening intramolecular electrostatic repulsion between single charge moieties (monopoles), zwitterionic polymers expand with increasing [NaCl] due to screening intramolecular electrostatic attraction between zwitterionic moieties (dipoles).[63] It should be noted that the relatively weak PEO monomer backbone dipole (1.04 D[93]) does not display any such anti-polyelectrolyte effect and [NaCl] dependence. PMAPS sulfobetaine moieties have significant dipole moments (24.9 D[94]), which when screened should increase chain dimensions, net intra- and inter- molecular repulsion, and solubility. These trends are indeed observed with increasing [NaCl] in this work (Figs. 2-3 to 2-5B, **Figs. 2-6Bi,ii**), where chains are insoluble in the absence of NaCl, and then expand and increase their range of repulsion at higher [NaCl]. These observations are consistent with prior measurements of both unadsorbed and adsorbed/grafted chain dimensions, interactions, and solubility.[56, 65, 95] In short, the [NaCl] dependent behavior of adsorbed PMAPS layers is a non-specific ion effect described by electrostatic interactions independent of ion type.

Adding $MgSO_4$ to adsorbed PMAPS layers causes them to collapse like PEO, but in a manner that also depends on [NaCl] (Figs. 3-5B, **Figs. 2-6Biii**), suggesting a competition between two effects. The anti-polyelectrolyte effect that increases PMAPS dimensions, interactions, and solubility with increasing [NaCl] is reversed by adding $MgSO_4$ in increasing proportion to the amount of NaCl present (Fig. 2-5B). Because $MgSO_4$ does not appear to contribute to the anti-polyelectrolyte effect, but instead decreases solubility as it does for PEO, it appears to have a similar specific ion effect in

the case of PMAPS. The obvious simplest explanation is that $MgSO_4$ changes water structure and PMAPS solubility as it does for PEO, only now it competes with the anti-polyelectrolyte effect, which was not important for PEO. Although $MgSO_4$ could interact with dipolar zwitterionic moieties or affect entropy of solvated structures beyond water structure, introduction of additional concepts is not obviously necessary to explain the PMAPS results or warranted by information accessible in our measurements of layer interactions and dimensions.

Adsorbed PMPC copolymer layers do not change interactions, dimensions, or solubility for the broad range of [$MgSO_4$] and [NaCl] mixtures investigated (**Fig. 2-6C**), with is different from both PEO and PMAPS and therefore requires consideration of different molecular mechanisms. Although the insensitivity of PMPC to [NaCl] is well known,[53, 71, 96] its insensitivity to [$MgSO_4$] has not been reported before to our knowledge. The phosphorylcholine (PC) moiety on PMPC has a dipole moment (21.30 D[97]) significantly higher (>20x) than PEO and somewhat smaller (~85%) than PMAPS, but this similarity alone does not lead to the common anti-polyelectrolyte effect. However, switching the PC moiety orientation on the polymer backbone has been shown to yield common anti-polyelectrolyte behavior (like PMAPS),[98] which indicates the importance of local molecular structure beyond simple non-specific screening of dipolar attraction.

The [$MgSO_4$] independence of all PMPC adsorbed copolymer properties provides additional insights into aqueous PMPC behavior. [$MgSO_4$] does not produce anti-polyelectrolyte behavior in PMPC, so there are no obvious non-specific ion effects, or electrostatic screening, with either salt. [$MgSO_4$] in the range 0-1M also does not produce any detectable dimensional collapse of PMPC, which is also a significant departure from

its effect on both PEO and PMAPS. As a result, the typical mechanism of $MgSO_4$ altering water structure in a manner that competes with polymer solubility appears to be compensated for by another mechanism. For comparison, other solutes such as ethanol have been shown to render PMPC insoluble in aqueous solutions,[99] which is attributed to a favorable enthalpy decrease due to formation of water-ethanol hydrogen bonds. Because changing PMPC structure by switching PC orientation can induce an anti-polyelectrolyte effect with other salts, and aqueous PMPC solubility can be altered by adding other competitive solutes like ethanol, the solvated molecular structure of PMPC and its competitive interactions with water and $MgSO_4$ appear to be unique. It seems solvation of PC moieties by water dominate dipolar screening, altered water structure, and competitive solute-water interactions. Whether the solvation of PMPC by water molecules dominates other effects by entropic (structural) or enthalpic (interaction) contributions is difficult to surmise from our data.

2.6 Conclusions

By comparing and contrasting our direct measurements of PEO, PMAPS, and PMPC copolymer layer interactions, dimensions, and phase behavior, our findings provide new insights into what mechanisms contribute to the thermodynamic solution behavior of each polymer. As a benchmark, the adsorbed PEO copolymer follows established expectations in its [NaCl] independence because it is nonionic and its [$MgSO_4$] dependence because of competing interactions and water structure changes. Likewise, adsorbed PMAPS displays a weak anti-polyelectrolyte effect with increasing [NaCl], which is consistent with bulk and grafted PMAPS measurements. The specific ion effects associated with the [$MgSO_4$] dependence of PMAPS has not been previously reported, but appear to

be somewhat similar to underlying mechanisms for PEO; the main difference being that PMAPS chains collapse via a specific ion-mediated [$MgSO_4$] dependence that competes with chain expansion via a nonspecific ion mediated [NaCl] dependent anti-polyelectrolyte effect. Finally, PMPC adsorbed layers displays no obvious dependence on either and [NaCl] or [$MgSO_4$], which suggests no contributions from non-specific or specific ion effects that influence PEO and PMAPS. Based on our results in conjunction with literature evidence, it seems that solvation of PC moieties on PMPC, involving possibly both PC-water interactions and structure, must dominate all other interactions to maintain consistent PMPC interactions and dimensions independent of [NaCl] or [$MgSO_4$]. Ultimately, these results provide a better understanding of aqueous polymer solution thermodynamics and solvent quality mediated macromolecular interactions important to diverse materials and applications.

3 BLOOD PROTEIN EXCLUSION FROM PEG BRUSHES

3.1 Abstract

Proteins are a critical element of the immune system response to foreign particles via adsorption, or formation of a "corona". Polymer coatings on particles with repulsive interactions towards proteins provide a potential mechanism for particles to evade detection by the immune system. Current methods to interrogate protein coronas are often expected to perturb weakly bound proteins, which perhaps provides some explanation for conflicting results from different assays. We present findings on *kT*-scale measurements of how the most abundant serum proteins, serum albumin and immunoglobin G, interact with PEG copolymers adsorbed to hydrophobic colloids and surfaces. Specifically, we use total internal reflection microscopy (TIRM) to directly and sensitively resolve interactions mediated by proteins, at blood concentrations, with nanometer- and *kT*- scale resolution. Given that different protein mediated interactions are mutually exclusive, our results provide unambiguous evidence of exclusion of proteins from adsorbed PEG layers, and the absence of protein corona. Measured interactions and corresponding exclusion states are fitted theoretically using two adjustable parameters reflecting the degree of penetration and exclusion of both proteins from adsorbed layers of PEG. These findings demonstrate a direct, sensitive, and non-intrusive measurement of protein mediated colloidal interactions as a probe of protein-polymer interactions with implications for immune responses to different polymer coatings adsorbed to colloidal particles.

3.2 Introduction

Nonspecific protein adsorption on surfaces is regarded as a key challenge in the development of high-performance devices in the marine industry, biotechnology, healthcare, and energy.[100] in the biomedical field, there is a significant body of literature suggesting that a complex mixture of blood proteins trigger an immune system response to foreign particles by adsorbing on the surface of these particles forming a "corona" which may affect hemolysis, activation of thrombocytes, and activating intracellular pathways leading to the release of inflammatory cytokines. [3, 25, 101-102] while several studies indicate the presence of protein corona, there is no consensus on how adsorbed proteins affect immune system stimuli. Current explanations include blood proteins stimulate or mitigate the immune response by: (a) modulating innate immune cell activity, (b) triggering the complement cascade, and (c) stimulating adaptive immune responses.[103] owing to the importance of evading the immune system response and its complexity in its composition, the key challenge is to design novel nanomaterials that resist nonspecific protein adsorption, i.e., design "stealthy" nanomaterials, without ignoring the complexity and heterogeneity of blood.[102] successful design of these nanomaterials relies on accurately elucidating the mechanisms of formation of protein coronas and understand the interactions that govern the immune system response towards foreign nanomaterials.

Polyethyleneglycol, or PEG, has been regarded as the 'gold standard' in stealth coatings on drug particle formulations owing to its biocompatibility and antifouling properties.[104] The unusual property of PEG as a surface that exhibits a net repulsion with proteins has been linked to the presumed biological inertness of the polymer

backbone and to its solvated configuration. Efforts to elucidate the phase behavior of PEG in its solvated states, either free in solution or physiosorbed, as a function of solvent quality has been characterized previously [42, 105-107] and PEG was found to be one of few alkylene oxide polymers that fits into water structure. Increasing or decreasing the temperature changes water structure and decreases the solvent quality and PEO solubility in water, however PEG's solvated structure does not change with changing concentrations of NaCl.[106] There is a prevalence of literature that shows that PEG-coated surfaces resist adsorption of proteins in the blood associated with the immune system responding to foreign particles, making PEG an attractive option for increasing bioavailability of drug particles in blood.[11, 108] However, neutron reflectometry evidence shows peculiar behavior of PEG interacting favorably with proteins in solution,[109-113] and some studies show that PEG may help with protein folding through binding unfolded proteins and perhaps functioning as chaperones, by preventing aggregation and facilitating refolding. [114-116] Additionally, several key works [117] [118] have shown that PEG relies on adsorption of a combination of plasma proteins to evade the immune system and remain bioavailable. Therefore, there is a trend in current literature that shows that PEGylated particles rely on selective adsorption of proteins to evade uptake and elimination from the blood versus the previous notion that PEG resists protein adsorption all together, suggesting more complicated protein interactions with PEGylated surfaces.

Serum albumin and immunoglobulin proteins are the most abundant proteins in blood with significant roles in the immune system response. Proteins, such as albumin and apolipoproteins called dysopsonins, aid evasion of phagocytosis while proteins, such as immunoglobulins and complement proteins called opsonins, promote phagocytosis.[119]

Serum albumin and PEG interact in such a way that the protein will concentrate in PEG-rich phases to reach the minimum free energy.[120-121] Reflectometry measurements show that BSA has been found to adsorb to grafted layers of PEO on planar substrates and it is further showed that BSA may penetrate the PEO layer.[122-123] Furthermore, the interactions of PEO and proteins in the bulk have been extensively studied and it is found that there are no attractive interactions between PEO and BSA in bulk solution, facilitating the use of PEG as a protein excluder. Foundational studies by Norde[124] and Halperin[125] show that protein molecules may penetrate the PEO brush to some extent. In addition, they considered partial insertion in brushes of short PEGs as illustrated by the case of bovine serum albumin (BSA).[126] However, atomic force microscopy measurements show that pH above the isoelectric point for BSA creates long range electrostatic repulsion between the negatively charged BSA and the PEO chains, whereas at lower pH, weak attractive interactions were formed.[127] Therefore, a combination of indirect and direct experimental measurement techniques and theoretical modeling show a wide array of findings for serum albumin interactions with PEO layers, showcasing the need to consolidate findings for this interesting physical problem.

Moreover, recent work has shown the prevalence of anti-PEG antibodies, demonstrating the favorable interactions of proteins with PEG.[15] Anti-PEG Immunoglobulin G antibodies binding methoxy-terminated PEG chain segments were found to adsorb onto PEG brushes grafted to lipid monolayers and adsorb at the outer edge of the brush. The results from this work reveal that IgG adopts an inverted “Y” configuration with the two characteristic FAB segments towards the brush. They suggest

that increasing the grafting density favors narrowing of the angle between the FAB segments as well as overall orientation of the bound antibodies. What is fascinating is that there is no consensus on the degree of PEG-protein interactions, what type of interactions explain their antifouling properties, and to what extent is PEG truly able to evade the immune system.

When considering the state-of-the-art methods in probing for and characterizing in-solution protein corona formation and properties, we find that there is no one method to conclusively provide evidence or a mechanism for the formation of protein corona on different material systems, and how this affects the bioavailability of drug-loaded particle systems.[128] Experimental techniques commonly applied include zeta potential to assess surface charge, dynamic light scattering (DLS) or fluorescence correlation spectroscopy to measure hydrodynamic size, absorbance spectroscopy to examine colloid morphology, fluorescence quenching and microscopy to track and confirm adsorption.[119] In fact, many seminal papers have used a combination of direct and indirect techniques to understand protein adsorption. Isothermal titration calorimetry was suitable for studying the affinity and stoichiometry of protein binding to nanoparticles, and surface plasmon resonance was also used to determine the rates of protein association and dissociation in combination with size exclusion chromatography of protein–nanoparticle mixtures.[25] Combinations of Transmission Electron Microscopy (TEM), Infrared Spectroscopy Measurements (ATR-FTIR), Dynamic Light Scattering (DLS) and Zeta-Potential Analysis, and Differential Centrifugal Sedimentation (DCS) were also used in probing for a protein corona. [129] Furthermore, laser scanning confocal microscopy, atomic force microscopy (AFM), and quartz crystal microbalance with dissipation (QCM-D) were also co-utilized to obtain an

understanding of protein-polymer surface interactions.[130] However, these techniques, while they have been pivotal in their insights into the importance of proteins in the immune system, limitations with the sensitivity and directness of these techniques have made their conclusions non representative of the real system.

In a recent review, it was suggested that protein corona is often treated as existing at thermodynamic equilibrium, despite a body of literature providing evidence otherwise.[119] Results from experimental assays used to detect protein corona and measure its size should be carefully interpreted. Large increases in hydrodynamic size, which are typically regarded as evidence of a corona, may indicate colloidal aggregation in the presence of proteins via interactions such as polymer bridging or depletion attraction due to exclusion. Techniques that assess dried-state physical properties of protein corona formation, including electron microscopy and atomic force microscopy for size and structure are invasive and require drying samples, which is not representative of the true, physiological system. Super-resolution microscopy is a powerful tool that uses a single-molecule probe with high sensitivity in probing single protein–colloid binding events, but it does this by avoiding ensemble-averaged methods of studying corona formation, which, again, is not representative of the true scenario of injecting hundreds of polymer-stabilized particles into blood. Molecular dynamics (MD) simulations, on the other hand, provide insight into interactions driving protein adsorption and their conformational changes upon adsorption shedding light on our understanding of the time-dependence or dynamics of the process. However, simulations require fine-tuning and, most importantly, comparison against experimental results to use their results, reliably, as predictive tools. The inherent complexity of being able to discern effect of adding proteins to a dispersion of polymer

coated surfaces makes this an intriguing and challenging task to find an assay that combines direct measurements and dynamics of protein-polymer interactions with minimum invasiveness.

In this paper, we establish the use of a direct, non-intrusive, and sensitive assay, Total Internal Reflection Microscopy (TIRM), to measure the interactions and layer dimensions of adsorbed PEGtb copolymers in the absence (Figure 3-1A) and presence of proteins (Figure 3-1 B-D) added to the bulk solution. TIRM is a tool that combines the best of nonintrusive, sensitive, and ensemble-averaged properties to measure colloidal interactions and layer dimensions. Three-dimensional Brownian motion tracking of an ensemble of micron-sized colloidal probes above planar surfaces via video microscopy, and evanescent wave light scattering measuring motion normal to surfaces with nanometer resolution. Additionally, equilibrium analysis provides in situ, direct evidence of how the two most abundant blood proteins, serum albumin and IgG, at blood concentrations, interact with PEGtb-coated surfaces (Figure 3-1A). Using this ultra-sensitive interaction measurement tool, we probe three possible fates of protein-PEGtb colloidal interactions: protein adsorption leading to corona formation (Figure 3-1B), negative protein adsorption leading to exclusion and depletion attraction (Figure 3-1C), and, at high protein concentrations, formation of a corona and excess nonadsorbing proteins are excluded (Figure 3-1D). Our goal is to use a combination of careful experimentation, using this assay, and theoretical modeling to discern which mechanism from Figure 3-1 do BSA and IgG, at blood concentrations, encounter when exposed to PEGtb-coated surfaces.

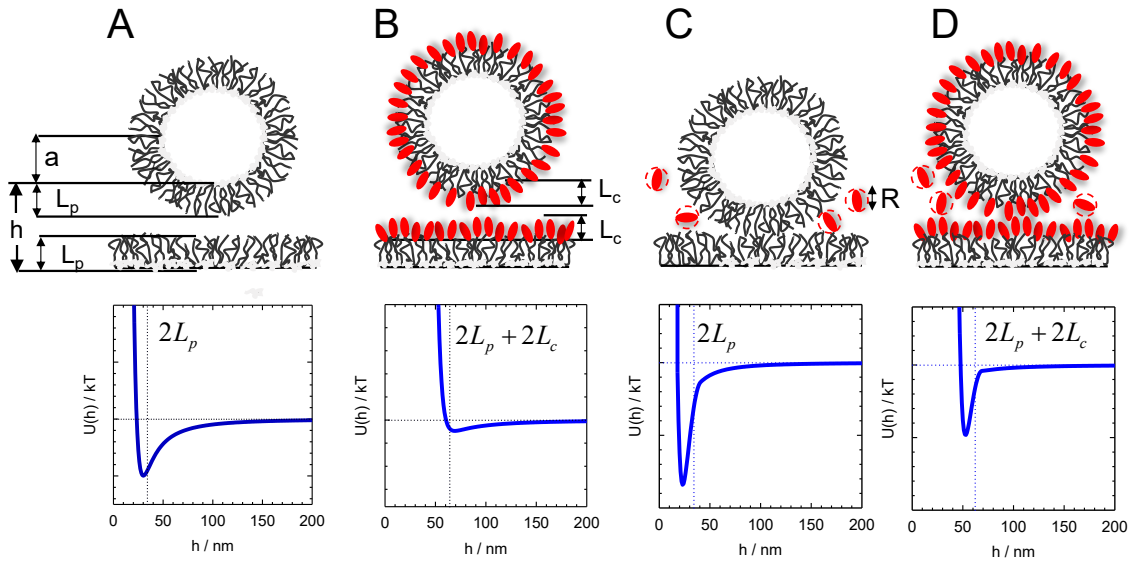

Figure 3-1 **Schematics of possible fates of adsorbed PEGtb layers in the absence and presence of blood proteins and predicted kT-scale interaction potentials.** (A) Top: Variables define colloid and PEGtb dimensions. Bottom: theoretical superposition of steric repulsion between PEGtb layers and vdW attraction between the particle and wall (vertical dashed lines refer to the thickness of the layers at contact, and horizontal dashed lines refer to 0 *kT*). (B) Top: Protein adsorption/corona on the surface of PEGtb of thickness L_p+L_c. Bottom: theoretical interaction potential showing the effect of adsorbed protein. (C) Schematic for the case of nonadsorbing proteins, with a dimension of R nm, that are excluded. Bottom: theoretical interaction potentials illustrate the effect of proteins exclusion without change in the steric thickness. (D) Top: Schematic describing proteins that fully coating the PEGtb brush, and excess nonadsorbing proteins excluded from the gap. Bottom: theoretical interaction potentials illustrating the effect of a protein corona in addition to exclusion of nonadsorbing proteins creating depletion attraction.

3.3 Results

3.3.1 Symmetric PEGtb interactions in physiological ionic strength in absence of proteins

Figure 3-2 illustrates, sequentially, how three-dimensional trajectories, local binding events, and interaction potentials provide a clear story on how to understand thew interaction of polymer-coated surfaces in absence of proteins as a control case, before blood proteins are introduced. While we can employ lateral diffusion analysis to understand colloidal interactions at a high level much comparable to other techniques, our analysis is unique in that it employs the scattering intensity of each diffusing colloid in the evanescent

wave and converts the intensity at each timepoint to normal height excursions as a function of time using. Figure 3-2A shows three representative colloids with adsorbed PEGtb diffusing freely above a PEGtb coated wall in the x- and y-direction, and the scale bar shows that in 150 mM NaCl, PEGtb-coated microparticles diffuse freely in the x- and y-directions with ~1s binding events. Figure 2B shows the height excursions over time for each of the representative particles and shows that not only are particles freely diffusing in the x- and y-directions, but they are freely diffusing in the normal, z-direction where each particle moves within 500 nm above the PEGtb-coated surface and exhibits binding events no longer than 1 second. Analyzing the equilibrium histogram of heights sampled by each of the particles above surfaces allows us to obtain particle–wall interaction potentials (Figure 3-2C).

The ensemble averaged net interaction potential is then fit with a superposition of short-range attractive interactions and longer-range steric repulsion between the adsorbed layers of PEGtb. The inset shows the net potential profiles for individual particles and the ensemble average without subtracting the contribution from gravity to show the consistency of behavior among the ensemble of 10 particles in the sample and narrow polydispersity in particle size. Our theoretical fits show that PEGtb in 150 mM NaCl forms 17 nm thick layers with ~0.5 kT surface vdW attraction. For clarity, in the remainder of the paper, we will present interaction potentials without gravity to illustrate concisely the balance of repulsive interactions and attractive interactions, and how this balance changes upon introduction of blood proteins (BSA and IgG).

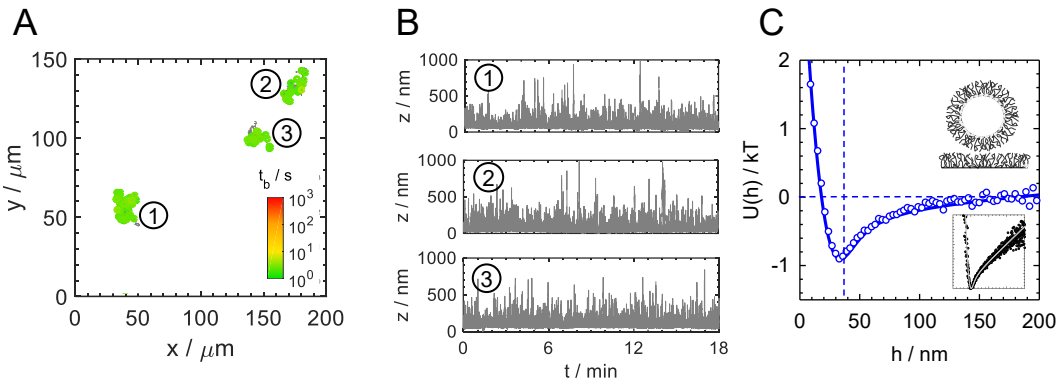

Figure 3-2 **A comprehensive, quantitative description of interactions between adsorbed PEGtb layers using 3D Brownian trajectories with nm-resolution and kT-scale interaction potentials.** (A) x- and y- trajectories of three representative diffusing particles with adsorbed PEGtb diffusing over an adsorbed layer of PEGtb on a wall in 150 mM NaCl. The scale bar illustrates the binding lifetime of each colloid in normal to the surface, where green indicates ~1s binding events, indicating stable levitating particles, and red indicates 1000s binding lifetimes, indicating increased attraction between the colloid and wall. (B) z-trajectories, or normal height excursions above the wall over 20 minutes for each particle. (C) *kT*-scale interaction potential profiles averaged over an ensemble of individual colloids (shown in inset), with gravity subtracted to illustrate the sum of attractive van der Waals attraction between the colloid and wall, and steric repulsion between the adsorbed PEGtb layers. In 150 mM NaCl, PEGtb forms 17 nm thick layers on the particle and wall ($2L_0$ = 34 nm as shown by the dashed line where two PEGtb layers first come into contact at 0.1 *kT*).

3.3.2 BSA and IgG Exclusion from Adsorbed PEG copolymer layers

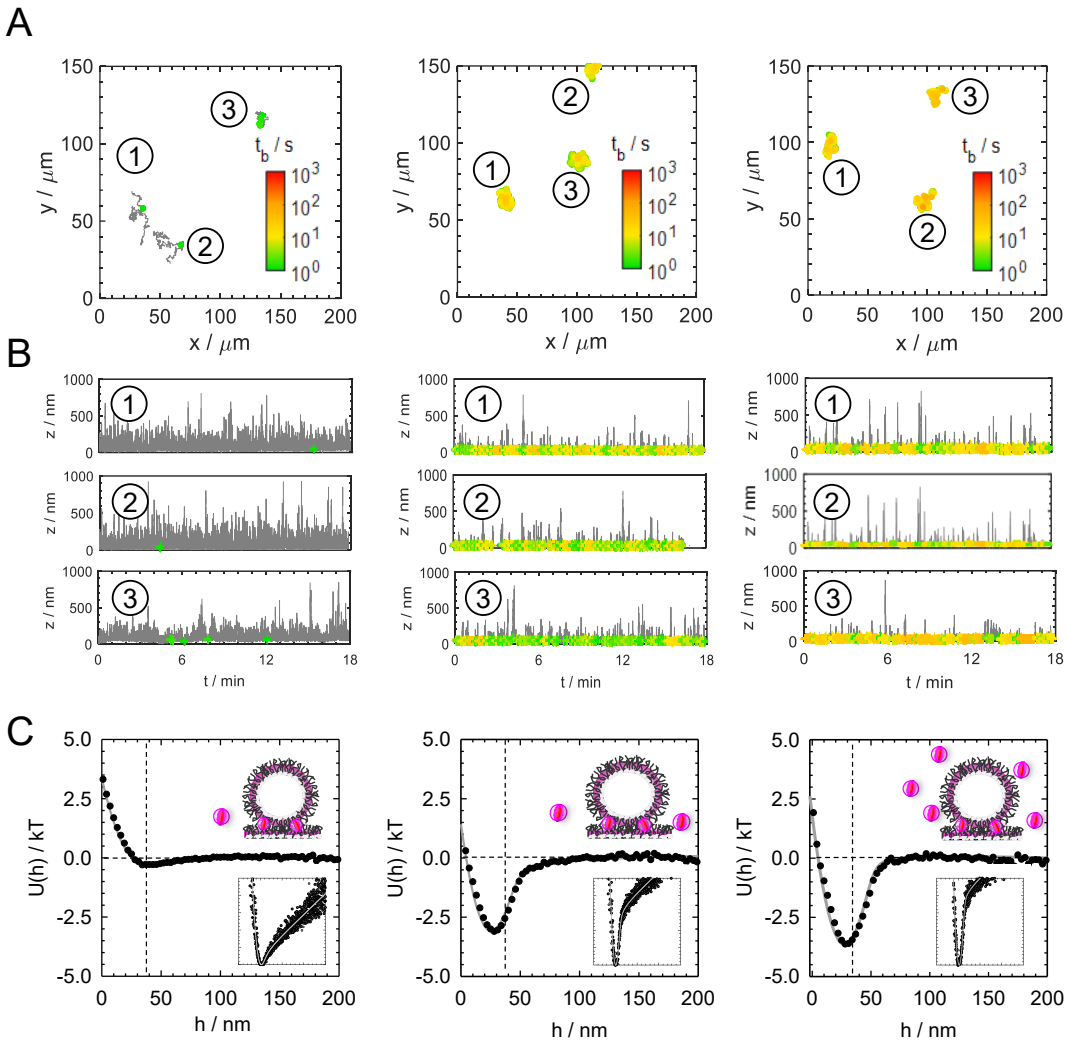

Figure 3-3 **3D trajectories and kT-interaction potentials show that BSA is excluded and does not form a corona on PEG.** (A) From left to right: x,y trajectories of three representative particles with adsorbed PEGtb diffusing over PEGtb adsorbed to a wall with 20, 30, and 40 g/L BSA added to the bulk. Scale bar in the inset illustrates the length of time a particle is bound to the surface as it diffuses laterally on the surface. (B) From left to right: z-trajectories illustrate particle diffusion normal to the surface that correlate to binding lifetimes. Short binding lifetimes correspond to a particle diffusing freely in the z-direction, such as in the case for 20 g/L BSA, whereas longer binding lifetimes correlate to particles diffusing closer to the surface, such as with 30-40 g/L BSA. (C) Ensemble averaged interaction potentials from the probability distribution of height excursions from B show a progressive deepening of the attraction well depths (from -0.5 kT to -3 kT from 20 g/L to 40 g/L BSA, respectively) and a constant polymer layer thickness at contact ($2L_0$ = 34 nm) for all cases.

For three representative particles in the ensemble, in Figure 3-3, we illustrate direct, sensitive measurements of colloidal interactions in the case of PEGtb-coated surfaces with BSA added to the bulk solution. Figure 3-3A shows that when the concentration of BSA in the bulk solution increases from 20−40 g/L, the normal binding lifetime, illustrated visually by the color scheme shown in the legend, progressively increases from 1 second at 20 g/L BSA to ~1000 seconds at 40 g/L. Additionally, we note that particles are freely diffusing in the x- and y-direction, demonstrating that addition of BSA into the bulk solution impacts normal binding of particles to the surface. In Figure 3-3B, we obtain the normal diffusion trajectories, z-trajectories, of each particle in Figure 3A by converting scattering intensity to height, which we explain in detail in previous publications, with nanometer resolution. These z-trajectories illustrate clearly how each of the representative particles diffuse progressively closer to the surface when the concentration of BSA increases, shown by how each particle diffuses at an increasing length of time a few nanometers above the surface at 40 g/L BSA, compared to the normal diffusion within a larger range of heights at 20 g/L, with 30 g/L exhibiting intermediate normal diffusion profiles.

Figure 3-3C shows how we integrate total internal reflection and three-dimensional particle trajectories by measuring single and ensemble-averaged particle-surface interactions. By fitting the ensemble averaged particle-surface interactions to a theoretical net interaction potential, we note two important findings: Firstly, the net attraction energy well depth increases from −0.5 kT to −3 kT from 20 g/L BSA to 40 g/L, respectively, where the origin of increase of attraction between the adsorbed polymer layers is due to BSA being depleted from PEGtb. Secondly, the thickness of the steric layer remains constant at

17 nm, which is the measured thickness of PEGtb layers in 150 mM NaCl shown in Figure 3-2C. These results unmistakably demonstrate that BSA, at physiological concentrations, does not adsorb to the outer layer of adsorbed PEGtb in good solvent conditions, rather this protein is excluded.

Although our measurement itself cannot distinguish where BSA is, we use three self-consistent approaches to the depletion interaction potential in Eq 2−3 by adjusting the degree of partitioning of BSA between PEGtb layers and the bulk solution, $\Delta\Pi$, the degree of penetration of the BSA into the PEGtb layer which affects the excluded volume for these soft surfaces, *f,* or an intermediate solution between these two cases, in order to estimate a self-consistent mechanism behind BSA exclusion from PEGtb affecting both the osmotic pressure and total excluded volume. If we use partitioning, $\Delta\Pi$, as the mechanism behind exclusion, we find that, for all cases for BSA, i.e., 20−40 g/L, ~99% of the total number of BSA molecules are excluded into the bulk. On the other hand, we achieve the exact same theoretical fits shown in Figure 3-3C if BSA is allowed to penetrate the PEGtb layer. In this case, we find that BSA at 20 g/L penetrates 10 nm, 30 g/L penetrates 7 nm, and 40 g/L BSA penetrates 5 nm into PEGtb. The approximation method we use to explore possible mechanisms between the two limits above considers the possibility of both penetration and partitioning shows us that BSA exclusion can be explained by our theoretical fits that provide a self-consistent approach to show that BSA can be depleted from PEGtb layers via partitioning and penetration into the PEGtb layer. It is important to note here that the parameter describing penetration into the polymer layer does not mean that proteins adsorb to the PEG layer, rather this describes a dynamic effect.

What is noteworthy in these experiments is that the order of physisorption and protein addition had a significant effect on the outcomes of potential energy profiles. In this paper, we present results when we employed a careful protocol simulating drug delivery conditions. In short, we added proteins after PEGtb has reached equilibrium following standard PEG's Langmuir adsorption isotherms. In previous setups where proteins were mixed earlier, we found that BSA had no effect on both the steric thickness and the net attraction, and IgG had heterogenous binding to different sites on the wall. However, with long equilibration times and careful protein addition after formation of the intact PEGtb layer, we eliminated any nonequilibrium structures, and found that with this method, BSA and IgG exclusion is significant from PEGtb and both proteins may partition and penetrate the layers. This is a crucial observation because it speaks to how other experimental techniques may lack the sensitivity to discern nonequilibrium structures due to heterogeneity and this highlights the need to develop an assay that carefully simulates drug delivery applications when studying sensitive interactions between proteins and polymer-coated surfaces to ensure that measurements of protein adsorption are not due to surface heterogeneities or defects.

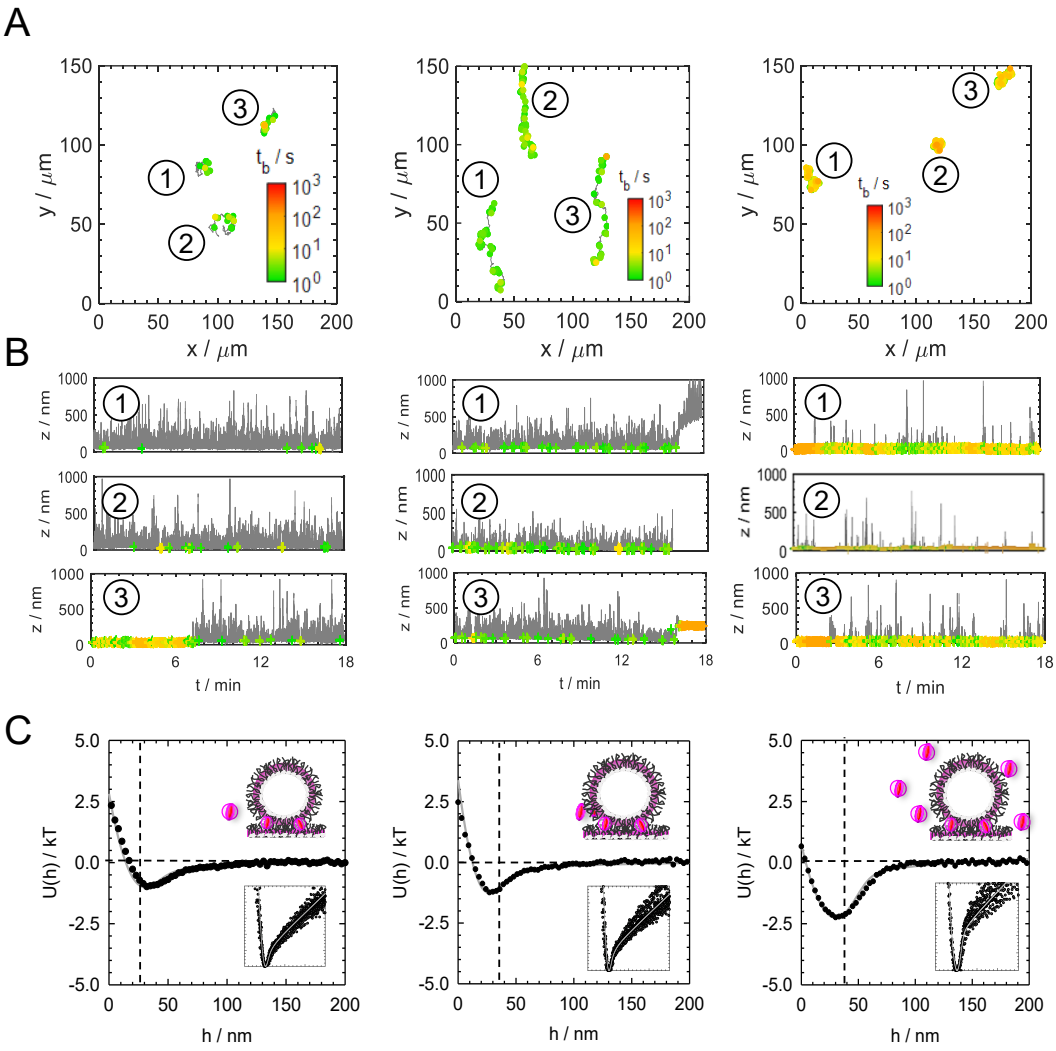

Figure 3-4 **3D trajectories and kT-interaction potentials show that IgG is excluded and does not form a corona on PEG.** (A) From left to right: x,y trajectories of three representative particles with adsorbed PEGtb diffusing over PEGtb adsorbed to a wall with 2.5, 5, and 10 g/L IgG added to the bulk. Scale bar in the inset illustrates the length of time a particle is bound to the surface as it diffuses laterally on the surface. (B) From left to right: z-trajectories illustrate particle diffusion normal to the surface that correlate to binding lifetimes. Short binding lifetimes correspond to a particle diffusing freely in the z-direction, such as in the case for 2.5 g/L IgG, whereas longer binding lifetimes correlate to particles diffusing closer to the surface, such as with 5-10 g/L IgG. (C) Ensemble averaged interaction potentials from the probability distribution of height excursions from B show a progressive deepening of the attraction well depths (from -0.5 kT to -3 kT from 2.5 g/L to 10 g/L IgG, respectively) and a constant polymer layer thickness at contact ($2L_0$ = 34 nm) for all cases.

We observed remarkably similar macroscopic behavior of IgG, a protein twice the molecular weight as BSA with a significantly different shape. In these experiments, we probe IgG-PEGtb interactions below and at blood concentrations, from 2.5 mg/mL to 10

g/L. Using the same approach in Figure 3-3, Figure 3-4A illustrates how addition of IgG into the bulk solution results in a progressive increase in normal binding lifetimes like BSA. However, we note that normal binding events >10s long occur at the lowest concentration of IgG, 2.5 mg/mL, which corresponds to 0.006 v/v whereas the onset of >10s binding lifetimes occur with BSA at 30 mg/mL, which corresponds to 0.042 v/v, an order of magnitude above the volume fraction of IgG, illustrating that a smaller amount of IgG is needed to cause attractive interactions with PEGtb layers. Figure 3-4B shows a similar progression in the increase in length of time a particle levitates within a few nanometers above the wall, where particles experience free normal diffusion at 2.5 mg/mL IgG, become more attracted to the surface shown by shorter normal excursions at 5 mg/mL, and spend minutes levitating within a few nanometers above the wall at 10 mg/mL IgG. Figure 3-4C complements the three-dimensional dynamics of these particles with ensemble-averaged kT-scale potential energy profiles. Again, we observe two important behaviors of adsorbed PEGtb copolymer layers in the presence of IgG: Firstly, the net attraction well depth progressively increases from −1.5 kT at 2.5 mg/mL to −2.5 kT at 10 mg/mL. Secondly, the steric layer thickness inferred from theoretical fits to the net potential remained constant at 17 nm, i.e., the same measured thickness as the native PEGtb layer in Figure 3-2C.

Like BSA, we find that theoretical fits to the average potential profiles indicate that IgG is also excluded from PEGtb layers. Using the same approach for theoretical fits to explain the mechanism of exclusion we find that if we use partitioning, $\Delta\Pi$, as the sole adjustable parameter, we find that ~87% of the total number of IgG molecules are partitioned into the bulk at 2.5 mg/mL IgG, whereas ~92% of IgG molecules are partitioned

into the bulk at 5−10 mg/mL. Moreover, we achieve the same theoretical fits in Figure 3-4C if IgG is allowed to penetrate the PEGtb layer, i.e, the penetration depth is the only adjustable parameter. In this case, we find that IgG at 2.5 mg/mL penetrates 5 nm, and IgG penetrates ~7 nm at 5−10 mg/mL. The approximation method we use to explore possible mechanisms between the two limits above shows us that IgG at 2.5−10 mg/mL may both penetrate, on average, 6 nm into the PEGtb layer while also having, on average, 78% of the added IgG partition into the bulk.

In summary, we use careful equilibrium analysis to non-intrusively and sensitively probe how blood concentrations of BSA and IgG interact with PEGtb coated surfaces and determined that neither blood protein forms a steric coating around PEG. Rather, BSA and IgG are excluded/depleted from the adsorbed PEGtb layer. Our theoretical models using modified AO depletion potentials for soft surfaces can be modified systematically to show the effect of the osmotic pressure difference and change in excluded volume, and we showed that both BSA and IgG can penetrate into PEGtb layers and be excluded into the bulk solution, which explains the origin of the increasing attraction when both proteins are added to a dispersion of PEGtb-coated surfaces.

3.3.3 Discussion

It is important to consider the phase behavior of adsorbed PEGtb in absence of proteins, because understanding polymeric stabilization in good solvent conditions, such as the condition shown in Figure 3-2, will help towards understanding the phase behavior of PEGtb-coated surfaces when proteins are introduced into the system. Solvent quality is a term that refers to how favorable interactions are between polymer segments and solvent molecules, ranging from “good” to “poor” at a polymer solution’s θ, theta, condition where

the polymer chain segments adopt a random walk, i.e., when polymer chains behave like ideal chains.[131] The scaling of polymer chain dimensions and length is determined by solvent quality behavior, which affects the range of repulsive or attractive interactions. In good solvent conditions, symmetric layers of adsorbed PEG copolymers are stabilized via a balance between osmotic interactions, resisting compression, and elasticity, resisting stretching, to maximize interactions with surrounding solvent molecules. However, in poor solvents, symmetric layers of adsorbed PEG copolymers interpenetrate to minimize interactions with the solvent.[132-133]

Addition of NaCl as a cosolute does not change water structure, and thus does not affect PEG solubility or interactions in water, therefore at 150 mM NaCl, adsorbed layers of PEG copolymers are in good solvent conditions, thus we expect PEG to form thick extended brushes in 150 mM NaCl, anchored by the hydrophobic PPO midblock on hydrophobically modified surfaces. The collapsed configuration of proteins, on the other hand, has been equated to water being a "poor" solvent, despite growing evidence which shows that favorable chain-solvent interactions reduce misfolded or aggregated-prone states,[134] so the solvent quality of blood is not necessarily poor for proteins. Compared to symmetric interactions in the PEG-PEG case (Figure 3-2A) where interpenetration is not likely to occur in good solvent conditions, asymmetric interactions due to the introduction of proteins may give rise to more interpenetration or structural rearrangement of the protein-polymer complexes, lowering the total energy of both layers on contact. [135]

Destabilization due to immiscibility of different components in a biphasic system, such as proteins and polymers in aqueous solutions, relates to the expulsion of polymer from the spaces between particles, and can be explained by excluded volume and osmotic

constraints as well as conformational entropy loss. The attractive depletion interaction was first analytically described by a theoretical model by Asakura and Oosawa (AO)[136] and later by Vrij.[137] In the AO model, the depletant being excluded from two large plates is assumed to be a hard sphere, and in Vrij's model, polymer coils are regarded as soft spheres that can overlap but exhibit hard interactions with surrounding colloidal particles. Later treatments examine depletion of a soft polymer solution near a hard wall followed by work examining the exclusion of soft polymers between two hard plates. [138-139] Subsequent work systematically describe various approaches to theoretically modelling exclusion and consider ideal polymer chains, hard spheres, hard walls, and colloidal disks.[140] However, the system described in this paper involves 'soft' protein macromolecules interacting with 'soft' polymer brushes on two symmetric surfaces. Therefore, traditional treatments of exclusion using AO potentials, De Gennes, and Lekkerkerker may not apply to our system of soft surfaces in contact making this system even more interesting, given its relevance to antifouling biomaterial design.

Although this is beyond the scope of this work, we also cannot neglect the importance of contributions to the net interaction from multi-body effects. This is particularly true in case of polymer chains with high molecular weight proteins where multibody contributions non-negligible since a single chain can interact more favorably with more than two colloids. In summary, depletion effects in solutions of macromolecular mixtures cannot be ignored, especially in drug delivery applications where polymer-coated colloids encounter concentrated protein solutions and have been known to interact with

plasma proteins; however, traditional treatments of depletion attraction reveal the need for adapting theory to model 'soft' interactions between polymer brushes and proteins.

Measured interactions revealing depletion of both proteins from PEG may be closely related to previous observations of PEG-induced phase separation of protein solutions and with other direct measurements of these protein's interactions with immobilized PEG monolayers. BSA, a protein with an effective hard sphere radius of 3.3 nm,[141] and IgG, with an effective hard sphere radius of 3.5 nm,[142] are both known to have positive second virial coefficients in physiological conditions. We achieve these values for protein size by fitting Carnahan-Starling equation of state to measurements osmotic pressure for both proteins and obtain values within expected dimensions from globular protein scaling theory.[143] There is a body of work that has shown how to induce phase separation in protein solutions by introducing an additional attractive interaction via adding polymers into solution.[144-147] PEG has been shown to induce phase separation of BSA and IgG through generating depletion attraction between protein molecules that is not well described by the standard depletion models, and the degree of depletion and decrease of the second virial coefficient, B_2, were found to depend on temperature, polymer concentration, and molecular weight.[147] Given the growing evidence that proteins in their folded states are in "good" solvent conditions, addition of PEG in the mixture may affect protein's solvent quality, impacting the range of repulsive and attractive interactions of proteins with each other, surrounding solvent molecules, and PEG. This is interesting given our sensitive nanometer resolution of layer thickness which indicates that PEG copolymers maintain their solvated dimensions even in the presence of protein solutions at blood

concentrations (between 1−6% v/v), which may indicate that concentrated blood protein solutions may still be good solvents for anchored PEG copolymers.

Furthermore, neutron reflectometry and surface plasmon resonance were utilized in several publications to investigate phase behavior of protein-polymer mixtures when the polymer is adsorbed or anchored to a planar substrate. [15, 125-126, 132, 148] Both proteins in this work were found to penetrate PEG layers to varying degrees; BSA binding and insertion into PEO layers depended on the grafting density, and in all cases, below and at the brush regime, BSA penetration still occurred. IgG was also found to have varying degrees of penetration into grafted PEO monolayers, where neutron reflectometry showed partial insertion of IgG ~2 nm into a PEO brush layer, and some adsorption on the periphery of the PEO monolayer. This is intriguing because it is consistent with our adaptation of the classical AO depletion potential to fit our experimental results, where tuning the excluded volume term using a parameter to account for penetration shows that both BSA and IgG partially penetrate the PEG brush layer, perhaps suggesting weak attractive interactions between these proteins and PEG molecules in addition to excluded volume and osmotic pressure effects giving rise to a self-consistent picture of the complexity of protein exclusion from PEG.

Several papers additionally deduce different mechanisms of these weak attractive interactions: insertion and compression. In the case of serum albumin, evidence suggest different adsorption scenarios: one due to weak, nonspecific monomer−protein attraction,[123] and secondly partial insertion of BSA into PEG layers due to attractive van

der Waals interactions with the underlying surface, which highlights the importance of the polymer layer density, among other design parameters highlighted in their work. In the case of antibodies, such as IgG, some evidence of polymer binding at specific protein sites for example, by PEG antibodies, has been shown involving terminal binding on the free ends of a polymer anchored to a surface, or backbone binding to internal chain segments. It is important to highlight the distinction between BSA and IgG in terms of their shape, for IgG is Y-shaped, whereas BSA is often assumed to have an ellipsoidal structure, since the shape of a protein, if assumed to maintain its native folded structure, may affect the degree to which insertion and compression into PEG layers takes place. This may be true in context of our results in Figure 3-3 and Figure 3-4, where the degree of penetration and partitioning for BSA was higher than that of IgG, perhaps indicative of the effect of shape of the protein and its osmotic pressure on its ability to insert into polymer layers of a constant density and preferentially partition into the bulk solution. Regardless of the effects of protein dimensions, our results clearly demonstrate that tuning partitioning and exclusion to account for both proteins and polymer softness, we achieve agreement between theory and experimental data supporting the fact that BSA and IgG are excluded from PEG.

3.4 Conclusions and Outlook

Using the two most abundant blood proteins, serum albumin and IgG, we found that neither protein forms what is known as a ‘protein corona’ around adsorbed layers of PEG. Our careful experimental assay and equilibrium analysis reveal quantitatively and qualitatively interesting behavior for both proteins, even though they differ in shape, function, and biophysical properties. As a benchmark, we characterized solution behavior

of PEG brushes in good solvent and established the thickness of the polymer layer as 17 nm. Our direct and sensitive measurement of layer thickness and colloidal interactions revealed that even at blood levels of both proteins, the PEG layer remarkably remained constant, and the origin of increased attraction is from progressively increasing depletion of the protein from the polymer layer. Careful theoretical modeling reveals that depletion attraction can be modeled using modified AO theory and systematic adjustments of the osmotic pressure difference and excluded volume effects, reflecting the need to adapt traditional models to describe soft interactions between the proteins and polymers.

Regardless of what adjustable parameter or approximation we used, the model accurately described our experimental results, and, thus, can be used to give a reasonable description without developing rigorous models. Our theoretical models also show that both proteins can penetrate the PEG layer to some degree and may partition between the polymer gap and the bulk solution. While the degree of penetration had no strong correlation with blood protein concentration, partitioning increased when the concentration of proteins in the bulk increased, which is consistent with increased protein exclusion and colloidal attraction at higher concentrations. Moreover, our assay is free from surface heterogeneities, and we believe that this could be a useful tool for probing polymer interactions with numerous biomacromolecules.

Ultimately, these results provide a strong foundation to study protein interactions with polymer coated surfaces for drug delivery applications with minimal invasiveness and maximum sensitivity, and statistical significance. Our findings entail the need for developing an accurate theoretical model to describe the balance of globular protein exclusion and penetration between two soft polymer layers. Additionally, we recognize the

importance of including a study on the synergistic effects of these proteins, and the effect of grafting the polymer layers. We hope to use our assay to shed light on the immune system response to protein depletion and penetration into polymer layers.

3.5 Methods

Surfaces. The commercial PEO_{141}-PPO_{51}-PEO_{141} (F108) copolymer (M_w/M_n=1.2) was donated by BASF. The adsorbed triblock copolymer is abbreviated by its end blocks with the suffix "tb" to indicate 'triblock'. 66 kDa lyophilized bovine serum albumin (>99% purity, essentially gamma-globulin free) and 150 kDa γ-Globulin from bovine blood (≥99% purity, mixture of IgG (80%), IgM (10%), and IgA (<10%)) were obtained from Sigma Aldrich and used without further purification or modification. For brevity, bovine serum albumin will be referred to as BSA, and γ-Globulin will be referred to as IgG, since most of the bovine γ-Globulin sample is composed of IgG, in the manuscript. Both protein stock solutions were prepared in 150 mM NaCl and sonicated for 30 minutes. Glass microscope slides (Fisher) were cleaned and rendered hydrophobic according to protocols in previous publications from this group. Briefly, glass slides were cleaned in acetone, 100 mM KOH, and DI water, and rendered hydrophobic by spin coating polystyrene. Silica colloids of nominal 2.2 μm diameter (Bangs Laboratories) were rendered hydrophobic by coating with 1-octadecanol (Sigma-Aldrich). Despite different chemical functionalities on hydrophobic particle sand slide surfaces, prior studies have shown the same triblock copolymers in this study yield the same solvent quality dependent thickness even with two different coatings.[149]

Polymer Adsorption. 1000 ppm PEOtb was dissolved in 150 mM NaCl and added to vacuum grease-sealed O-rings on a hydrophobically modified glass slide and left to

equilibrate overnight, and 1000 ppm PEOtb dissolved in DI water was added to 2 uL of hydrophobically modified 2μm glass particles. The PEOtb-silica dispersion was exchanged into 150 mM NaCl after 3 hours of adsorption, via centrifugation, and was left to equilibrate on an inverted overnight. 1 μL of the PEOtb-silica dispersion was then added to the PEOtb on the slide and left to equilibrate in 150 mM NaCl for two hours. An equal volume of 2x the final desired concentration of the protein solution was added to the particle-wall system and left to equilibrate for two hours prior to measurements.

Microscopy. Ensemble TIRM was used to measure interactions between polymer coated colloids and slide as described in previous work. In summary, an evanescent wave is generated via reflection of a 633 nm HeNe laser (Melles Griot) onto a prism at 68 degrees. Images are captured using a 40× objective (LD Plan-NEOFLUAR), using a 12−bit CCD Camera (Hamamatsu Orca-ER) at 4 binning, 4 ms exposure, and a frame rate of 28 frames per second. In the TIRM experiment, scattering intensity, I, of a spherical colloidal particle in an evanescent wave is used to determine relative particle-wall separation, h. Measurements of single particle potentials are averaged to obtain ensemble average potentials.

3.6 Analysis

The net potential energy for PEG-stabilized colloids and substrates, u_N, in the presence of proteins added to the bulk solution may be given by a superposition of potentials due to van der Waals attraction, u_V, steric repulsion, u_S, and gravity, u_G, and depletion attraction, u_D, as,

$$u_{\text{net}}(h) = u_G(h) + u_{\text{V}}(h) + u_{\text{S}}(h,L) + u_{\text{D}}(h,L)$$

$$u_{\text{net}}(h) = (4/3)\pi a^3 \left(\rho_p - \rho_f\right) gh - \frac{a}{6}\int_h^\infty -\frac{A(h)}{h^2} dh + \Gamma \exp\left[-\delta\left(h - 2L\right)\right] - \Delta\Pi V_{\text{EX}}\left(h,L\right) \quad (4.1)$$

where h is particle-wall separation. Subscripts refer to interactions as: (V) van der Waals, (G) gravitational, (D) depletion, and (S) steric. The gravitational potential energy of each particle depends on its elevation above the underlying surface multiplied by its buoyant weight, where ρ_p and ρ_f are the particle and fluid densities. van der Waals attraction for sphere-plate are predicted from the rigorous Lifschitz theory where $A(l)$ includes retardation and screening for the silica colloids and glass substrates used in this work, explained in detail in previous publications.[65, 81] Steric repulsion due to compression of excluded volume macromolecular brushes are modeled using a soft exponential decay that fits the Milner brush theory until 50% compression of the brush. In our model, the pre-factor, Γ, is 0.1 kT and reflects the polymer layer repulsion upon contact at $2L_0$ as well as the limit to the sensitivity of our measurement technique. δ is the decay length of the exponential, which is defined as 0.281 nm $^{-1}$, and L is the thickness of a PEG layer here defined as $L = L_p$. If a protein fully coats the adsorbed PEG layers on both the particle and wall, a bilayer or protein corona is formed. From Eq. 1, we see that the adsorbing of proteins on the PEGtb coatings will impact the range of steric repulsion. In this case, L is the total measured layer thickness, which will be composed of the polymer thickness, L_p, and the measured protein corona thickness, L_c, that becomes $L = L_p + L_c$.

According to several models for depletion or exclusion, namely the AO depletion model, nonadsorbing proteins may be partially or totally excluded from the gap between the PEG-coated colloid and the PEG-coated substrate and result in depletion attraction

reflected in Eq 1 as u_D (h, L). In short, ΔΠ, defined in Eq 2 below, is the protein's osmotic pressure difference given as the ideal contribution modified by compressibility factors inside and outside the excluded volume region, Z_i and Z_o respectively as shown in Eq 2, below. Z_i and Z_o are modeled by the Carnahan-Starling equation of state as a function of bulk and gap number densities of the protein, and has been shown to sufficiently describe nonideal behavior of globular proteins in physiological ionic strength.[142]

$$\begin{aligned} \Delta\Pi &= \Pi_o - \Pi_i = \rho_o kT\left(Z_o\left(\rho_o\right) - Z_{in}\left(\rho_i\right)\cdot\left\langle K\right\rangle\right) \\ \left\langle K\right\rangle &= \left(2R\right)^{-1}\int_0^{2R\rho_o} h^{-1}dh\int_0^{h} K\left(h,x\right)dx \;,\; K\left(h,x\right) \equiv \frac{\rho_i\left(\rho_o,h,x\right)}{\rho_o} \end{aligned} \tag{4.2}$$

Here, ρ_o is the depletant number density outside the excluded volume region, and $\left\langle K\right\rangle$ is the partition coefficient defined as $\langle\rho_i\rangle/\rho_o$ (where $\langle\rho_i\rangle$ is an average number density of the depletants inside the excluded volume region) modeled in Edwards et al.[150]

The expression to model the excluded volume region between a hard depletant and hard sphere, V_{EX}, is typically given as,

$$\begin{aligned} V_{ex}\left(h_S,R\right) &= \pi\left(\frac{4}{3}R^3 + \frac{4}{3}aR^2 - 4aRh_S + ah_S{}^2 - Rh_S{}^2 + \frac{h_S{}^3}{3}\right) \\ h_S &= h - 2Lf \end{aligned} \tag{4.3}$$

where R is the depletant's effective hard-sphere radius, fixed from fitting literature values of osmotic pressure of BSA and IgG to the Carnahan-Starling EOS with the Donnan contribution at 150 mM NaCl. [141-142] To account for the softness of the brush and proteins and potential attractive asymmetric interactions, we include a factor to allow for proteins

to penetrate the PEG brush layer. In Eq 3, we represent this with *f* which is the percent brush thickness that is inaccessible to the depletant or protein (impenetrable thickness).

To our knowledge, there is no theoretical model of the average partition coefficient, $\langle K \rangle$, of soft globular proteins between soft polymer layers. Therefore, in this work, we rely on the closest approximation for the density profiles using expressions for PEO random coils excluded between two hard plates where PEO density profiles are determined from superposition[140] of the single wall density profile [138, 151] using a correlation length from RG theory as detailed in previous work. In brief, we compute the equivalent size and volume fraction for PEO for each condition used for BSA and IgG in this work to estimate the appropriate $\langle K \rangle$ and use an iterative method to find the value of *f* that satisfies the partition coefficient expression and fits to the measured interaction potentials in Figure 3 and 4. This allows us to survey an appropriate intermediate solution between the hard surface limits either imposed by setting $\langle K \rangle = 0$ or setting $f = 1$. This results in a self-consistent explanation on the mechanism of BSA and IgG being excluded from PEG. Results from this method are summarized in Table 2.

In limit of high-volume fractions of protein, if there are sufficient attractive interactions between PEG and the added protein, the protein forms a full corona around PEGtb on the colloid and wall, any excess protein that does not adsorb may be depleted from the gap between the particle and wall. This case will affect both the steric and depletion contributions in Eq. 1 shown above. To summarize, we can use our ultra-sensitive technique and analysis to probe and model the net interactions between PEGtb coated

particles and wall with and without proteins in the bulk solution. Our non-intrusive, highly sensitive measurement technique and analysis method will provide us unambiguous understanding of how proteins modulate the thickness of the steric layer and/or the amount of depletion attraction due to protein exclusion from the gap, with nanometer- and kT-resolution.

Table 1. Fixed Parameters Used for Theoretical Fits (Eq 1-3) to Generate Results in Figures 3 and 4. [a]

Parameter	Value
2a (μm)	2.14
Γ (kT)	0.1
L (nm)	17
δ (nm^{-1})	0.281
Mw_{BSA} (kDa)	69
Mw_{IgG} (kDa)	150
R_{BSA} (nm)	3.3
R_{IgG} (nm)	3.5

Table 2. Adjustable Parameters Used for Theoretical Fits (Eq 1-3) to Generate Results in Figures 3 and 4.

Parameter	[BSA] gL^{-1}			[IgG] gL^{-1}		
	20	30	40	2.5	5	10
f [b]	0.48	0.68	0.75	0.94	0.842	0.806
$\langle K \rangle$ [c]	0.74	0.79	0.8	0.81	0.8	0.797
L (nm) [d]	17	17	17	17	17	17

[a] The colloid radius fit to the gravitational potential is shown in the first row, Γ was set to 0.1 kT to calculate the thickness of the layers at contact, and the decay length was fixed to 0.281 nm^{-1} for a 17 nm thick PEG brush as measured in Figure 2. All the potential fits reveal that $L_c = 0$ nm; therefore, L is equal to the polymer brush length, L_p. The effective hard sphere radius, R, for each protein is fixed from fitting the Carnahan-Starling equation of state to experimental osmotic pressure data. Other independent parameters include van der Waals power, p=2.195, and size dependent contact value, $A = (2140/a)kT$ nm^{1+p}. [149]

[b] We show the results from using the available theory for partitioning of PEO, as explained in the text, to find an intermediate solution for f and $\langle K \rangle$.

4 BLOOD PROTEINS DISPLACE PHYSISORBED ZWITTERIONIC COPOLYMERS

4.1 Abstract

We report direct and sensitive measurements of the interactions of zwitterionic copolymer-coated colloids with two major blood proteins, BSA and IgG. Previous work shows that BSA and IgG are excluded from and do not adsorb to PEG copolymer brushes; however, a similar comparison using direct, *in situ* interaction measurements on polyzwitterions has not been made. We employ three-dimensional multiple particle trajectories and kT-scale potential energy profiles from Total Internal Reflection Microscopy (TIRM) to evaluate the hypothesis that zwitterionic polymers have an increased resistance to blood protein adsorption. We find that BSA adsorbed to the surface of high molecular weight PMAPS brushes but is weakly excluded from high molecular weight PMPC brushes. Secondly, we find that both high molecular weight PMPC and PMAPS competitively adsorb with IgG, forming defective layers at higher IgG concentrations. To examine the well-documented molecular weight-driven competitive adsorption, we use low molecular weight PMPC and PMPAS copolymer brushes adsorbed to both the colloid and wall and find that both copolymers competitively adsorb with both BSA and IgG. Our results unambiguously show that adsorbed zwitterionic copolymer coatings are not completely inert to high molecular weight blood proteins, in stark contrast to adsorbed PEG copolymers. Using direct, kT-scale, time-averaged measurements of multiple particle-wall interactions using super-resolution microscopy, our results suggest that the interaction of adsorbed zwitterionic copolymers with high molecular weight, abundant blood proteins arise from a balance of both symmetric and asymmetric solvent,

surface, zwitterionic copolymer, and protein interactions that lead to a molecular weight-driven sequential adsorption not seen with adsorbed PEG copolymer brushes.

4.2 Introduction

Assessing the stability of end-tethered or adsorbed copolymer coatings against blood proteins is a major challenge when using synthetic coatings for drug delivery vehicles. Immunostimulatory properties of nanoparticles may occur through various mechanisms, including antigenicity, adjuvant properties, and inflammatory responses.[152-153] Immune cells in the bloodstream and in tissues have a propensity to engulf and eliminate certain nanoparticles.[154] Adsorption of plasma proteins onto the surface of a nanoparticle can occur the instant a particle enters the bloodstream. The mechanism by which protein adsorption occurs is not completely understood. However, the specific blood proteins which bind nanoparticles have been examined. Of those, the most common are immunoglobulins and components of the complement system, as well as other abundant blood serum proteins such as fibrinogen and albumin.[155-156] There is a prevalence of literature that shows that PEG-coated surfaces, adsorbed or grafted[155, 157], resist adsorption of proteins in the blood associated with the immune system responding to foreign particles, making PEG an attractive option for increasing bioavailability of drug particles in blood.[11] However, current literature shows that PEGylated particles rely on selective adsorption of proteins to evade uptake and elimination from the blood versus the previous notion that PEG resists protein adsorption altogether.[117, 154, 158] Therefore, the demand for surfaces that resist immune system protein adsorption is of high interest and importance.

Zwitterionic polymers have been shown to exhibit ultralow nonspecific fouling (protein adsorption) and excellent biocompatibility.[21, 159-160] It is thought that more favorable segment-solvent interactions compared to segment-protein interactions explain the ultralow fouling behavior. Simulation, SPR, and ellipsometry studies explain the antifouling behavior of polyzwitterions due to their strong hydration layer via electrostatic interactions, dipole orientation, and balanced charges that minimized dipoles.[161-163] However, previous work by the author has shown that specific ion effects challenge the architecture and dimensions of zwitterionic copolymers in presence of poor solvents mediated by divalent salts.[149] Contrasting reports include the ability of some proteins to adsorb to zwitterionic coatings,[163-167] consistent with theoretical work by Halperin on protein adsorption on grafted polymer layers.[125-126, 148, 168-169] It is noteworthy that several studies on protein interactions with zwitterionic coatings consider end-grafted zwitterionic polymers,[159, 170-175] which is a reliable method to forming stable coatings, unless the surface is compromised by defects. However, previous reports, including recent work by the authors, illustrate both physiosorbed ethylene-oxide and zwitterionic copolymer coatings form defect-free, dense brushes that impart robust steric stabilization lubrication performance. Therefore, physisorption of copolymers is a simple versatile, practical, scalable, and environmentally friendly strategy for stable coatings.[24, 42, 149, 176-180]

A problem for any physiosorbed copolymer brush is the possibility for being displaced by competing species with a different molecular weight and more favorable macromolecule-surface interactions. This ‘competitive adsorption’ is an important biophysical problem made famous due to discoveries of the displacement of plasma

proteins, i.e., the Vroman effect[181] , but generally refers to the process of macromolecular displacement onto solid surfaces from solution, either coadsorption from mixtures followed by displacement, or sequential adsorption followed by displacement.[182-184] These processes have been examined for either chemically similar or chemically different macromolecules.[182-183, 185-191] Nonequilibrium adsorption and desorption dynamics highlight the importance of segment-surface interactions, adsorbed polymer density, and polymer architecture on adsorption/desorption dynamics.[186] More nuanced explanations posit that the rate of displacement depends on the interactions between polymer, surface, and solvent, and the rate of conformational changes in the adsorbed layer.[183, 192] Moreover, it is found that if the displacer macromolecule has more favorable segment-surface interactions, this drives the displacement, and thin-layer chromatography experiments suggest that the interactions between the adsorbed layer and displacer are not as dominant.[193]

Direct measurements of competitive adsorption of PEO with different charged end-groups highlight the importance of molecular weight effects by examining competitive processes for similar macromolecules differing in molecular weight.[194] Moreover, segment adsorption energy and chain flexibility dynamics control competitive adsorption kinetics have been considered as important drivers of macromolecular displacement.[195] However, kinetics and mechanism of coadsorption is highly dependent on order of addition of macromolecules.[196] Experiments on adsorbed zwitterionic copolymers onto negatively charged surfaces, using fibrinogen and lysozyme to test protein repellence, serves as a reminder that displacement of adsorbed layers can cause surface defects, whether the displacement is chemically driven, or molecular weight driven as reported in literature from

the 1950s. However, to date, there has been no assessment of dimensions, interactions, and solvent quality effects of physiosorbed zwitterionic copolymer brushes when exposed to larger, more abundant blood proteins and if any competitive or sequential adsorption behavior can be detected.

In the authors' previous works, PEG-PPO triblock copolymers irreversibly adsorb to hydrophobic surfaces, formed dense brushes, and did not desorb in good solvents, characteristic of nonequilibrium , irreversible adsorption behavior.[42, 105] We have previously shown that adsorbed PEG triblock copolymers irreversibly adsorb onto hydrophobic surfaces and do not compete with high MW blood proteins. However, a running hypothesis is that zwitterionic polymers are more promising coatings that may resist adsorption of blood proteins involved in the immune system response. To evaluate this hypothesis rigorously, direct, sensitive, non-invasive measurements of preferential or competitive adsorption between adsorbed synthetic zwitterionic copolymers and high molecular weight blood proteins must be examined. Studying the effect of high molecular weight blood proteins on surface-anchored zwitterionic polymers will elucidate the balance of segment, protein, and solvent interactions and aid in the prediction of macromolecular segregation onto colloids when introduced to blood protein solutions. This is important since controlling adsorbed layer properties requires knowledge of polydispersity-related kinetics and equilibrium layer architectures[190] via direct and sensitive spectroscopic and scanning experimental techniques.[119]

In this paper, we extend our previous study on PEG-protein interactions and employ our direct, non-intrusive, and sensitive assay, Total Internal Reflection Microscopy (TIRM) to measure the interactions and layer dimensions of high and low molecular weight

(Mw) adsorbed zwitterionic triblock copolymers (ZItb) in the presence of large, abundant blood proteins, bovine serum albumin (BSA), and immunoglobulin G (IgG), in the bulk solution (Figure 4-1A). Equilibrium analysis provides in situ, direct evidence of layer architectures formed when BSA and IgG are introduced into the bulk. Using this ultra-sensitive interaction measurement tool, we probe the fates of protein-ZItb colloidal interactions and layer architectures: protein adsorption leading to corona formation, negative protein adsorption leading to exclusion and depletion attraction and competitive adsorption of high molecular weight proteins with zwitterionic copolymers, leading to defective layers. (Figure 4-1B-E) We show that model zwitterionic copolymers, PMAPS and PMPC exhibit unique behavior in response to the introduction of blood proteins driven by the chemical structure of these zwitterionic species and molecular weight differences of these heterogonous macromolecules, standing in stark contrast to layer architectures and interactions of adsorbed PEG copolymers exposed to the same blood proteins.

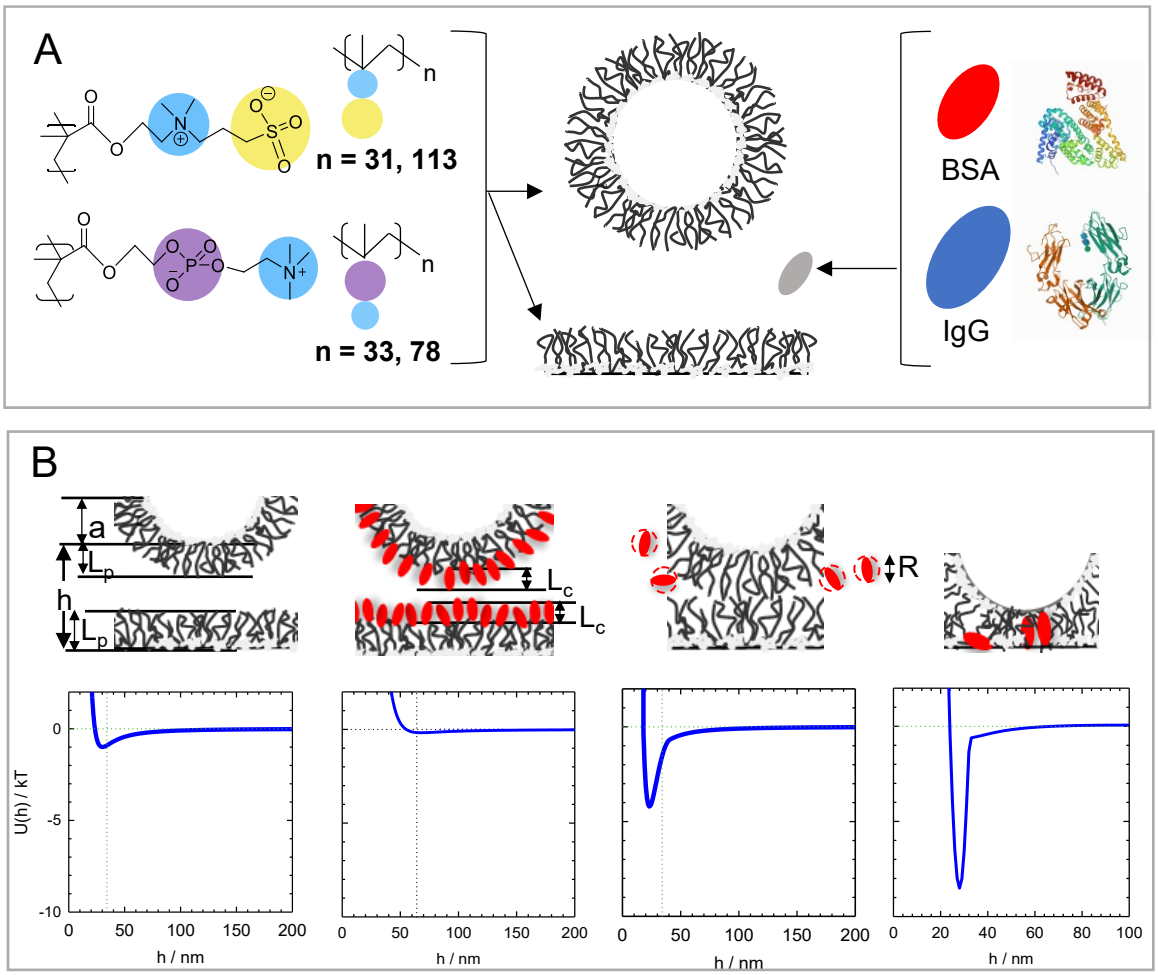

Figure 4-1 **Predictions of zwitterionic triblock copolymer (ZI-tb) layer architecture and interactions with blood proteins.** (A) Schematic of materials. Left: Zwitterionic triblock copolymer molecular detail with of both copolymers (represented by the number of repeat units of each triblock). PMAPS (top: yellow, blue), and PMPC (bottom: purple, blue). Middle: Colloid and wall geometry with adsorbed copolymers. Right: Structural renderings of BSA and IgG were reprinted with permission from PDB. (B) Schematics of possible fates of adsorbed ZItb layers in the absence and presence of blood proteins and theoretical kT-scale interaction potential. From left to right: Symmetric interactions of ZItb layers in absence of proteins; Protein adsorption/corona on the surface of PEGtb of thickness L_p+L_c with theoretical potential showing the effect of adsorbed protein; Exclusion of nonadsorbing proteins, with a dimension of R nm, with theoretical potentials illustrating depletion without change in the steric thickness; Defective layer formation due to desorption of ZItb which can cause increased vdW attraction due to thinner defective layers and/or protein and polymer bridging. Theoretical potentials show >5 kT attractive wells that induce particle deposition.

4.3 Results & Discussion

4.3.1 Interactions of BSA with high Mw Zwitterionic Copolymers

Figure 4-2A reports lateral and normal trajectories and kT-scale interaction potentials of hydrophobic silica colloids and wall with an adsorbed layers of PMPC78-tb (23.6 kDa, i.e., the molecular weight of one PMPC with 78 repeat units), with no BSA, and with addition of 20 g/L and 40 g/L BSA (from left to right). In the top row, PMPC78-tb coated colloids freely diffuse laterally over a PMPC78-tb coated wall, with no normal binding as evidenced by the persistence of grey trajectories over 30,000 frames, or 18 minutes. The z-trajectories offer a nanometer resolution of equilibrium normal height excursions for a representative particle and show a particle freely diffusing with no evidence of intermittent binding to the surface, showing that PMPC-PMPC brushes exhibit net repulsive interactions due to osmotic repulsion between PMPC-tb brushes generated at the onset of segment overlap at the layer periphery. Statistical mechanical analysis for an ensemble of particles using Boltzmann inversion in the bottom row show a superposition of attractive vdW and repulsive steric interactions between adsorbed PMPC78-tb layers. Theoretical fits that agree with our data to within ~0.2 kT allows us to resolve a PMPC78-tb uncompressed layer thickness of 25 nm.

With the addition of 20 g/L and 40 g/L of BSA into the bulk solution, followed by equilibration shows some interesting effects on the layer interactions and architectures. First, we note that there is a progression of longer binding lifetimes of PMPC78-tb coated colloids onto the wall at 20-40 g/L BSA, near physiological conditions. Since lateral trajectories might offer misleading notions of attractive protein-polymer interactions,

normal excursions of representative particles in each case show instances of longer binding, but there is no evidence of intermittent binding to the surface. This is further reflected in the potential energy profiles, where there is no shift in either the range of steric interactions, i.e., the layer thickness we measure remains 25 nm. Coupled with the binding lifetime data, BSA is likely weakly excluded from PMPC layers causing a weak depletion attractive interaction between the polymer brushes. Previous examination of such exclusion of BSA from PEG reveals that BSA might be penetrating the layer dynamically causing weak depletion attraction. Ultimately, sensitive super resolution microscopy analysis of 3D trajectories and equilibrium potentials shows that this exclusion of BSA from PMPC78-tb layers has no effect on the net thickness of layers but leads to a finite weak attraction between the particle and wall for all particles in the ensemble.

PMAPS copolymers are of interest due to their reversed dipole orientation compared to PMPC, which has been shown by the authors to lead to unique behavior in terms of its layer architecture and dimensions in response to changes in solvent quality. Figure 4-2B shows lateral and normal trajectories and kT-scale interaction potentials of hydrophobic silica colloids and wall with an adsorbed layer of PMAPS113-tb (31.5 kDa) with no BSA, and with addition of 20 g/L and 40 g/L BSA (from left to right, top to bottom). In the top left panel in Figure 3B, like PMPC78-tb, PMAPS113-tb coated colloids freely diffuse laterally over a PMAPS113-tb coated wall, with no normal binding as evidenced by the grey trajectories. The z-trajectories offer show a particle freely diffusing with no evidence of intermittent or persistent binding to the surface demonstrating net repulsive particle-wall interactions conferred by the steric repulsion between PMAPS

layers. Statistical mechanical analysis of the distribution of the height excursions for all particles shows a superposition of attractive vdW and repulsive steric interactions between adsorbed PMAPS113-tb layers. Theoretical fits show PMAPS113-tb layers have an uncompressed layer thickness of ~24 nm. While PMAPS113-tb particles free diffuse in the lateral and normal directions like PMPC78-tb layers and exhibit some longer binding in the normal direction, equilibrium analysis of interaction potentials show that the thickness of the steric layer surprisingly increased by 8 nm at both 20 and 40 g/L BSA. Although we cannot infer an exact orientation of the protein adsorbed to the surface, since BSA short axis dimensions are on the order of this time-averaged steric layer thickness increase, direct and sensitive spectroscopy here shows that BSA unequivocally adsorbed to PMAPS113-tb layers.

TIRM measurements of polymer layer thickness mediated by solvent quality changes, such as adding high molecular weight proteins, results in qualitatively different behavior for each of the zwitterionic copolymers. To explain this intricate difference, responses to solvent quality (entropic or enthalpic), and polymer interactions with BSA, which is negatively charged at neutral pH, should be considered. Lysozyme and fibrinogen were found to adsorb to polyanionic brushes.[197] It was argued that positive sites on the fibrinogen molecule allowed localized electrostatic attraction to charged polyelectrolyte segments, and neutron reflectivity measurements showed that the proteins were located on the periphery of the brush, with fibrinogen located further out than lysozyme.[198] This argument supports the implication that negatively charged BSA may have allowed for localized attractive electrostatic interactions with positively charged amine groups in the periphery of the PMAPS layer, leading to the increase in the steric thickness on the order

of the dimensions of BSA. One reasonable speculation could be that BSA-sulfobetaine interactions are favorable compared to other symmetric and asymmetric interactions, and since the sulfobetaine moiety contains a negatively charged sulfate group, BSA might adsorb by partially inserting into the PMAPS layer periphery and displace nearby water molecules.

PMPC, however, possesses a reversed dipole orientation with the cationic amine extending outwards. In this case, no corona is measured as shown in Figure 4-2. Fibrinogen and cationic proteins such as lysozyme were found to exhibit net repulsive interactions with electrostatically anchored PMPC brushes, and this is somewhat consistent with our results that negatively charged proteins do not adsorb to PMPC brushes, although the cationic amine group should theoretically allow for electrostatic attraction between BSA and the amine group. Therefore, the nature of how negatively charged BSA interacting with PMAPS, and PMPC cannot be simply explained by an electrostatic argument. It is thought that water molecule structuring around MPC groups explains its inertness to changes in solvent quality. Previous work from the author supports this hypothesis by showing that addition of NaCl (water structure enhancer) and $MgSO_4$ (water structure breaker) had no specific ion effects and no impact on the solvated dimensions of adsorbed PMPC brushes. This was explained by enhanced water structuring around MPC moieties that out-compete the presence of other mono- or di- valent ions in solution.[149] Furthermore, it is hypothesized that water molecular ordering at the polymer surface impacts protein adsorption.[199] Experimental evidence suggests that proteins cannot out-compete water molecules that hydrate MPC moieties, and thus serve as a potential explanation for why

BSA is excluded from PMPC. As shown in previous work, the depletion effect can be significantly weakened due to partitioning of proteins between the gap and the bulk solution and partial insertion into the polymer layer reducing its excluded volume. Fitting the potentials for PMPCtb in BSA solutions further confirms that a balance between these two parameters explains the weakened depletion and the fact that BSA does not adsorb irreversibly to PMPC forming a corona.

4.3.2 Zwitterionic Copolymer Desorption

Figure 4-3 shows an interesting effect with employing the same protocol but with IgG (150 kDa), another abundant blood protein with a crucial role in immunogenicity of foreign particles in blood, with >2X the molecular weight of BSA (66 kDa). In the author's previous work, IgG between 2-10 g/L were added to the bulk solution to PEG-coated surfaces. However, preliminary experiments with both PMPC78-tb and PMAPS113-tb layers at the same concentration range used previously consistently led to unstable, deposited particles (data not shown). Since TIRM is a good measure of weak interactions, lower concentrations of IgG were tested to see when particles deposit. Using 0.6-2.5 g/L IgG in the bulk solutions, PMPC78-tb and PMAPS113-tb showed a continuum of defective layer formation in this range. (Figure 4-3) While previous experiments with BSA did not reveal any desorption of the zwitterionic layers, with IgG, particles bind intermittently to the substrate (z-trajectories have longer binding lifetimes going from 0-1000s from 0-2.5 g/L IgG). Moreover, interaction potential profiles for both copolymers demonstrate heterogenous attractive wells among various particle populations characteristic of the formation of defective layers (shown as different colored effective potentials averaged over populations of particles with similar attractive wells). Therefore, our hypothesis is that

higher molecular weight IgG displaces adsorbed both PMPCtb and PMAPStb copolymers and leads to defective layers with increasing attractive interactions. What is interesting is that with a small change in IgG concentration, particles experience a quasi-first order transition from levitated to deposited at IgG concentrations below that of blood levels (6-11 g/L). To explore this hypothesis and explain a potential explanation, lower molecular weight PMPC-tb and PMAPS-tb interactions were explored.

Figure 4-4 shows lateral and normal binding trajectories and kT-scale interaction potentials of PMPC33-tb (9.7 kDa) and PMAPS31-tb (8.6 kDa) coated on both the colloid and wall with increasing concentrations of BSA from 20-40 g/L. First, lateral, and normal trajectories for PMPC33-tb with no protein show free diffusion of particles near the wall with no normal binding lifetime. Theoretical fits to the superposition of van der Waals, gravity, and steric repulsion show that PMPC33-tb forms layers with an uncompressed thickness of 16 nm. Thinner layers lead to exposure of shorter-range ~2 kT van der Waals attraction between all the particles and wall, but with the steric repulsion between the layers providing robust steric stabilization that prevent aggregation. Similar analysis for PMAPS31-tb with no protein leads to 14 nm PMAPS31-tb layers with ~1s binding lifetimes over the course of 18 minutes.

Thinner PMPC33-tb layers were not inert to high BSA concentrations. It is clear from Figure 4-4A that PMPC33-tb coated particles show longer intermittent binding lifetimes normal to the surface with more BSA added. At 20 g/L BSA, PMPC33-tb particles are bound ~100 seconds, whereas at 40 g/L, particles are bound for 100-1000

seconds to the surface as seen by the normal trajectory plots. This further reflects in the interaction potential energy profiles, where heterogenous attractive well depths increase and persist with more BSA added to the bulk solution, indicative of the formation of defective layers, perhaps due to BSA displacing PMPC33-tb polymers at certain locations across the surface. PMAPS31-tb layers also show similar trends with increasing BSA from 20-40 g/L in Figure 4-4B. Particle populations experiencing similar net attraction were grouped together and averaged within that grouping to obtain an effective potential, although these intermittent binding events are nonequilibrium, and will be discussed in more detail below. Moreover, particles seem to be stuck for longer periods of time at different intervals at 20 g/L BSA compared to PMPC33-tb, and all particles are completely deposited for more than 1000 seconds at 40 g/L BSA.

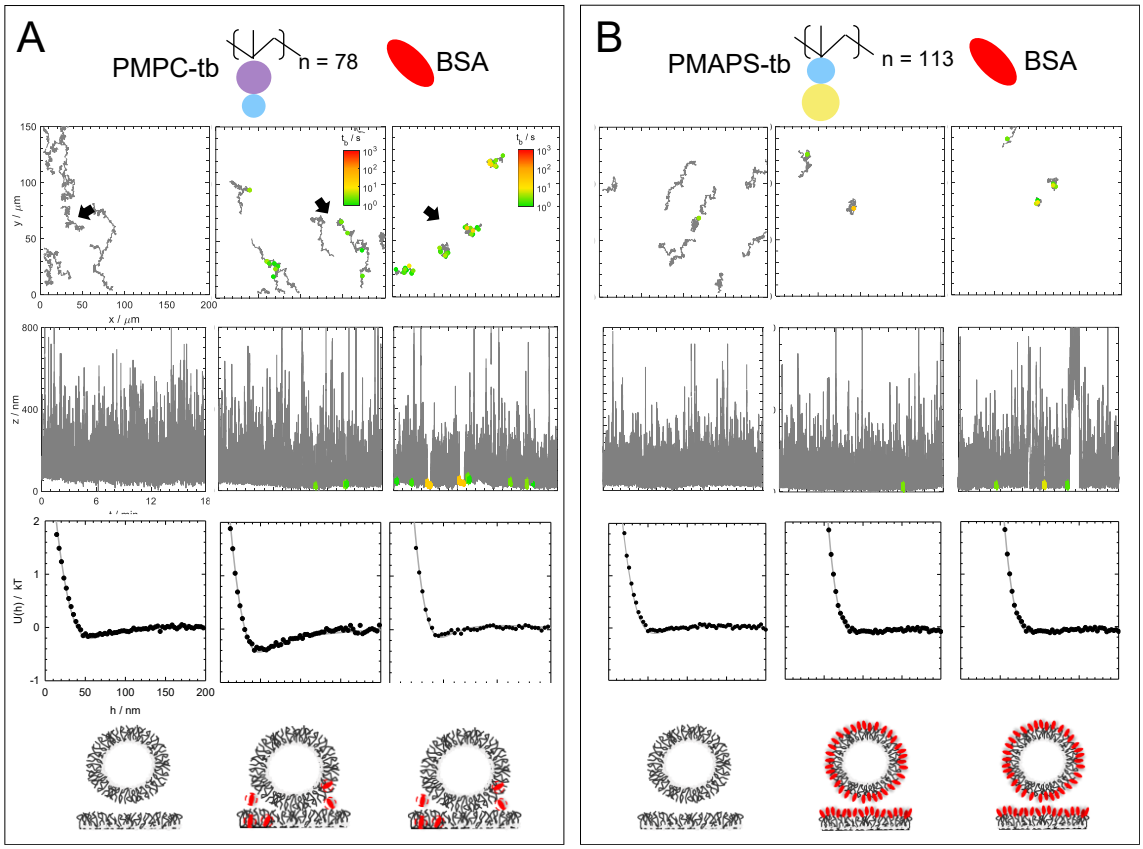

Figure 4-2 **BSA is excluded from high Mw PMPCtb but forms a corona on high Mw PMAPStb.** Scale bars in the insets illustrate the normal binding lifetime of a particle. (A-B) Top row: x,y trajectories of 2.15 μm silica colloids and wall with adsorbed high Mw PMPCtb (A) and PMAPStb (B) with 0,20,40 g/L (left to right) BSA. Center row: z-trajectory of a single representative particle (indicated by arrow) illustrates free diffusion normal to the surface for each case from left to right (0, 20, 40 g/L BSA, respectively). Bottom row: Ensemble-averaged interaction potentials is a superposition of steric repulsion and van der Waals attraction (see Methods). (A) Interaction potentials demonstrate no change in the thickness of PMPCtb, but slight increase in attractive interactions due to weak depletion. (B) Potentials show an 8 nm increase in the steric thickness from native PMAPStb thickness and a decrease in the attractive well depth, indicating longer range repulsion and that BSA may be adsorbed to PMAPStb layers.

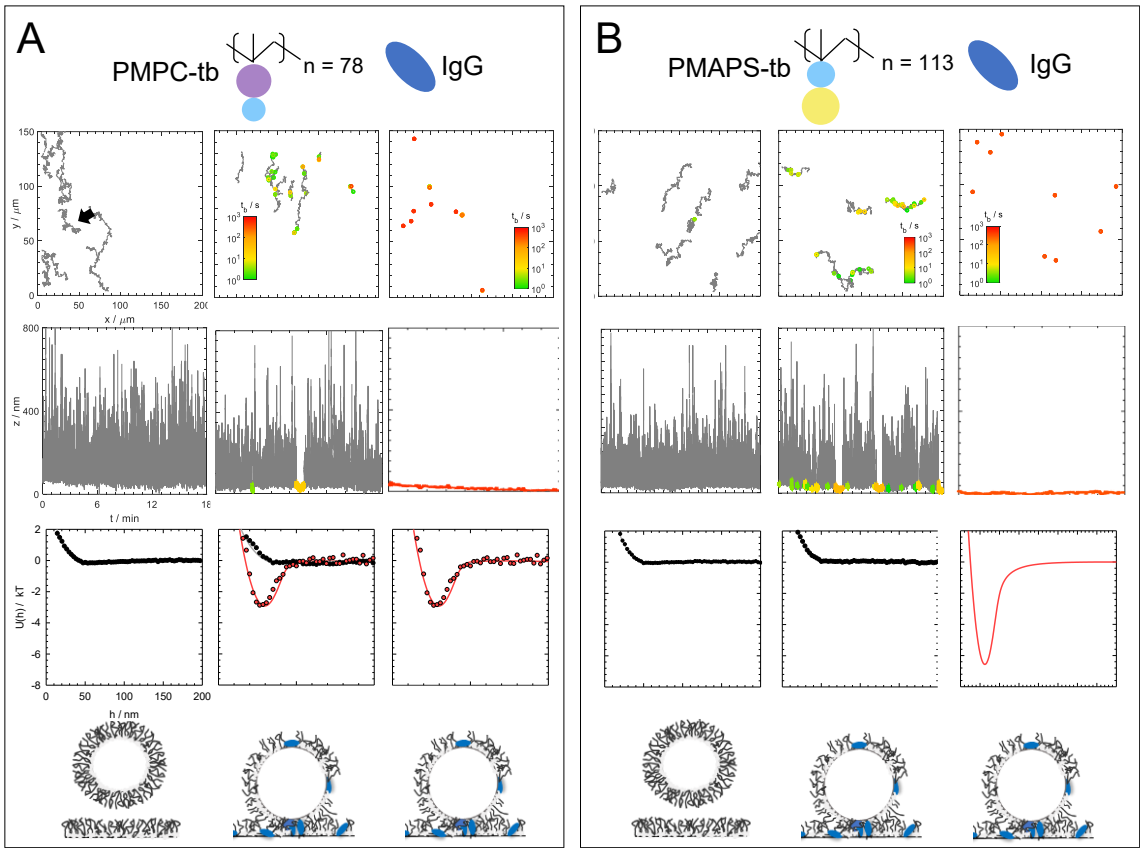

Figure 4-3 **IgG progressively displaces both high Mw PMPCtb and PMAPStb.** (A-B) Top row: x,y trajectories of 2.15 μm silica colloids and wall with adsorbed high Mw PMPCtb (A) and PMAPStb (B) with 0,1.25,2.5 g/L (left to right) IgG, Trajectories show more hindered lateral diffusion with binding lifetimes increasing from 0-1000s. Center row: z-trajectory of a single representative particle (indicated by arrow) illustrates a continuum of particle deposition normal to the surface from left to right with some particles levitated and others deposited at 1.5 g/L IgG, and particles completely deposited at 2.5 g/L. Bottom row: Ensemble-averaged interaction potentials is a superposition of steric repulsion and van der Waals attraction (see Methods). Interaction potentials demonstrate an increase in the attractive well depth, with 1.25 g/L IgG case displaying populations with different attractive well (A) and in (B) particles experience a quasi-first order transition from stable (0-1.25 g/L) to deposited at 2.5 g/L IgG.

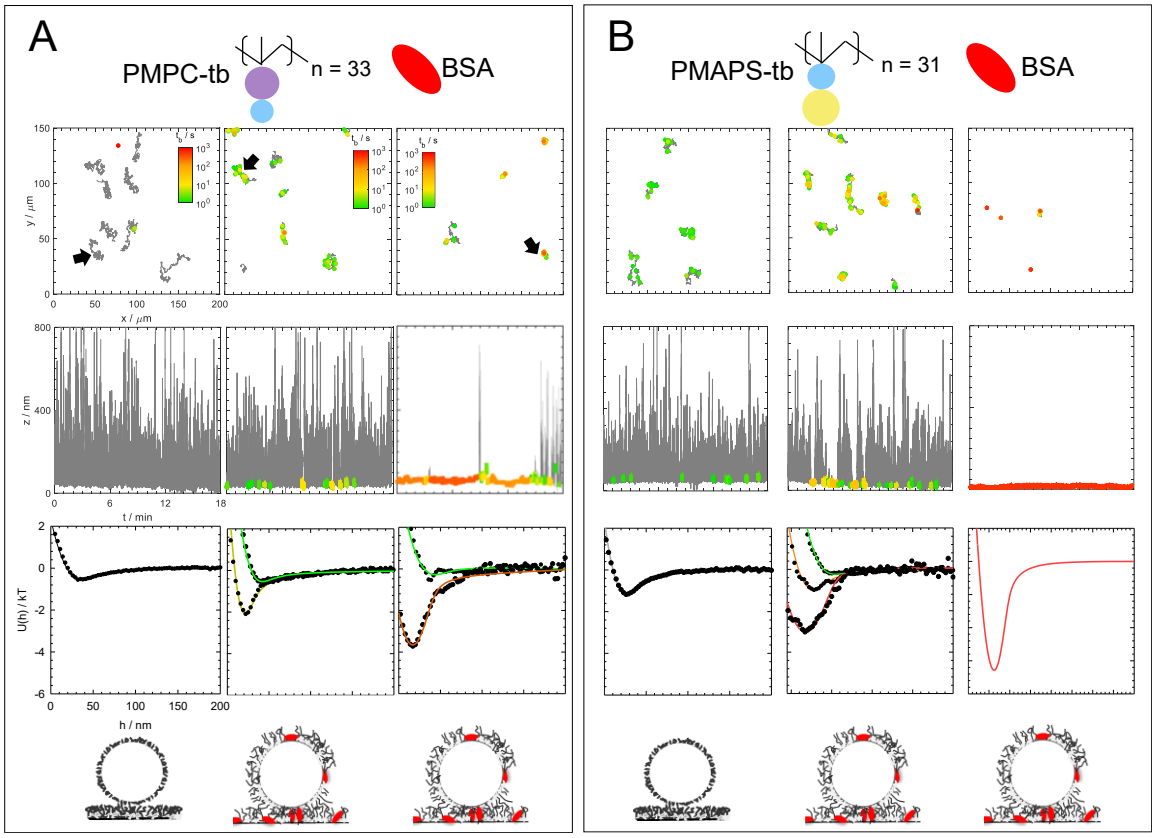

Figure 4-4 **BSA progressively displaces both low Mw PMPCtb and PMAPStb.** (A-B) Top row: x,y trajectories of 2.15 μm silica colloids and wall with adsorbed low Mw PMPCtb (A) and PMAPStb (B) with 0,20,40 g/L (left to right) BSA illustrate more hindered lateral diffusion with binding lifetimes increasing from 0-1000s. Center row: z-trajectory of a single representative particle illustrates a continuum of hindered diffusion normal to the surface from left to right with some particles experiencing 0-10s binding (green) and others experiencing 10-100s binding lifetimes (orange-yellow) at 20 g/L BSA. At 40 g/L BSA, some particles experience 10-100s binding (green-yellow), and other populations experience 100-1000s binding (orange-red). Bottom row: Ensemble-averaged interaction potentials. Interaction potentials demonstrate an increase in the attractive well depth, with 20-40 g/L BSA case displaying populations with different attractive well depths characteristic of defective layers that cause deposition.

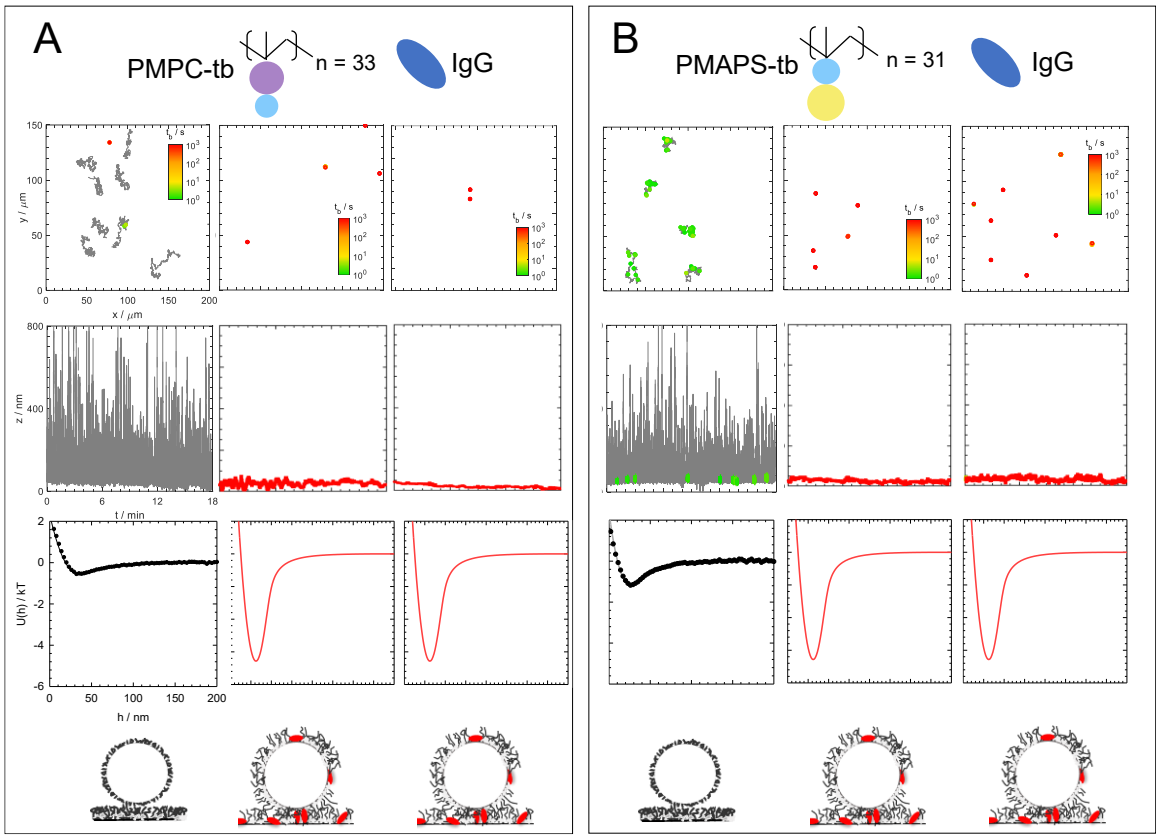

Figure 4-5**. IgG displaces both low Mw PMPCtb and PMAPStb.** (A-B) Top row: x,y trajectories of 2.15 μm silica colloids and wall with adsorbed low Mw PMPCtb (A) and PMAPStb (B) with 0,1.25,2.5 g/L (left to right) IgG, Trajectories show more hindered lateral diffusion with binding lifetimes increasing from 0-1000s. Center row: z-trajectory of a single representative particle (indicated by arrow) illustrates particle deposition normal to the surface from left to right with some particles deposited at 1.25-2.5 g/L IgG. Bottom row: Ensemble-averaged interaction potentials is a superposition of steric repulsion and van der Waals attraction (see Methods). Interaction potentials demonstrate a significant increase in the attractive well depth.

More dramatic results occur with both PMPC33-tb ad PMAPS31-tb layers with addition of IgG from 0.6-2.5 g/L. Figure 4-5 shows progressive desorption of PMPC33-tb and PMAPS31-tb, respectively, with 0-2.5 g/L from left to right, and both normal trajectories and potential energy profiles revealing stuck particle potentials from top to bottom for each copolymer. It seems from these experiments that <0.6 g/L IgG is needed to create defective zwitterionic copolymer layers and increase the net attractive interaction between the particle and wall until full deposition. In conclusion, Figure 4-4 and Figure 4-5 illustrate direct and sensitive evidence using a combination of 3D equilibrium trajectories

and potential energy profiles to show that BSA and IgG, both significantly higher Mw compared to the adsorbed zwitterionic triblock copolymers, form defective layers on both PMPC33 and PMAPS31 layers at near physiological concentrations. This supports the hypothesis that there is a molecular weight- and enthalpic-driven displacement of higher molecular weight proteins and zwitterionic triblock copolymers, truly unique to the behavior of PEG copolymers (15 kDa).

4.3.3 Argument for Zwitterionic Copolymer Displacement by Large Proteins

Previous work from the authors shows that ZItb copolymers desorb after washing steps, indicating of equilibrium adsorption behavior. Therefore, our strategy has been to add 30 ppm ZItb to the bulk solution to drive equilibrium to the surface, and we have applied this strategy in this work. However, even with this strategy, results in Figure 3A and Figure 4-4 show varying levels of attractive well depths at higher BSA and IgG concentrations for PMPCtb and PMAPStb-coated colloids and walls. This can be misinterpreted as a protein-mediated attraction. However, these results show heterogenous intermittent binding events varying in space and time over the surface. Our analysis is based on equilibrium sampling of heights of a single colloid over a wall, but the individual particle "effective" potential profiles in Figure 4-3A, and Figure 4-4A-B include both levitated (gray trajectories) and bound (orange-red trajectories) height excursions where the bulk of the particle excursions are measured in the bound state rather than the levitated state causing heterogenous deep attractive wells, i.e., the histograms are skewed to the bound state.

Therefore, this results in averaged potentials for particle ensembles or 'groups' experiencing similar attractive wells. Previous work in our group has shown that subtracting the longer binding events from the normal trajectories results ion potential profiles that collapse onto each other and resemble potential profiles and trajectories of particles that are freely levitated on the surface. Although our results cannot distinguish if the defective layers were formed on the colloid or the wall or both, by comparison to control experiments with no proteins (no defective layers on either surface), we speculate the displacement may occur on either surface leading to heterogenous binding events. What implies is that the observed intermittent binding is due to local attraction of a colloid and/or wall with a defective steric layer diffusing on a heterogeneous surface due to polymer displacement by large proteins.

It is important to note that TIRM measures equilibrium particle dynamics, and we do not measure the initial kinetics of displacement, rather we measure interactions and layer architectures in nonequilibrium situations. As explained previously, there is a large body of work on the kinetics of displacement of homogeneous and heterogenous adsorbed macromolecules. Typical arguments for similar macromolecules include the variation in molecular weight and surface affinity that leads to displacement and potentially coadsorption over longer periods, which has been the main observation for the Vroman effect. However, more nuanced explanations posit that the rate of displacement depends on the interactions between polymer, surface, and solvent, and the rate of conformational changes in the adsorbed layer, i.e., the dynamic stiffness of the polymer chain.[183, 192] While it is not within the scope of this work to calculate thermodynamic parameters, our direct

equilibrium interaction experiments draw a picture on the potential balance of interactions that lead to the defective layers.

Typically, macromolecule adsorption requires a decrease in the total free energy, and this is mediated by polymer adsorption energy, loss of conformational entropy, and the entropy of mixing and de-mixing. Therefore, adding another chemically dissimilar macromolecule and with a different molecular weight should theoretically affect each term in the total free energy. In thermodynamic equilibrium, therefore a small difference in segmental binding energy is enough to lead to very pronounced adsorption preference.[200] It is found that if the displacer macromolecule has more favorable segment-surface interactions, this drives the displacement, and thin-layer chromatography experiments suggest that the interactions between the adsorbed layer and displacer are not as dominant.[193]

In this work, when the molecular weight differential was great enough, adsorption preference of the proteins to the surface was more readily visible since both larger proteins seemed to create defective layers at low concentrations within 10 minutes of equilibrating the sample prior to measurement (data not shown). However, molecular weight differentials between dissimilar macromolecules are not the only explanations for displacement. Our previous work shows that adsorbed PEG copolymers (PEG Mw = 15 kDa) was not displaced by either BSA or IgG at much higher concentrations than what was used in this work, suggesting that Peg was irreversibly adsorbed regardless of the change in solvent quality mediated by proteins, and highlights the importance of layer architecture and interactions.

Therefore, we posit that zwitterionic moieties experience solvent quality-driven desorption mediated by preferential protein-surface interactions at the expense of zwitterionic-surface interactions, driving the formation of defective layers. By comparing zwitterionic copolymer behavior against PEG copolymers, it seems grafting zwitterionic copolymers might circumvent desorption, but these layers may not be totally inert to large blood protein, unlike adsorbed PEG copolymers, which demonstrate their robust steric stabilization in wider ranges of solvent quality mediated by dissimilar macromolecules. Future work could include an assessment of grafted zwitterionic copolymers using TIRM against BSA, IgG, and protein mixtures.

4.4 Conclusions

3D trajectories and *kT*-scale interactions potentials via a nonintrusive and direct assay utilizing diffusing colloidal probes were used to examine symmetric interactions of adsorbed zwitterionic triblock (ZItb) copolymers, PMPCtb and PMAPStb, at high and low molecular mediated by solutions of high molecular weight blood proteins, BSA and IgG. BSA, at physiological concentrations, was found to be weakly excluded from high Mw PMPCtb but formed an adsorbed layer (corona) on high Mw PMAPStb. IgG, an order of magnitude higher Mw than both copolymers lead to the formation of defective layers on the particle and wall. Similar symmetric interaction assays with lower Mw PMPCtb and PMAPStb confirmed the hypothesis that proteins may be displacing zwitterionic copolymers off the surface leading to defective layers that cause local binding events on heterogenous surfaces. Normal trajectories show a succession of increasing timescales of intermittent binding events until colloids are completely deposited at 2.5 g/L IgG and 40 g/L BSA for both copolymers.

Our results in this work are significant in that they contrast significantly with similarly physiosorbed systems with PEG that did not show desorption, i.e., PEG was irreversibly adsorbed to the colloid and wall and the layer was intact at high BSA and IgG concentrations. Our results therefore indicate not only a molecular weight-driven displacement, which has been suggested I previous literature, but suggests an interplay of segment, surface, protein, solvent interactions that favor protein adsorption on the surface compared to zwitterionic copolymers. Even though TIRM was not used to measure kinetics of displaced layers, equilibrium analysis shows the effect of long-term displacement on the intactness of the adsorbed layer and suggests a potential examination of the kinetics of zwitterionic polymer-protein displacement. Ultimately, our results show that while adsorbed systems are easy, scalable, and seem to form intact layers with PEG copolymers, zwitterionic copolymers have more complex, nonnegligible interactions with blood proteins and may not be inert to blood proteins at physiological conditions when these copolymers are physiosorbed to the surface.

4.5 Methods

Surfaces: PMPC-b-PPO-b-PMPC (PMPC copolymers), and PMAPS-b-PPO-b-PMAPS (PMAPS copolymers) were synthesized using activator regenerated by electron transfer-atom transfer radical polymerization (ARGET-ATRP) in a previously described method. To develop compact notation for each copolymer used, we abbreviate the three copolymers as: PMAPS 113 (31.5 kDa), PMAPS 31 (8.6 kDa), and PMPC 78 (23.6 kDa), and PMPC 33 (9.7 kDa), which are based on repeat units of each polymer. The molecular weights correspond to the molecular weight of one zwitterionic polymer extending into solution based on the molecular weight of the repeat units, MPC and MAPS (not including

PPO midblock). 66 kDa lyophilized bovine serum albumin (>99% purity, essentially gamma-globulin free) and 150 kDa γ-Globulin from bovine blood (≥99% purity, mixture of IgG (80%), IgM (10%), and IgA (<10%)) were obtained from Sigma Aldrich and used without further purification or modification. For brevity, bovine serum albumin will be referred to as BSA, and γ-Globulin will be referred to as IgG, since most of the bovine γ-Globulin sample is composed of IgG. Both protein stock solutions were prepared in 150 mM NaCl and sonicated for 30 minutes. Glass microscope slides (Fisher) were cleaned and rendered hydrophobic according to protocols in previous publications from this group. Briefly, glass slides were cleaned in acetone, 100 mM KOH, and DI water, and rendered hydrophobic by spin coating polystyrene. Silica colloids of nominal 2.2 μm diameter (Bangs Laboratories) were rendered hydrophobic by coating with 1-octadecanol (Sigma-Aldrich). Despite different chemical functionalities on hydrophobic particle sand slide surfaces, prior studies have shown the same triblock copolymers in this study yield the same solvent quality dependent thickness even with two different coatings.[149]

Polymer Adsorption. 1000 ppm of all copolymers used were dissolved in 150 mM NaCl and added to vacuum grease-sealed O-rings on a hydrophobically modified glass slide and left to equilibrate overnight, and 1000 ppm of all copolymer solutions were added to 2 uL of hydrophobically modified 2μm glass particles overnight. 1 μL of the triblock-silica dispersion was then added to the triblock adsorbed on the slide and left to equilibrate in 150 mM NaCl for two hours. An equal volume of 2x the final desired concentration of the protein solution was added to the particle-wall system and left to equilibrate for two hours prior to measurements.

Microscopy: Ensemble TIRM was used to measure interactions between polymer coated colloids and slide as described in previous work. In summary, an evanescent wave is generated via reflection of a 633 nm HeNe laser (Melles Griot) onto a prism at 68 degrees. Images are captured using a 40× objective (LD Plan-NEOFLUAR), using a 12−bit CCD Camera (Hamamatsu Orca-ER) at 4 binning, 4 ms exposure, and a frame rate of 28 frames per second. In the TIRM experiment, scattering intensity, I, of a spherical colloidal particle in an evanescent wave is used to determine relative particle-wall separation, h. Measurements of single particle potentials are averaged to obtain ensemble average potentials.

Analysis: The net potential energy for ZItb-stabilized colloids and substrates, u_N, in the presence of proteins added to the bulk solution may be given by a superposition of potentials due to van der Waals attraction, u_V, steric repulsion, u_S, and gravity, u_G, and depletion attraction, u_D, as,

$$u_{\text{net}}(h) = u_G(h) + u_V(h) + u_S(h,L) + u_D(h,L)$$
$$u_{\text{net}}(h) = (4/3)\pi a^3 \left(\rho_p - \rho_f\right) gh - A_H a h^{-2} + \Gamma \exp\left[-\delta\left(h - 2L\right)\right] - \Delta\Pi V_{EX}\left(h,L\right) \quad (4)$$

where h is particle-wall separation. Subscripts refer to interactions as: (V) van der Waals, (G) gravitational, (D) depletion, and (S) steric. The gravitational potential energy of each particle depends on its elevation above the underlying surface multiplied by its buoyant weight, where ρ_p and ρ_f are the particle and fluid densities. van der Waals attraction for sphere-plate are predicted from the rigorous Lifschitz theory where A(l) includes retardation and screening for the silica colloids and glass substrates used in this work, but can be modeled by a simple power law, as described in previous work. Steric

repulsion due to compression of macromolecular brushes are modeled using a soft exponential decay that fits the Milner brush theory until 50% compression of the brush. In our model, the pre-factor, Γ, is 0.1 kT and reflects the polymer layer repulsion upon contact at $2L_0$ as well as the limit to the sensitivity of our measurement technique. δ is the decay length of the exponential, which is defined as 0.281 nm^{-1}, and L is the thickness of a zwitterionic layer here defined as $L = L_p$.

If a protein fully coats the adsorbed zwitterionic layers on both the particle and wall, a bilayer or protein corona is formed. From Eq. 1, we see that the adsorbing of proteins on the PEGtb coatings will impact the range of steric repulsion. In this case, L is the total measured layer thickness, which will be composed of the polymer thickness, L_p, and the measured protein corona thickness, L_c, which becomes $L = L_p + L_c$. Nonadsorbing proteins may be partially or totally excluded from the gap between the polymer-coated colloid and substrate resulting in depletion attraction between particles and the underlying wall surface, u_D (h, L), and is reflected in the net potential as shown in Eq. 1 using a modified AO-depletion potential. In short, ΔΠ, shown in Eq 1, is the protein's osmotic pressure difference given as the ideal contribution modified by compressibility factors inside and outside the excluded volume region, Z_i and Z_o respectively as shown in Eq 2, below. Z_i and Z_o are modeled by the Carnahan-Starling equation of state as a function of bulk and gap number densities of the protein and has been shown to sufficiently describe nonideal behavior of globular proteins in physiological ionic strength, where the Donnan effect is negligible.[142]

$$\Delta\Pi = \Pi_o - \Pi_i = \rho_o kT\left(Z_o\left(\rho_o\right) - Z_{in}\left(\rho_i\right)\cdot\langle K\rangle\right) \tag{5}$$

Here, ρ_o is the depletant number density outside the excluded volume region, and <K> is the partition coefficient defined as $\langle\rho_i\rangle/\rho_o$ (where $\langle\rho_i\rangle$ is an average number density of proteins inside the excluded volume region) modeled in Edwards et al. The expression to model the excluded volume region between a hard depletant and hard sphere, V_{EX}, is typically given as,

$$V_{EX}(h,L) = \pi\left(\frac{4}{3}R^3+\frac{4}{3}aR^2-4aRh+ah^2-Rh^2+\frac{h^3}{3}\right) \quad (6)$$

where R is the depletant's effective hard-sphere radius, which is fixed from fitting literature values of osmotic pressure of BSA and IgG to the Carnahan-Starling EOS. However, neither the globular proteins used in this study nor the adsorbed polymer layers satisfy the conditions for a hard surface, so we propose the use of a single adjustable parameter, f, to account for the softness of both the proteins and polymer. We can do this by modifying h to be $h = h - f2L$ where f accounts for proteins penetrating the PEGtb layer. We propose adjusting experimental potentials with adjusting either P or f to fit the depletion potential. The first limiting case is when $\langle K\rangle = 0$, and f is the sole adjustable parameter. Conversely, the other limiting case is when f = 1 i.e., when the protein is assumed to not penetrate the ZItb layer but is allowed to partition inside and outside the gap between the particle and wall, i.e., $\langle K\rangle \neq 0$. However, we realize that there can be an infinite number of solutions between these two limits that fit our experimental results. To our knowledge, there is no theoretical model of the average partition coefficient, $\langle K\rangle$, of soft globular proteins between soft polymer layers. So, we propose that $\langle K\rangle$ could be approximated by more rigorous theoretical approaches, as mentioned previously. We use

this approximation to estimate the theoretical average partition coefficient, and thus predict $\Delta\Pi$ and corresponding f that fits our results to self-consistently explain proteins being excluded from the gap and penetrating the polymer brush.

In solutions of macromolecules with varying molecular weights, dimensions, and interactions, displacements may be possible as explained in the text. Displacement of zwitterionic copolymers (desorption) by high molecular weight proteins may lead to defective layers. These defective layers may cause thinner steric layers (vdW attraction increases) or lead to heterogenous bridging potentials between proteins or polymers. All in all, desorption and displacement may lead to defective layers either increasing attraction or decreasing repulsive interactions between the particle and wall.

To summarize, we can use our ultra-sensitive technique and analysis to probe and model the net interactions between ZItb coated particles and wall with and without proteins in the bulk solution. Our non-intrusive, highly sensitive measurement technique and analysis method will provide us unambiguous understanding of how exactly proteins modulate the thickness of the steric layer and/or the amount of depletion attraction due to protein exclusion from the gap, or defective layer formation due to competitive displacement, with nanometer- and kT-resolution.

5 KT-SCALE REPULSION BETWEEN POLYMER-COATED COLLOIDS AND MUCIN

5.1 Abstract

In this paper, we report direct and sensitive measurements of weak interactions, or the order of ~kT, between zwitterionic (ZI) and ethylene oxide (PEG) coated microparticles with adsorbed mucin in various solution conditions such as low pH, excess mucolytic agents, and calcium chloride. By employing Total Internal Reflection Microscopy (TIRM) to measure ensemble colloidal interactions against adsorbed mucin, we exploit stochastic motion of diffusing colloidal probes, a natural gauge for equilibrium weak interactions, in conjunction with super resolution microscopy and rigorous theoretical modeling. Our method is the key to reconciling the relationship between polymer chemistry and interactions with mucus in a non-intrusive, sensitive, and direct way, unlike the state-of-the-art techniques existing. We find that both ZI and PEG copolymers exhibit long-range repulsion with mucin independent of the polymer's molecular weight and mucus structure in physiological ionic strength. Addition of excess mucolytic agents (DTT), calcium chloride, and lowering pH shows no evidence of net attractive, mucoadhesive, interactions even if the structure of adsorbed mucins may be radically different. Ultimately, our results demonstrate that nanoparticles with PEG and ZI coatings are unequivocally repulsive towards mucin which suggest that these particles may diffuse through mucus. Our findings provide a strong template for tuning polymer coatings to weakly and specifically adhere to mucus to achieve a balance of mucopenetration and mucoadhesion behavior for successful colloid permeability through mucus networks.

5.2 Introduction

Mucus is a complex biopolymer barrier located in airways, gastrointestinal, reproductive, and ocular tracts.[201-203] Major components of the mucus layer are biopolymers known as mucins, suspended in solution or membrane bound,[204-205] which are complex glycoproteins characterized by the presence of at least one large region of polypeptide with grafted oligosaccharides terminated with cysteine residues (Figure 5-1).[206] Due to the presence of the sialic and sulfonic acid residues along the bottlebrush structure, mucins are anionic at neutral pH.[207-209] There is significant interest in designing drug-bearing colloids to successfully permeate mucus. Several studies have shown that successful particle transport through mucus occurs if particles: are small enough to fit inside the porous network (<500 nm),[204, 210] possess chemical moieties to circumvent interactions with non-glycosylated protein regions, or are electrically neutral.[211-213] It is believed that the network structure of mucins, dominated by covalent and non-covalent interactions within the polymer network, are dependent on pH and calcium, both of which vary across different regions in the body,[214-218] and may be affected by presence of reducing agents that may break the mucus network by reducing disulfide bonds or oxidizing agents that increase disulfide cross-linking, which has been linked to diseased states (Figure 5-1D-F).[219-224] Although a large body of work loosely identifies relevant interactions that explain macroscopic colloid-mucus behavior, there is no definitive, quantitative relationship between structure of mucus, mediated by its physiochemical environment, and interactions with polymer-coated colloidal particle. Therefore, there is a need to identify, and sensitively measure polymer/mucin interactions that affect particles being able to permeate the mucosal network.[225]

Interactions of colloidal particles in complex, crowded environments such as mucus include both conservative forces such as electrostatic, van der Waals, and steric interactions, as well as non-conservative forces due to hydrodynamic interactions.[226] Particles that display no appreciable diffusion in mucus could result from either strong repulsive interactions in highly confined pores or strong attractive interactions in a large open pore.[38, 227-228] For example, strong van der Waals attraction could cause a particle to deposit irreversibly in mucus, which would prevent diffusion. Likewise, viscous drag due to hydrodynamic interactions between particles and pores within mucus also provides resistance to particle diffusion. Mucoadhesive mechanisms involve net attractive interactions between the colloid and mucus, spreading on the biological substrate, and, lastly, an interpenetration between polymer chains and mucins with the formation of physical entanglements between the two macromolecular species.[229-230] Mucopenetration, on the other hand, involves net repulsive interactions that can drive diffusion of colloids through mucus, if the thermodynamic driving force to partition into mucus exists. We hypothesize that an integrated strategy can be optimal for successful delivery across mucus, i.e., we believe that a balance of kT-scale attractive interactions that allow particles to partition into mucus, along with sufficient repulsive interactions to prevent irreversible adhesion might be the key to achieving successful delivery of colloidal particles with synthetic polymer coatings.

Particle diffusion through networks like mucin, has a complex dependence on colloidal and macromolecular interactions that can complicate quantitative analysis and, in some cases, even confuse qualitative interpretation. A large body of foundational work on solute partitioning into hydrogels and diffusion through porous networks offers nuance and

fundamental insights often overlooked in mucus drug delivery studies. Hindered diffusion of solutes in porous structures has been rigorously modeled and posit that a thermodynamic driving force for solutes partitioning from bulk solution into a pore, on the order of kT, must be greater than one for successful partitioning. For permeability, the solute must be able to diffuse through the porous network governed by excluded volume, nonspecific and specific interactions and.[231-236] Key parameters that must be characterized are the equilibrium solute partition coefficient and the solute diffusion coefficient.[237] Therefore, the first objective should be to measure colloid-mucus interactions on the kT-scale, relevant for drug delivery to predict the ability of a drug particle to permeate through mucus. Our hypothesis relies on the fact that kT-scale, repulsive interactions allow colloids to diffuse through mucus.[38] This strategy emphasizes the need to interrogate both conservative and non-conservative forces between particles and mucus provides a basis to understand basic interactions critical to particle mucus penetration.[225, 229]

In synthetic polymer systems, permeability has been shown to be enhanced through surface functionalization with polyethylene glycol (PEG). PEG is the most widely applied polymer in drug delivery, and has been empirically shown to have mucopenetrative properties.[10, 209, 238-239] The popularity of PEG is based on its chemical structure, which allows only a very limited amount of interactions with other molecules making PEG nonfouling.[5, 240-241] However, PEG coated drug carriers have also been shown to be mucoadhesive.[242-247] It has been suggested that low PEG molecular weight and high PEG surface coverage are required for rapid mucus penetration, whereas that high molecular weight PEG can increase mucoadhesion, contradicting well-established theory and experiments on steric stabilization, which leads to misleading notions on colloidal

therapeutic deisgn.[105, 149, 248] In parallel, there is growing evidence demonstrating that polyzwitterions outperform PEG in resistance to non-specific protein adsorption from plasma and blood serum.[209, 249] Inspired by nonadhesive viruses that can easily diffuse through mucus with hydrophilic surfaces that are net neutral, but contain equal numbers of positive and negative charges, zwitterionic micelles have recently been shown to diffuse through mucus an order of magnitude faster than PEG coated particles. Based on these findings, it seems it is important to avoid strong mucoadhesion, but purely repulsive interactions (e.g., PEG) appear to be improved by net neutral positive and negative groups (e.g., zwitterions) that interact favorably with heterogeneous mucus structure including weak intermittent specific binding (e.g., to sialic acid groups).[212] Recent work by the authors has shown how zwitterionic polymer interactions with each other depend on pH, salt concentration and type, and dipole orientations, with significant differences to PEG, consistent with the potential promise of zwitterionic polymers for mucus penetration.[42, 65]

Current methods to interrogate mucoadhesion and mucopenetration behavior of polymer-coated colloids do not provide direct evidence of the nature of polymer-mucin interactions. Common indirect experimental techniques include mean squared displacement,[16, 250-252] which is limited in temporal and spatial resolution and does not directly relate interactions to diffusivity, zeta potential, which is an average surface property and has been shown previously to not be a suitable indicator for particle-mucus interactions and diffusivity,[38, 253] measurements of adsorbed amounts of particles on mucus layers measured via QCM-D, which are limited by surface defects leading to potentially misleading results when interpreting interactions, and rheological measurements, employed to measure viscoelastic properties of mucus in response to

physiochemical changes, which reveal little about the nature of interactions at the molecular level.[214, 230, 250, 254-256]

More direct experimental techniques have been developed to measure colloid-mucus forces more. Surface force apparatus (SFA) measurements reveal weak attractive forces between PEG and mucin, albeit these weak attractive forces may be influenced by surface defects on adsorbed layers and must be carefully interpreted.[28] Surface force balance (SFB) was used to measure friction and lubrication between two adsorbed layers of mucin.[257] Atomic force microscopy (AFM) was used to measure forces between adsorbed polymers on a 20 μm colloidal probe versus an adsorbed mucin layer.[258-259] While these techniques offer substantially more direct, rigorous information, it is important to note that SFA/SFB and AFM rely on the application of external force to perturb the system, where the sensitivity is limited by the spring constant. Secondly, these techniques measure static thermodynamic conditions which is not representative of the Brownian motion of drug colloidal particles while diffusing through mucus. Lastly, SFA/SFB and AFM measure forces six orders of magnitude stronger than the forces Brownian particles experience during diffusing through porous structures like mucus, and while these techniques offer insights for lubrication and friction for biomedical and tissue engineering applications, drug permeability and diffusion occurs at six-seven orders of magnitude weaker forces, or at interaction energies on the order of kT.[30-31, 260] Consequently, there is a need to employ an experimental assay that directly measures polymer-mucin interactions at the kT-scale, with minimal perturbation of the colloids above the surface to reconcile the variability in findings from preceding literature and build a more reliable framework for designing colloidal therapeutics for delivery across the mucus barrier.

Numerous studies have characterized colloidal particles diffusing within and/or adhering to mucus, but none have directly measured interactions between particles and mucus. Additionally, many studies have examined the effect of mucin structure on its thickness and rheology, demonstrated by either increasing the degree of networking within the mucus or breaking internal structure (Figure 6-1 D-F). However, none of have examined the effect of mucus thickness and network density on their resulting interactions with colloidal therapeutics. In addition, the effects of molecular weight of polymer-coated colloids have not been compared extensively in literature, and it is important to provide these insights to help guide engineering design requirements for drug delivery vehicles through mucus suing state of the art PEG and zwitterionic coatings. In this paper, we use total internal reflection microscopy (TIRM) to directly measure carrier-mucus interactions via direct kT-scale measurements of biomaterial interactions. We use our interaction measurements to probe polymer molecular weight and mucus networking effects by varying pH, calcium, and adding mucolytic agents (Figure 5-1 G-I) to systematically and rigorously show that all these variations lead to net repulsive, weak interactions between the polymer coated colloid and mucin.

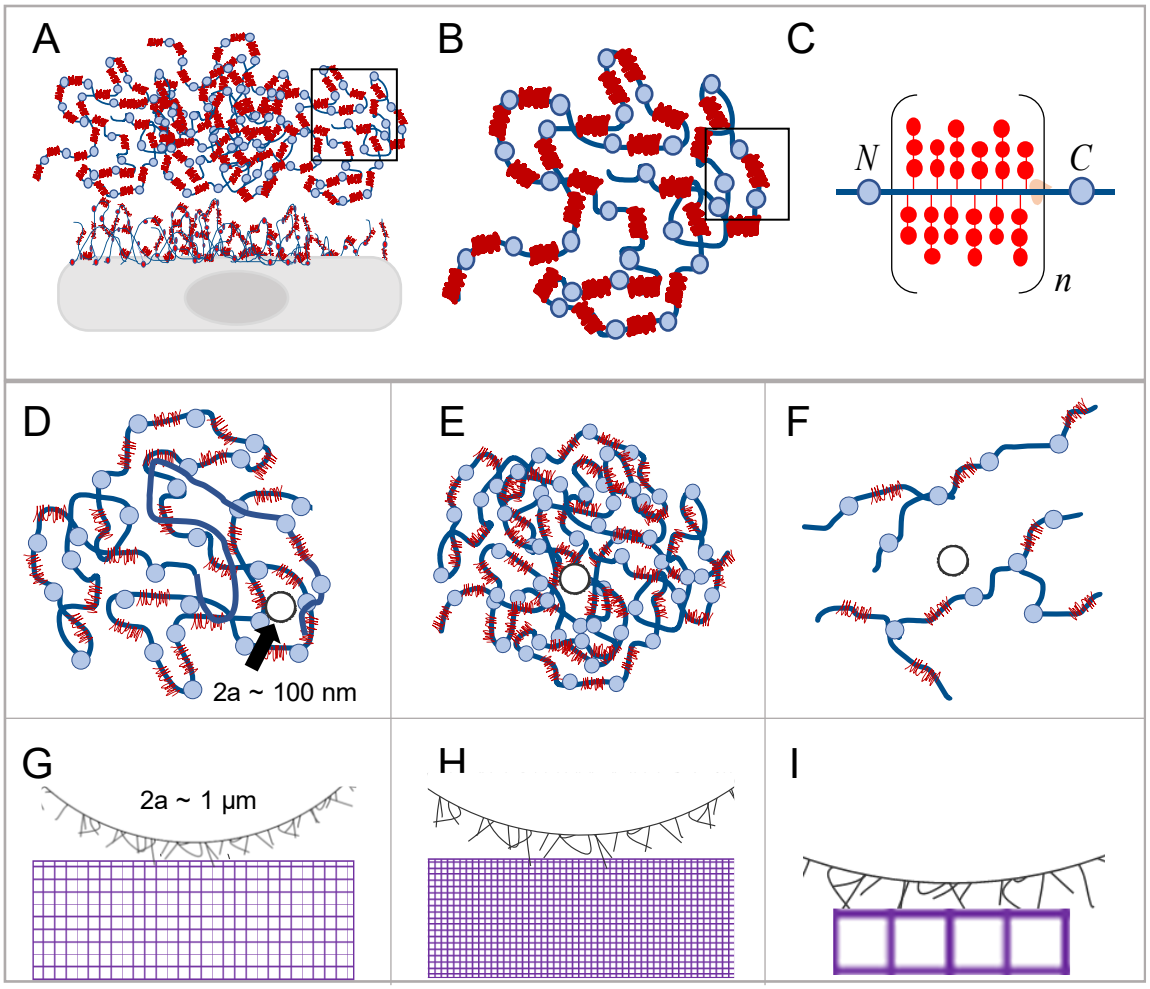

Figure 5-1 **Schematic illustration of mucins, solution conditions that affect its structure, and corresponding diffusing colloid probe geometry for each condition.** (A) Schematic representation of goblet cells (grey) with membrane-bound mucins (blue and red) and secreted mucins, enlarged for clarity. (B) Zoomed in schematic of secreted mucins composed of mucin monomers connected via disulfide bonds (blue). (C) Zoomed in schematic of a mucin monomer. A protein backbone (blue line) with grafted oligosaccharides (red) linked by disulfide bonds between cysteine groups (blue circles) at the N and C termini. (D) Simplified structure of secreted mucins in neutral pH, 150 mM NaCl. Nanoparticles (NPs) can penetrate mucus if they are smaller than the pore size. (E) Schematic of mucins with heavier cross-linking density due to either low pH or high calcium, decreasing the mucus pore size and preventing penetration of polymer coated NPs. (F) Schematic of the effect of mucolytic agents such as DTT. DTT reduces disulfide bonds between cysteines and increase the overall pore size of mucus. (G) Illustration of particle-wall geometry with a polymer-coated microparticle above a mucin-coated wall with some degree of cross-linking at physiological conditions (purple grid). (H) Illustration of particle-wall geometry with a polymer-coated microparticle over a mucin layer with higher cross-linking. (I) Illustration of particle-wall geometry with a polymer-coated microparticle over a mucin layer with lower cross-linking density and thinner mucin layers.

5.3 Materials and Methods

5.3.1 Materials

Surfaces: The commercial PEO_{141}-PPO_{51}-PEO_{141} (F108) copolymer and PEO_{76}-PPO_{51}-PEO_{76} (F68) copolymers were donated by BASF without further modification.[261-262] Two repeat units of PMPC-b-PPO-b-PMPC (80 and 33 repeat units), and PMAPS-b-PPO-b-PMAPS (113 and 31 repeat units) were synthesized using activator regenerated by electron transfer-atom transfer radical polymerization (ARGET-ATRP) in a previously described method. To develop compact notation for each copolymer used, we abbreviate the three copolymers as: F108/F68, PMAPS 113/PMAPS 31, and PMPC 78/PMPC 33, which are based on repeat units of each polymer. The adsorbed triblock copolymer is abbreviated by its end blocks with the suffix "-tb" to indicate 'triblock'. Poly(allylamine) hydrochloride (Sigma), PAH, was used without further purification. Bovine mucin from submaxillary glands. BSM, (Sigma-Aldrich, without further purification) was dissolved at 1 mg/mL in 150 mM NaCl, 10 mM phosphate buffer (Sigma-Aldrich), and 6 mM sodium azide (Sigma-Aldrich). Glass microscope slides (Fisher) were cleaned and rendered hydrophobic according to protocols in previous publications from this group. Briefly, glass slides were cleaned in acetone, 100 mM KOH, and DI water, and rendered hydrophobic by spin coating polystyrene. Silica colloids of nominal 2.2 μm diameter (Bangs Laboratories) were rendered hydrophobic by coating with 1-octadecanol (Sigma-Aldrich).

Macromolecule Adsorption. 1 mg/mL of filtered BSM was added to a hydrophobic slide in a vacuum grease-sealed O-ring under a coverslip for over 3 hours, after which excess mucin was washed with 150 mM NaCl 2x. 1000 ppm of all the triblocks

were added to 3 μL of hydrophobically modified 2 μm glass particles. The polymer-particle dispersion was exchanged into 150 mM NaCl after 4 hours of adsorption. 1 μL of each of the polymer-particle dispersion was added to the mucin on the slide and left to equilibrate in 150 mM NaCl for two hours. For experiments where we aim to change the structure of the adsorbed mucin layer, we prepared the following solutions: 30 mM DTT (x molar excess), 150 mM NaCl at pH 2 by adjusting the starting solution with pH 1 hydrochloric acid until the solution pH stabilized at pH 2, and 100 mM CaCl2/150 mM NaCl. For these conditions, after physisorbing mucin for 3 hours on the PS slide, we exchanged the mucin into 150 mM NaCl 1-2x to remove excess mucin, then 30 uL of the final solution condition was washed into the O-ring and left to equilibrate for 1-2 hours prior to measurement. For adsorbing cationic PAH to bare silica particle, we employed the adsorption method from Swavola et al to form positively charged silica particles.[38]

***Total Internal Reflection Microscopy*:** Ensemble TIRM was used to measure interactions between polymer coated colloids and slide as described in previous work. In summary, an evanescent wave is generated via reflection of a 633 nm HeNe laser (Melles Griot) onto a prism at 68 degrees. Images are captured using a 40× objective (LD Plan-NEOFLUAR), using a 12−bit CCD Camera (Hamamatsu Orca-ER) at 4 binning, 4 ms exposure, and a frame rate of 28 frames per second. In the TIRM experiment, scattering intensity, I, of a spherical colloidal particle in an evanescent wave is used to determine relative particle-wall separation, h and are related as: $I(h) = I_o \exp(-\beta h)$ where I is the scattered intensity, I_0 is the intensity at particle−wall contact, h = 0, and β^{-1} is the evanescent wave decay length.[248] measurements of scattering intensity from individual levitated particles can be used to record their height variations due to Brownian excursions

perpendicular to the wall. The probability of sampling each height above the surface is related to the potential energy of each height by Boltzmann's equation and can be inverted to obtain the potential energy relative to a reference state (most probable). Measurements of single particle potentials are averaged to obtain ensemble average potentials which are defined as $U(h)-U(h_{mp})/k_BT=\ln\left[n(h_{mp})/n(h)\right]$.[65] Gaussian kernels with a finite width are applied to theoretical potentials to convolute theory to match experimentally measured potential energy profiles to account for finite noise from thermal fluctuations and layer heterogeneity.[42]

5.3.2 Analysis

The net potential energy for PEG-stabilized colloids and substrates, u_N, in the presence of proteins added to the bulk solution may be given by a superposition of potentials due to van der Waals attraction, u_V, steric repulsion, u_S, and gravity, u_G, and depletion attraction, u_D, as,

$$u_{\text{net}}(h)=\overbrace{(4/3)\pi a^3(\rho_p-\rho_f)gh}^{u_G}-\overbrace{A_H a h^{-2}}^{u_V}+\overbrace{\Gamma\exp\left[-\frac{\gamma}{\delta_1+\delta_2}h\right]}^{u_S}$$

where h is particle-wall separation. Subscripts refer to interactions as: (V) van der Waals, (G) gravitational, and (S) steric. The gravitational potential energy of each particle depends on its elevation above the underlying surface multiplied by its buoyant weight, where ρ_p and ρ_f are the particle and fluid densities defined as 1.960 g/cm^3 and 1 g/cm^3, respectively. The particle diameter is typically 2.15 um, but some variations were found due to solution refractive index variations which affect the decay length of the evanescent wave, although

this is beyond the scope of this work. van der Waals attraction for sphere-plate are predicted from the rigorous Lifshitz theory where $A(l)$ includes retardation and screening for the silica colloids and glass substrates used in this work, but can be modeled by a simple power law, as described in previous work where AH is 2410 $a^{-1}kT$ nm^p where p is -2.195.[149]

Steric repulsion due to compression of excluded volume macromolecular brushes are modeled using a soft exponential decay that fits the Milner brush theory until 50% compression of the brush.[263] In our model, the pre-factor, Γ, is fixed at 1984 kT and δ_1 and δ_2 are the thicknesses of the asymmetric layers on the particle and wall. δ_1 was calculated from symmetric TIRM measurements for each copolymer in 150 mM NaCl. For F108, δ_1 is 17 nm, F68 has a δ_1 of 16 nm, PMPC78 and PMAPS113 have a δ_1 of 25 nm, PMPC33 has a δ_1 of 16 nm, and PMAPS31 has a δ_1 of 14 nm (data not shown). The thickness of the mucus layer was determined from the ratio of the most probably intensities described above, compared to a bare silica particle over a bare glass wall. The thickness of the mucin layer in 150 mM NaCl, δ_2, was determined to be 250 nm. γ is a dimensionless constant defined as 9.72, i.e., the value at which the symmetric polymer experiment matches the asymmetric case, which then can be generalized $u_s(h)$ to adsorbed macromolecular architectures with different decaying density profiles at their periphery.[38]

5.4 Results & Discussion

5.4.1 Particles with Inadequate Steric Stabilization Adhere to Mucus

TIRM is first used to resolve net attractive interactions between colloids that lack steric stabilizing layers and mucin. In this work, we illustrate polymer-coated colloids

interactions with adsorbed mucin layers using three dimensional trajectories and kT-scale interactions potentials. Figure 5-2 illustrates *x,y* trajectories of bare and polycation-coated 2.15μm silica microparticles. In Figure 5-2A, we note that two out of eight bare silica particles in the ensemble are freely levitating. This is an example of a surface heterogeneity that is not representative of the equilibrium repulsive interactions observed in the remaining particles in the ensemble, and such particles/artifacts are eliminated from further analysis. The binding lifetime timescale shows that almost all particles in Figure 1 are bound between 100-1000 seconds normal to the mucin layer and the determination of the binding lifetime scale is explained in previous work.[264] Figure 5-1B and Figure 5-1E show the z-component of the particle trajectories on the nanometer-scale for both bare and polycation-coated silica microparticles inferred from the intensity of the particle at each time point in the evanescent wave.[105] Both particles are stuck near the surface of the mucin layer on the wall diffusing only ~50 nm, which indicates the 2.15 um particles are stuck to the thick mucus layer. Figure 5-1C-F are the kT-scale interaction potentials as a result inverting the Boltzmann distribution of heights from the z-trajectories as explained in the Methods section in further detail. Bare silica microparticles are stuck to mucus due to strong (>5 kT) van der Waals attractive interactions between the surfaces at close contact. The PAH-coated silica, which are positively charged, are stuck to the anionic mucin layer either solely due to strong electrostatic attraction between the oppositely charged surfaces or due to some entanglement of oppositely charged polymers. In conclusion, bare and cationic silica particles are examples of mucoadhesive systems with strong attractive interactions with mucus and emphasizes the need for sterically stabilized particles that do not adhere strongly to the mucin network.

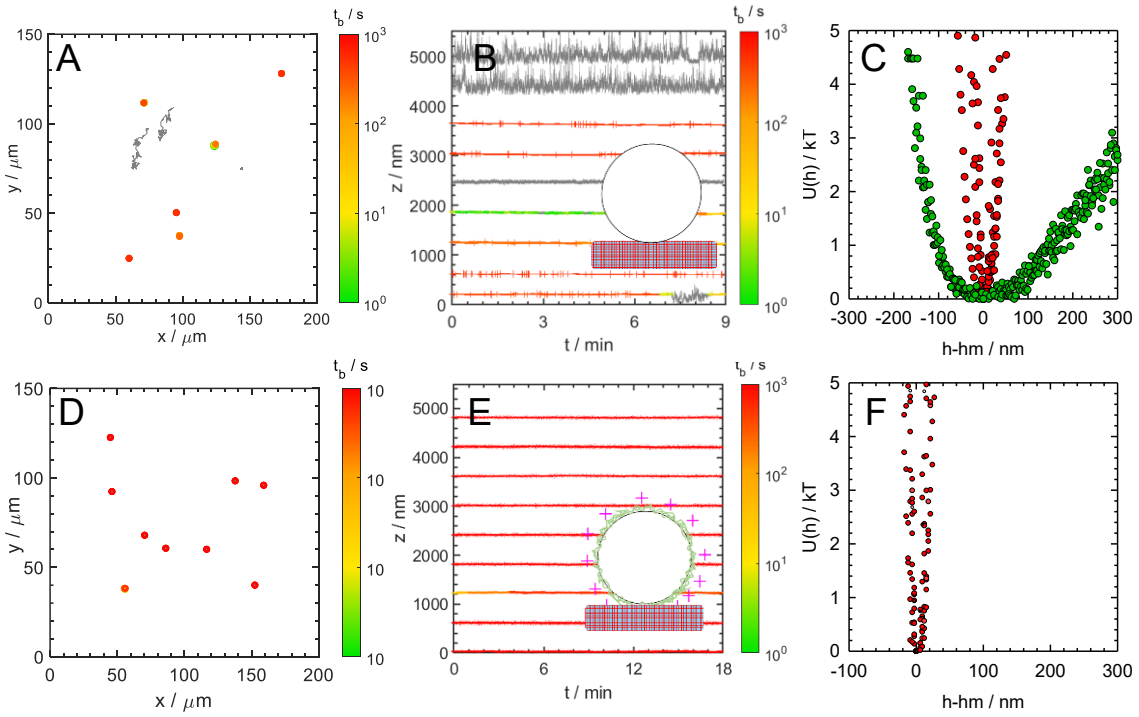

Figure 5-2 **Three dimensional trajectories and equilibrium interactions of mucoadhesive particles with adsorbed mucins.** (A, D) x,y trajectories from video microscopy of bare silica microparticles (A) and silica particles with adsorbed polycationic polymers (PAH) (D) exhibit hindered diffusion near an adsorbed layer of mucin in 150 mM NaCl and pH 6. Scale bar of the normal binding lifetime indicates ~1000s binding of each particle in each position normal to the surface. (B, E) Equilibrium z-trajectories of particles, either bare (B), or coated with PAH (E) show hindered diffusion normal to adsorbed mucins on the wall with particles moving <50 nm above the mucin wall, indicating particles are stuck to the mucin layer. (C, F) Boltzmann inversion of histograms of the *normal* trajectories results in individual particle-wall potential energy profiles on the kT-scale with nanometer-resolution. Potential profiles for both bare (C) and PAH-coated (F) particles exhibit narrow distributions and deep attractive wells characteristic of particles that are stuck to the wall due to net attractive interactions.

5.4.2 3D trajectories and interaction potentials of adsorbed F108-tb with mucin

To directly and sensitively evaluate equilibrium polymer/mucin interactions at the kT-scale, high and low molecular weight (Mw) PEG, PMPC, and PMAPS triblock copolymers were physiosorbed to 2.15 µm hydrophobically modified silica microparticles and suspended over adsorbed mucin in various physiochemical conditions. Figure 5-3A-D reports the three-dimensional trajectories and interaction potential energy profiles of F108-

tb adsorbed on a silica microparticle on a layer of mucin adsorbed to the wall in various solution conditions. The solution conditions: pH 2, 0.1M $CaCl_2$, and 30 mM DTT only affect the layer dimensions and architectures of the mucin layer. PEG copolymers are insensitive to pH, the concentration of $CaCl_2$ used in this study, and have no reducible moieties; therefore, these conditions are not expected to affect PEG-PEG symmetric interactions. Therefore, mucin-mucin and mucin-solvent interactions mediated by these additives affect asymmetric interactions between PEG and mucin. In Figure 5-3, all particles in the ensemble diffuse freely in both the lateral and normal directions with some particles exhibiting ~1s normal binding. Analysis of the ensemble averaged interaction potentials for each copolymer in 150 mM NaCl and plot the gravity-subtracted potentials. From this analysis, the location of the most probably height (thickness of the compressed layers at contact) is ~240 nm, with long range steric repulsion and virtually screened van der Waals (<0.5 kT) confirming the equilibrium 3D trajectories by use of our statistical mechanics analysis of height distributions. Thus, the equilibrium asymmetric interaction between F108-tb and mucin is unequivocally dominated by long-range steric repulsion.

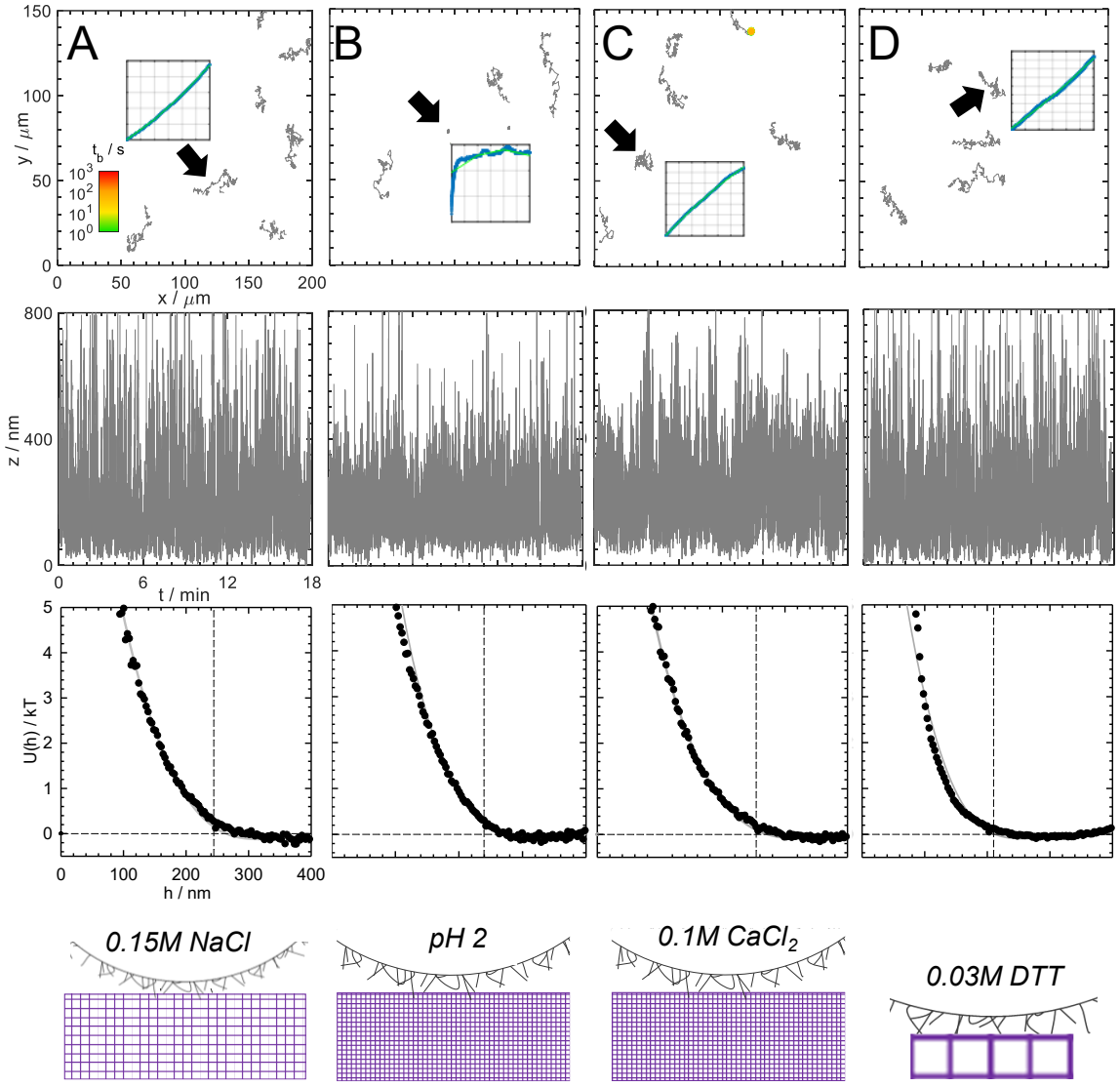

Figure 5-3 **3D trajectories and Ensemble TIRM measurements of particle–wall potential energy profiles, U(h), for particles adsorbed layers of F108-tb over a mucus layer.** Particle-wall schematics illustrates mucin network structure of and thickness in each solution condition based on data. Top row: 2D trajectories of F108tb-coated colloids above mucin in 150 mM NaCl, pH 2, 0.1M $CaCl_2$, and 0.03M DTT, respectively. Insets show mean squared displacement data and fits for the representative particle (see Methods). Middle row: equilibrium nanometer-scale z-trajectories of one particle over 18 minutes. Bottom row: Ensemble-averaged Boltzmann inversion of the height distributions of all particles. Gravity is subtracted to show clearly the steric and van der Waals contributions to the interaction potential (horizontal dashed line is *0 kT*, and vertical dashed line is h_m). The thickness of mucin is 250 nm except for 0.03M DTT, where mucin is 200 nm thick. F108-tb's layer thickness was constant at 17 nm at all conditions. Vertical dashed line represented the compressed thickness of both asymmetric layers (polymer-mucin) and is calculated to be from left to right as: 244 nm, 240 nm, 253 nm, and 210 nm, respectively.

Figure 5-3 also reports the 3D trajectories and interaction potentials of F108-tb interacting with adsorbed mucin in 150 mM NaCl at pH 2. This pH was chosen to mimic the pH of the gastrointestinal mucus milieu, in addition to reports on changes in the rheological properties and decreased porosity of mucins at low pH. The state-of-the-art understanding is that lowering pH decreases repulsion between weak acid groups which increases crosslinking density (schematic at the bottom of Figure 5-3) such as in the calcium case. The pKa of mucus is 3, therefore we expect the overall charge of mucin to change due to protonation of the weak sialic acid groups.[265-266] What is fascinating is that particles in the ensemble still do not bind to mucus in the lateral and normal direction shown by the equilibrium *x, y*, and *z*-trajectories even with such dramatic structural changes in mucus as suggested previously. MSD curve for the representative particle shows that the particle is more tightly bound laterally (bridging attraction skews the MSD curve), but no evidence of net attractive interactions is present between the particle and all, and remaining particles diffuse freely and experience no external force. Furthermore, the location of the most probable height seems to be within the margin of error in our sensitive experiments, compared to the native thickness of adsorbed mucin. The approach used shows that the steric repulsion between the adsorbed F108-tb and mucin is accurately captured by the reported analytical curves.

Calcium is an important cation to consider for mucus architecture, since it is reported 10 mM of this salt was enough to increase the viscosity of mucus, and calcium is present in goblet cells at ~2 mM to pack mucins more tightly via a specific ion effect mediated interaction.[214, 254, 267] Additionally, phase behavior of PEG in 100 mM $CaCl_2$ solutions shows that PEG is stable and only phase separates when the temperature is

increased to 90 degrees Celsius.[268-270] In this work, we modulate the salt solution to have a final concentration of 150 mM NaCl, and titrate in CaCl2 to reach a final concentration of 100 mM after mucin has adsorbed. Surprisingly, we find that in Figure 5-3, particles in the ensemble, again, do not bind to mucus in the lateral and normal direction as shown by the equilibrium *x, y*, and *z*-trajectories. Additionally, the lower panels with interactions potentials show that the location of the most probable height for all polymers was 10 nm higher than in the 150 mM NaCl case, but we speculate that this is due to thermal fluctuations and experimental noise, therefore the thickness of mucin has not changed significantly, and the functional form of the net potential is identical to the case with no calcium chloride.

The last case involves adsorbed mucin with added mucolytic or reducing agent, Dithiothreitol (DTT), which is routinely used for liquefying sputum by reducing disulfide bonds at concentrations below 20 mM.[271-272] Figure 5-3 illustrates that the mucin layer thickness decreases, and the location of the most probably heights decreased ~30 nm to 210 nm. This also reflects in the increased steepness of the steric repulsion component of the net potentials in Figure 3D. which reflects shorter range repulsion compared to the rest of the cases with 150 mM NaCl, 100 mM $CaCl_2$, and pH 2. However, we find that none of the particles are stuck to the surface and there is no evidence of intermittent binding either in the lateral or normal directions. All the particles diffuse freely laterally and perpendicularly even if we expect most disulfide bonds to be reduced and the layer considerably thinner.

Using the same experimental setup and theoretical analysis, shorter repeat units of F108-tb, i.e., F68-tb, exhibited the same trends in the 3D equilibrium random walk trajectories and kT-scale interaction potential profiles: no normal or lateral binding, long range repulsive interactions, and shorter-range repulsion with 30 mM DTT (Figure 5-6). This is a contrasting result to previous reports on molecular weight effects.[239] Our diffusing colloidal probe technique, which is a natural gauge for thermal motion, conforms that thinner copolymer layers on microparticles impart enough steric stability and do not show and nonspecific binding to adsorbed mucin.

Synthetic macromolecules with zwitterionic moieties have become increasingly attractive options for drug delivery across the mucosal barrier.[9, 249, 273] As mentioned previously zwitterionic micelles have recently been shown to diffuse through mucus an order of magnitude faster than PEG coated particles. Moreover, phosphatidylcholine-based zwitterionic polymer coatings on nanoparticles have been shown to have greater mobility in mucus compared to PEG.[274] Therefore, the subsequent figures report direct, sensitive, equilibrium behavior of PMPC and PMAPS-coated microparticles. These two copolymers have been shown to have unique behavior in response to the type and concentration of salts, reflecting their dynamic behavior in aqueous environments. Previous work by the author found that PMAPS and PMPC are highly extended, relatively stiff, copolymers when physiosorbed to hydrophobic surfaces in 150 mM NaCl reflecting the importance of dipole orientation and polymer-solvent interactions on their layer architectures. Previous work by Petroff et al showed that adsorbed PMPC and PMAPS copolymers have a pKa of ~1.5, and therefore remain net neutral at pH > 1.5.[42] Moreover, control experiments on PMPC and PMAPS show that 100 mM $CaCl_2$ does not affect the layer thickness of each of these

copolymers (data not shown). Additionally, like PEG copolymers, both zwitterionic copolymer species are not likely to be affected by reducing agents such as DTT. Like F108-tb, the only effect we would expect would be on the mucus layer thickness and architecture.

Figure 5-4 reports 3D trajectories and kT-scale interaction potentials of PMPC78-tb coated silica microparticles above an adsorbed mucin layer. Freely diffusing particles are seen across the ensemble in all directions, lateral and normal to the surface, over 18 minutes, and the bottom panel reflects a similar result to F108-tb coated particles in that the net interaction potential is dominated by long-range steric repulsion and less than 0.5 kT van der Waals attraction consistent with F108-tb results and indicative of robust steric stabilization. When the pH is lowered to 2 and 100 mM $CaCl_2$ is added, there is still no effect on the binding lifetime in the lateral and normal directions for all particles at equilibrium, and the net potential looks identical with the same functional form and almost identical position of the most probable height (vertical dashed line). We observe two stuck particles in this experiment, and these stuck particles could be due to thinner mucus layers in certain regions which may have caused some particles to stick to the surface at those locations. Similarly, we find no change in any of the interactions of lower Mw PMPC, PMPC31-tb, against mucin in any of the solution conditions we tested (Figure 5-7). Therefore, DTT reduces the mucus thickness to ~210 nm and the steepness of the repulsion regime indicates that the mucin layer is thinner and stiffer; however, no equilibrium attractive interactions are resolved at the kT-scale.

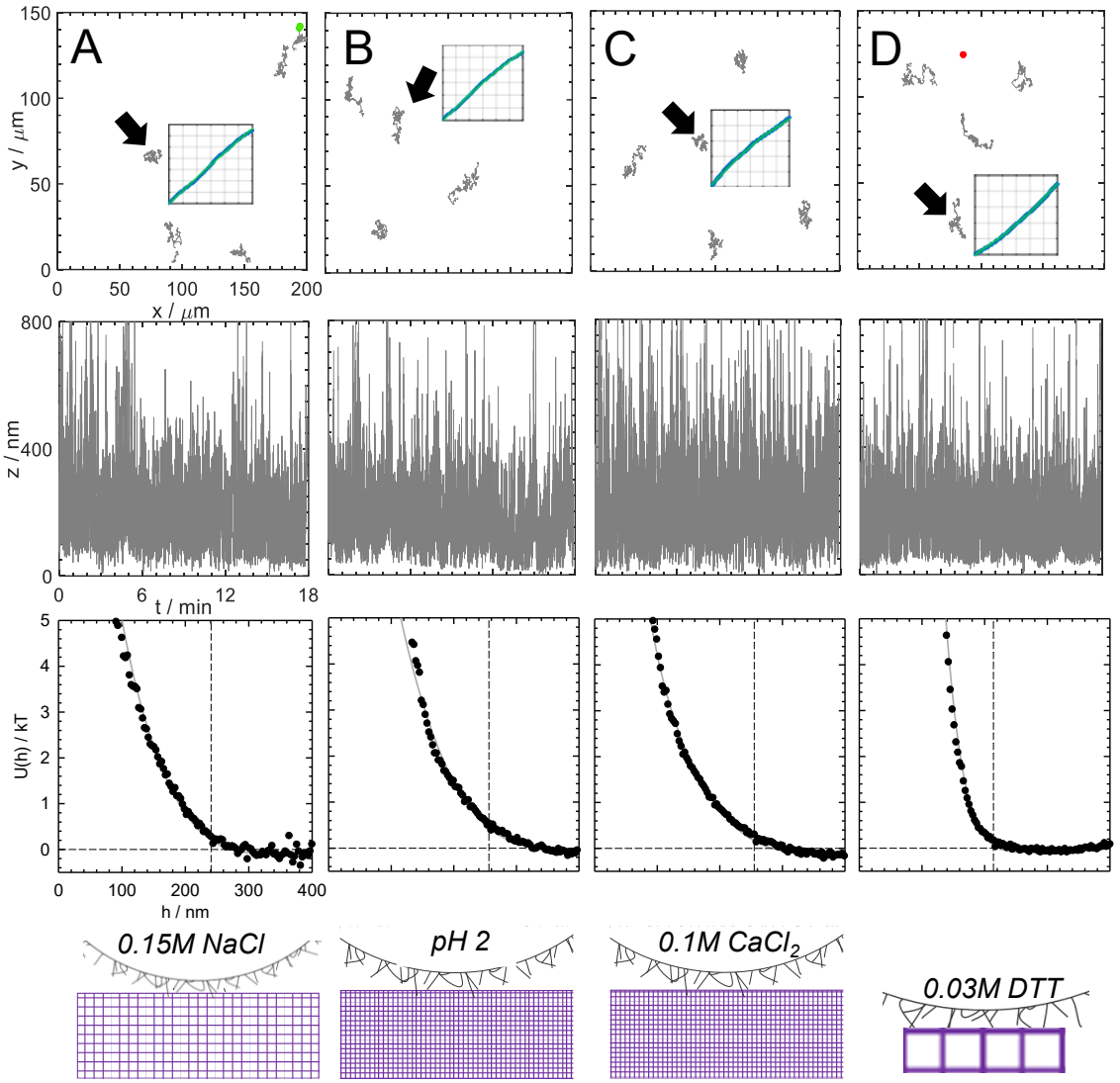

Figure 5-4 **3D trajectories and Ensemble TIRM measurements of particle–wall potential energy profiles, U(h), for particles adsorbed layers of PMPC78-tb over a mucus layer.** Particle-wall schematics illustrates mucin network structure of and thickness in each solution condition based on data. Top row: 2D trajectories of PMPC78tb-coated colloids above mucin in 150 mM NaCl, pH 2, 0.1M $CaCl_2$, and 0.03M DTT. Insets show mean squared displacement data and fits for the representative particle (see Methods). Middle row: equilibrium normal nanometer-scale trajectories of one particle over 18 minutes. Bottom row: Ensemble-averaged Boltzmann inversion of the height distributions of all particles. Gravity is subtracted to show the steric and van der Waals contributions to the interaction (horizontal dashed line is *0 kT*, and vertical dashed line is h_m). The thickness of mucin is 250 nm calculated, except for 0.03M DTT, where mucin was ~214 nm thick, and PMPC78-tb's layer thickness was constant at 25 nm. Vertical dashed line represented the compressed thickness of both asymmetric layers (polymer-mucin) and is calculated to be from left to right as: 240 nm, 255 nm, 256 nm, and 210 nm, respectively.

PMAPS has a reversed dipole orientation compared to PMPC, and a more dynamic response to changes in ionic strength, therefore, it is of interest to evaluate the behavior of

PMPAS coated colloids against mucin in various solution conditions. However, the diffusion and interaction profiles of PMPAS113-tb coated colloids above mucin were identical to F108-tb and PMPC-tb coated colloids in all conditions. Figure 5-5 shows that the particles in the ensemble do not bind to mucus in the lateral and normal direction as shown by the equilibrium *x, y*, and *z*-trajectories, with the location of the most probable height at 243 nm for a 25 nm thick PMPAS113-tb layer and a 250 nm thick mucus layer at 150 mM NaCl. Figure 5-5 B-C shows the consistent trends in pH 2 and 100 mM $CaCl_2$ indicating that there were no effects on the architecture of PMAPS and its layer thickness in calcium chloride solutions. We recognize that there are a few stuck particles in Figure 5C, but, as mentioned previously, these stuck particles may rise from some surface defect at those locations due to thinner layers. Figure 5-5 D shows that DTT reduces the adsorbed mucin thickness to ~150 nm and the steepness of the repulsion regime indicates that the mucin layer is thinner and stiffer. Likewise, we find no change in any of the interactions of lower Mw PMPC, PMPC31-tb, against mucin in any of the solution conditions we tested. However, there were a few particles using PMAPS31-tb that had more van der Waal's attraction between the surfaces at 30 mM DTT (Figure 5-8), which confirmed the layer thickness of mucin, but normal trajectories show no evidence of intermittent binding even at these heterogenous locations, which indicates the net interactions between both high and low Mw PMAPS copolymers and mucin is repulsive, like PMPC and F108.

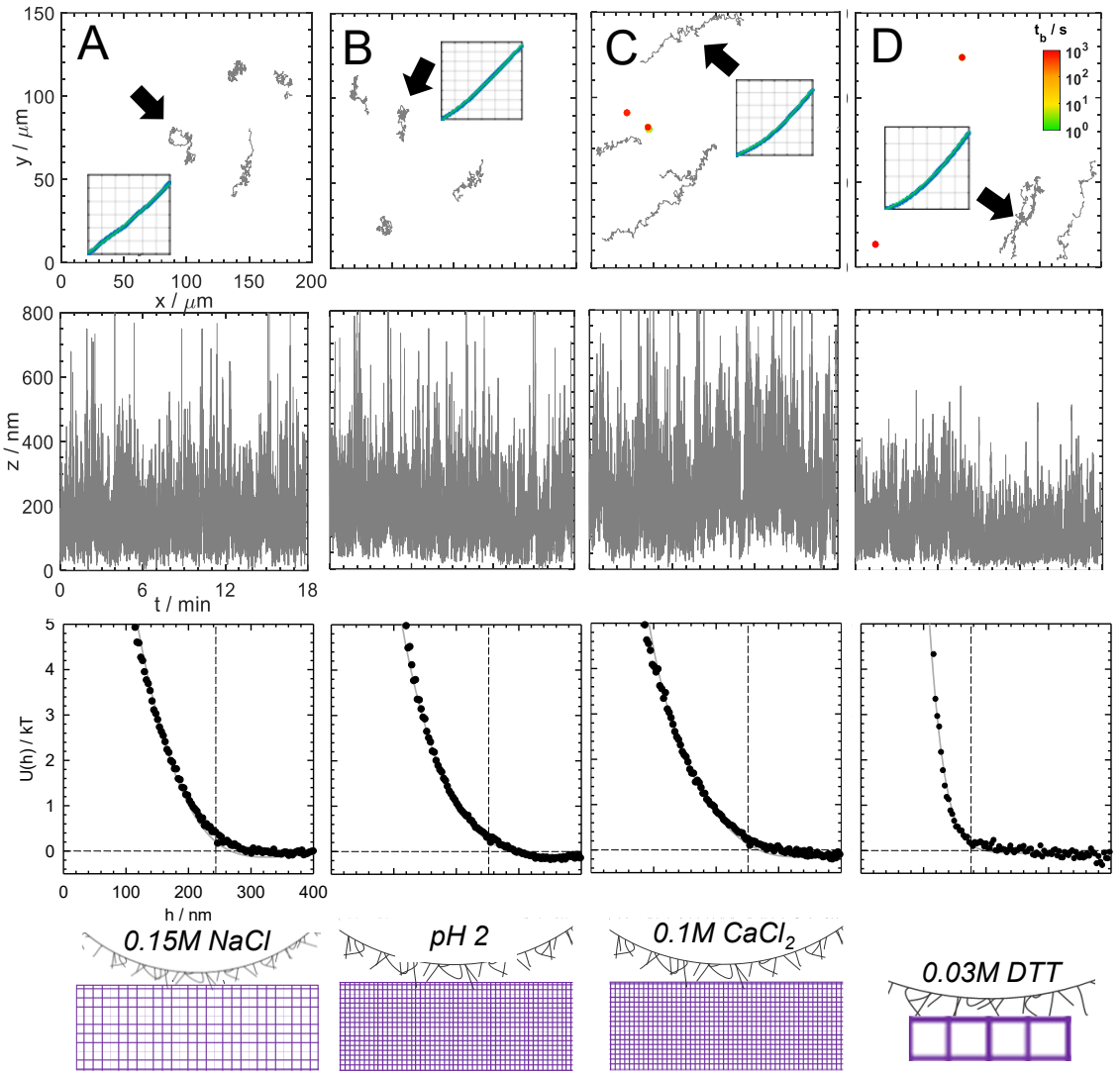

Figure 5-5 **3D trajectories and Ensemble TIRM measurements of particle–wall potential energy profiles, U(h), for particles adsorbed layers of PMAPS113-tb over a mucus layer.** Particle-wall schematics illustrates mucin network structure of and thickness in each solution condition based on data. Top row: 2D trajectories of PMAPS113tb-coated colloids above mucin in 150 mM NaCl, pH 2, 0.1M $CaCl_2$, and 0.03M DTT. Insets show mean squared displacement data and fits for the representative particle (see Methods) Middle row: equilibrium normal nanometer-scale trajectories of one particle (indicated with an arrow) over 18 minutes. Bottom row: Ensemble-averaged Boltzmann inversion of the height distributions of all particles. Gravity is subtracted to show the steric and van der Waals contributions to the interaction (horizontal dashed line is *0 kT*, and vertical dashed line is h_m). The thickness of mucin is 250 nm calculated, except for 0.03M DTT, where mucin was ~214 nm thick, and PMAPS113-tb's layer thickness was constant at 25 nm. Vertical dashed line represented the compressed thickness of both asymmetric layers (polymer-mucin) and is calculated to be from A-D as 243 nm, 251 nm, 250 nm, and 175 nm, respectively.

5.5 Discussion

Understanding particle partitioning from the bulk solution into and subsequent diffusion within porous networks requires a careful understanding of weak interactions. Total Internal Reflection Microscopy offers substantial advantages compared to state of the art experimental techniques attempting to answer questions on polymer/mucin interactions. TIRM capitalizes on the properties of the evanescent wave produced by total internal reflection at the glass/liquid interface.[260] The intensity of the scattered light decays exponentially with the distance separating the sphere and the plate. This provides a sensitive, instantaneous, and nonintrusive measure of the submicroscopic separation distance where changes in distance as small as 1 nm can be detected. From the equilibrium distribution of separation distances sampled by Brownian motion by use of Boltzmann's equation, which defines the mean potential in statistical mechanics, we determine the potential energy profile where forces as small as 0.01 pN can be detected.

This is in stark contrast to sensitive force measurement techniques SFA and AFM. Although SFA benefits from measuring sub-nanometer separations using multiple beam interferometry, it employs 1 cm interacting cylinders which are several orders of magnitude larger than colloidal particles (even though we can employ the Derjaguin approximation). AFM was used as a colloidal probe technique back in 1992 by Ducker who attached a micron sized colloid to the tip of an AFM probe and measured the forces between it and a flat surface. Both SFA and AFM utilize fixed bodies interacting at a controllable distance and are limited by being mechanical properties of force.[31]

However, TIRM utilizes thermal energy as a gauge for interactions which is more relevant for colloids that do free Brownian diffusion above or in surfaces and measures forces at least five orders of magnitude weaker than its force measurement counterparts.[248, 260] Moreover, TIRM is sensitive to surface heterogeneities which can be seen in Figure 4-5 where some particles are stuck to the surface but have been eliminated from the ensemble analysis because they are attributed to surface defects on the heterogenous mucus layer. Therefore, we can accurately examine surface defects and discern 'real' interactions from defect-induced attraction.

From our results in Figures 3-5, we can infer important information on polymer/mucin asymmetric interactions in various solution conditions. For F108-tb, PMPC78-tb, and PMAPS113-tb adsorbed on particles interacting with adsorbed mucin on the wall in 150 mM NaCl (physiological conditions), we see no evidence of attractive, kT-scale interactions between any of these polymer systems and mucin. Figure 2 provides a benchmark for true mucoadhesive interactions at the kT-scale, and both lateral and normal diffusion trajectories in Figures 3-5 unequivocally show net repulsive interactions between PEG and both zwitterionic copolymers and mucin. Potential energy profiles corroborate evidence from the three-dimensional trajectories by showing highly extended steric layer thickness where mucus is 250 nm. Therefore, the net asymmetric interaction is repulsive, and we can infer that since no collapse has occurred on the colloid or wall, individual symmetric interactions, i.e., polymer-polymer, and mucin-mucin are repulsive and favor their solvated states. These results, specifically for F108-tb and generally PEG-

copolymers, contrasts with results that show that PEG-mucin interactions are weakly attractive, and that molecular weight influences mucoadhesive properties of PEG.

From our analysis for all three polymers, we found that while the mucin layer thickness decreased about 40-50 nm from its solvated thickness in 150 mM NaCl, we still observe no attractive interactions, even intermittent binding in both lateral and normal trajectories. This implies that DTT decreased the solvated thickness of mucins and formed stiffer shorter brushes, consistent with macroscopic properties of reduced mucin, but equilibrium trajectories and potential profiles still exhibit net repulsive interactions. Variations in pH and presence of calcium salts are known to mediate the crosslinking density of mucins.[214, 218, 275-278]

Low pH is known to protonate weak sialic acid groups, which reduces repulsion between those negatively charged groups, whereas calcium mediates mucin crosslinking via the known Hofmeister effect where calcium chelates negatively charged carboxylate groups and thus competes with surrounding water molecules changing the overall solvation of mucins and increasing attractive interactions. Through both methods, low pH, and presence of at least 10 mM calcium have been shown to induce gelation in solvated mucins characterized by an increase in viscosity and other viscoelastic properties. Interestingly, this did not lead to a significant change in the functional form and range of repulsion compared to the system in 150 mM NaCl. As illustrated in Figures 3-5, we still see no significant change in lateral and normal diffusion profiles and the equilibrium potential energy profiles consistently show thick solvated layers with net repulsive asymmetric

interactions. These results closely resemble SFA results of adsorbed PEG interacting with mucin at pH 2 which sows no change in the range of forces compared to neutral pH conditions.[206]

Insets in the top row from Figures 3-5 that show mean squared displacement of the representative particle show that most particles freely diffuse in *x,y* except for the condition of pH 2 (Figure 3B), where it seems that the particle is more tightly bound laterally. While typically this indicates a bridging attraction between the particle and wall, no attractive interactions were resolved in the original potential energy profiles before gravity subtraction. Previous work by the corresponding author has shown that lubrication near the surface of the mucus layer may change in different solution conditions, which could possibly explain certain cases where particles may be bound. Other particles shown in Figure 5-5 experience migration due to the sample being unlevel. Each MSD curve is fit to a parabolic function $4Dt + (vt)^2$ that supports the fact that these particles are freely diffusing but experience drift to an unlevel sample and not mucus-polymer interactions.[279-280]

It is important to highlight the asymmetry we measure using TIRM. We posit that there higher crosslinking density inside the mucin layer due to lower pH and excess calcium may induce more mucin-mucin attractive interactions based on precedent. Changes in pH and introduction specific ion effects have been shown by the authors to mediate symmetric polymer layer architecture and interactions; however, at pH 2 (higher than the pKa of both zwitterionic copolymers) and 100 mM $CaCl_2$, we expect no change in the layer thickness and architecture of PEG, PMAPS, or PMPC copolymers. This is further evidenced by the lack of particle-particle attractive interactions (aggregation) at these conditions. Therefore, while the solvent conditions impact the internal structure

differently for each component, the net asymmetric interaction between the polymers and mucin is repulsive. Furthermore, while previous reports claim that the polymer molecular weight may impact mucoadhesive or mucopenetrative properties of polymer coated colloids, we unequivocally show that there is no impact of molecular weight on the net interaction. As shown in the supplementary information, Figure S1-3, the net asymmetric interaction is repulsive, except for low Mw PMAPS, which exhibits some heterogeneity.

Ultimately, our work strongly implies that nanoparticles with physiosorbed PEG, PMPC, and PMAPS copolymers form thick, solvated brushes with net repulsive symmetric and asymmetric interactions (with mucus) regardless of the changes in the internal structure of adsorbed mucin, i.e., these physiosorbed copolymers produce robust mucopenetrative particles. We postulate that while our results imply that PEG, PMPC, and PMAPS copolymers on nanoparticles may be able to diffuse through mucus with kT-scale repulsion, tuning the copolymer chemistry is still needed to achieve a thermodynamic driving force to partition from the solvent into the mucus porous network by designing synthetic macromolecules that have specific attractive interactions on the order of ~kT.

5.6 Conclusions and Outlook

Three dimensional random walks, with nanometer resolution, from super resolution microscopy and evanescent wave scattering couple with equilibrium statistical mechanical analysis of polymer-mucin interactions reveal that PEG, PMPC, and PMAPS triblock copolymer coated microparticles exhibit net repulsive interactions with adsorbed mucin, no intermittent binding indicating any bridges or mucoadhesive interactions at the kT-scale. Intensity analysis reveals mucin makes 250 nm thick layers in 150 mM NaCl. Control experiments show that F108, PMPC, and PMAPS architecture and layer thickness

are unperturbed by low pH and 100 mM $CaCl_2$. Addition of excess DTT may have stiffened and decreased the thickness of mucin layers according to the steepness of the repulsion, but the net measured interactions are consistently repulsive regardless of the solvent condition or copolymer molecular weight.

Consistent net repulsive asymmetric interactions between ethylene oxide and zwitterionic synthetic macromolecules and mucin indicate PEG, PMPC, and PMAPS are suitable mucopenetrating coatings for nanoparticles. pH and calcium may impact the structure/layer architecture of adsorbed mucin, i.e., mucin- mucin interactions, but mucin remains extended when adsorbed to hydrophobic surfaces. Ultimately, our interactions provide a strong foundation for reconciling conflicting views on mucoadhesion and mucopenetration, ad provide a template for designing particles with chemically modified coatings of PEG and ZI polymers to employ integrated mucopenetrating and mucoadhesive properties with specific interactions mediated by solvent conditions.

5.7 Supplemental Information

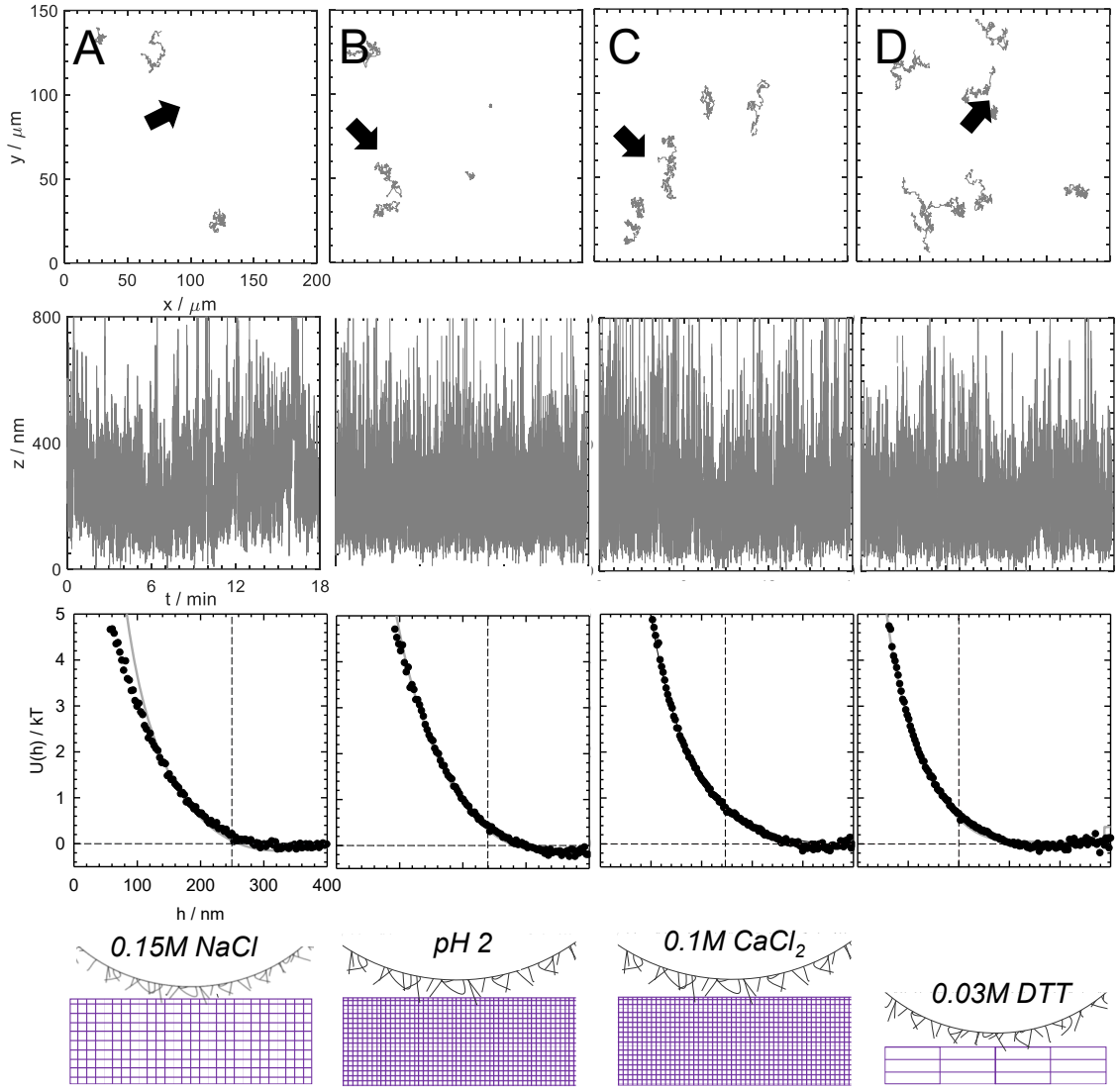

Figure 5-6 **3D trajectories and Ensemble TIRM measurements of particle–wall potential energy profiles, U(h), for particles adsorbed layers of F68-tb over a mucus wall.** Particle-wall schematics illustrates mucin network structure of and thickness in each solution condition. Top row: 2D trajectories of F68tb-coated colloids above mucin in 150 mM NaCl, pH 2, 0.1M $CaCl_2$, and 0.03M DTT. Middle row: equilibrium normal nanometer-scale trajectories of one particle (indicated with an arrow) over 18 minutes. Bottom row: Ensemble-averaged Boltzmann inversion of the height distributions of all particles. Gravity is subtracted to show the steric and van der Waals contributions to the interaction. The thickness of mucin is 250 nm, except for 0.03M DTT, where mucin was 200 nm thick, and F68-tb's layer thickness was constant at 17 nm. Vertical dashed line represented the compressed thickness of both asymmetric layers (polymer-mucin) and is calculated to be from A-D as 249 nm, 240 nm, 246 nm, and 200 nm, respectively.

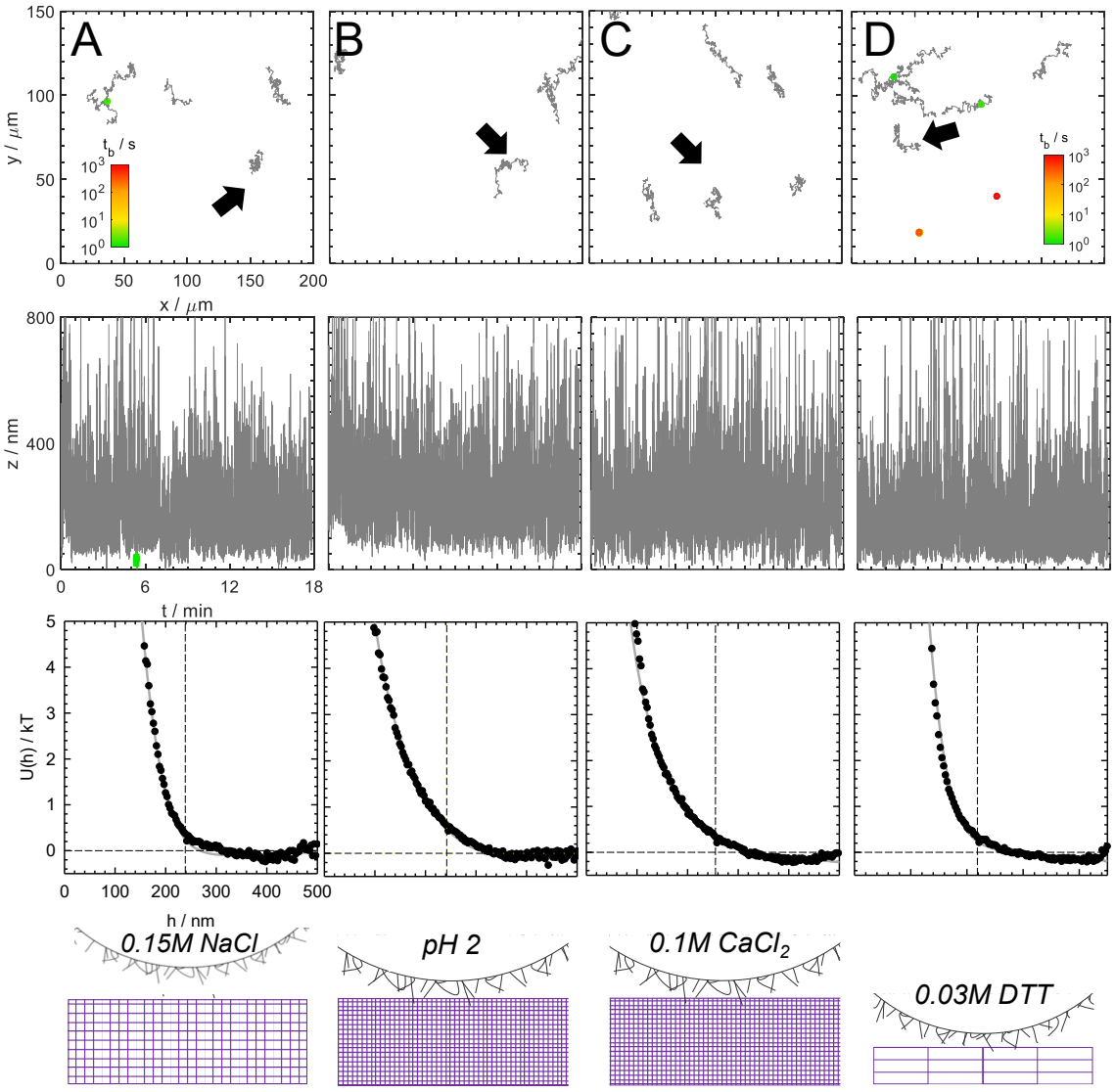

Figure 5-7 **3D trajectories and Ensemble TIRM measurements of particle–wall potential energy profiles, U(h), for particles adsorbed layers of PMPC33-tb over a mucus wall.** Particle-wall schematics illustrates mucin network structure of and thickness in each solution condition. Top row 2D trajectories of PMPC33tb-coated colloids above mucin in 150 mM NaCl, pH 2, 0.1M $CaCl_2$, and 0.03M DTT. Middle row equilibrium normal nanometer-scale trajectories of one particle (indicated with an arrow) over 18 minutes. Bottom row: Ensemble-averaged Boltzmann inversion of the height distributions of all particles shows long-range repulsion between PMPC33-tb and mucin in each condition. Gravity is subtracted to show the steric and van der Waals contributions to the interaction. The thickness of mucin is 250 nm calculated by Eq.1, except for 0.03M DTT, where mucin was 200 nm thick, and PMPC33-tb's layer thickness was constant at 16 nm. Vertical dashed line represented the compressed thickness of both asymmetric layers (polymer-mucin) and is calculated to be from A-D as 239 nm, 242 nm, 255 nm, and 219 nm, respectively.

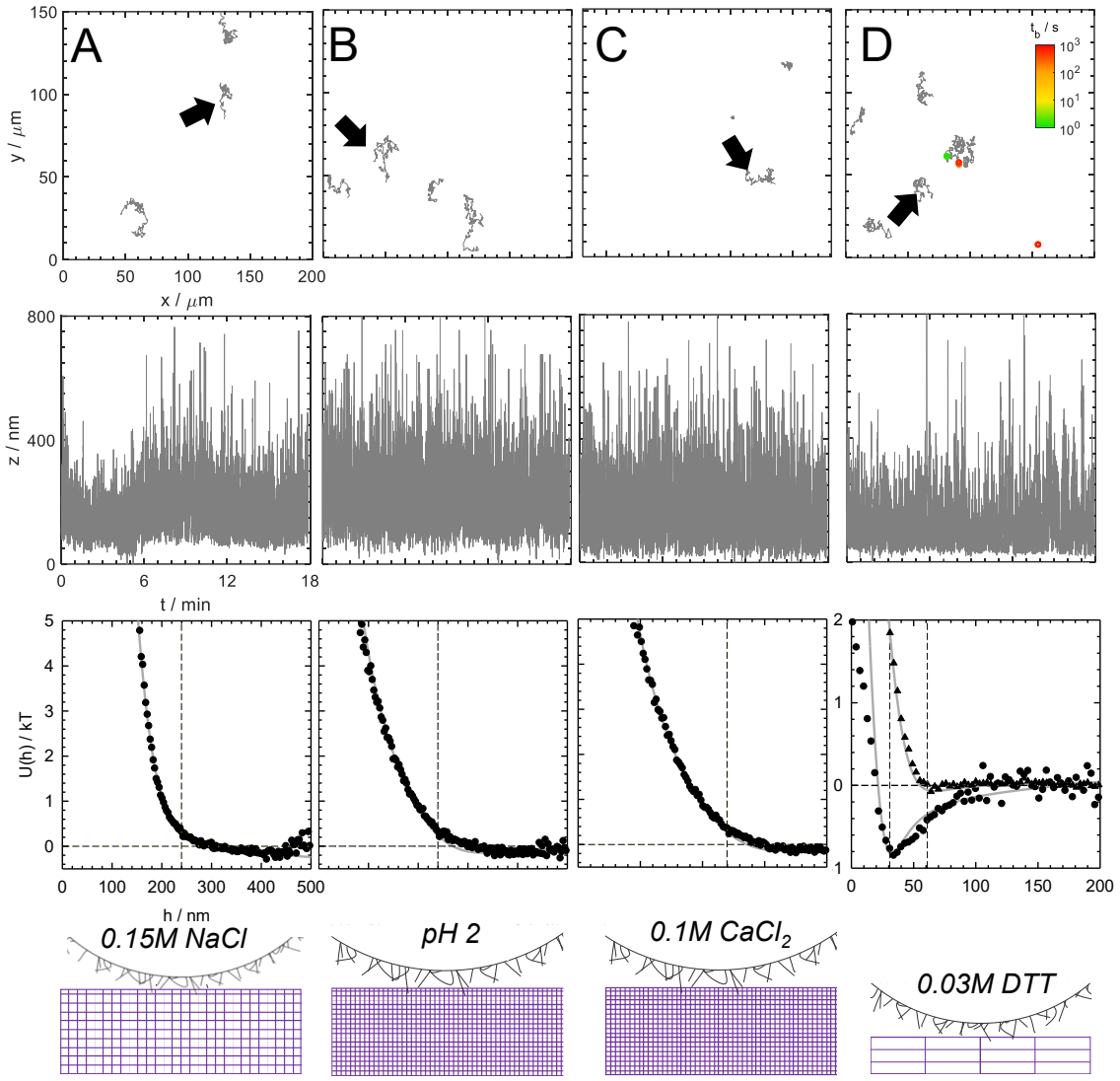

Figure 5-8 **3D trajectories and Ensemble TIRM measurements of particle–wall potential energy profiles, U(h), for particles adsorbed layers of PMAPS31-tb over a mucus wall.** Particle-wall schematics illustrates mucin network structure of and thickness in each solution condition. Top row: 2D trajectories of PMAPS31tb-coated colloids above mucin in 150 mM NaCl, pH 2, 0.1M $CaCl_2$, and 0.03M DTT. Middle row: equilibrium normal nanometer-scale trajectories of one particle (indicated with an arrow) over 18 minutes. Bottom row: Ensemble-averaged Boltzmann inversion of the height distributions of all particles shows long-range repulsion between PMAPS31-tb and mucin but DTT makes thinner mucin layers and exposes vdW attraction between. Gravity is subtracted to show the steric and van der Waals contributions to the interaction. The thickness of mucin is 250 nm calculated by Eq.1, except for 0.03M DTT, where mucin was 20-45 nm thick for two ensemble populations. PMAPS31-tb's layer thickness was constant at 14 nm. Vertical dashed line represented the compressed thickness of both asymmetric layers (polymer-mucin) and is calculated to be from A-D as 240 nm, 240 nm, 240 nm, and 20-45 nm, respectively.

6 ENERGY LANDSCAPES ON POLYMERIZED LIQUID CRYSTAL FILMS

6.1 Abstract

Topological defects of liquid crystals (LC) at aqueous interfaces display optical heterogeneity based on surface anchoring and orientation. Developing a quantitative understanding of colloidal interactions mediated by defects at the LC-aqueous interface may drive a deeper theoretical framework for colloidal self-assembly. By integrating diffusing colloidal probes and video microscopy, we identify features of the particle-wall potential. Experimental results using sterically stabilized diffusing colloids and polymerized LC surfaces reveal that the ensemble particle density is lower near surface point defects compared to near-planar regions of LC, despite the sample being topographically smooth. Iterative and converging Monte Carlo simulations show higher potentials at the defect decreasing to a plateaued minimum near other bulk regions. We determine that van der Waals attraction is significantly weaker at the defect due to changes in refractive and dielectric properties of LC that are controlled by their molecular orientation. Additional adjustments in the particle-wall repulsive potential at the aqueous-LC interface increases agreement between experiment and simulation. We hypothesize that the LC orientation changes the range of steric repulsion, between macromolecular-coated colloids and LC, electrostatic repulsion driven by changes in surface potential, and the position-dependent energy gradient. Ultimately, our findings illustrate how non-invasive, sensitive probes of the underlying energy landscapes of topological defects explain the relationship between orientation and weak interactions, which may become a template for further understanding and predicting colloidal self-assembly on LC.

6.2 Introduction

Spatial structures and time evolutions of topological defects on LC surfaces can be captured by optical techniques.[281-282] Motivated by theoretical characterization groundwork by Modes et al,[283] topological defects were shown to exhibit structural and dynamic heterogeneity[284] and adaptive responses to external stimuli, with applications in biomedical engineering, robotics, and sensors.[285-286] The complexity of LC surfaces has become a tool to mediate self-assembly with a particular rising interest in studying how topological defects affect the assembly process. It is thought that defects at LC-aqueous interfaces affect the nanoscopic environments to direct the formation of well-defined molecular assemblies.[284] Current methods in surveying how topological defects impact self-assembly such as fluorescence microscopy, cryogenic transmission electron microscopy and super-resolution optical microscopy highlight current challenges in measuring nanoscale systems non-invasively, sensitively, and at equilibrium. To take advantage of the dynamic heterogeneity in LC defects, time-averaged interactions of colloids at a LC surface is necessary for successful reversible and tunable self-assembly.

There is a rapid evolution in understanding how the orientation of the LC near topological defects affects these colloidal interactions. The change in orientation of the dipolar topological defects surrounding particles at the LC−aqueous interface emphasizes findings that LCs can mediate long-range interactions of colloidal particles.[287] Moreover, experiments using microparticles deposited at the LC−aqueous interface, by Koenig et al, showed that LC-mediated interactions drive interfacial assemblies of particles via reversible ordering transitions; however, it is necessary to acquire more nuanced measurements compared to deposition experiments to understand energy landscapes on

LC-aqueous interfaces.[288-289] It is thought that the ordering of LCs is dominated by van der Waals forces but the range of interactions is far more complex including electrostatic double layers, hydrogen bonding, and so on,[290-292] therefore a challenge remains in determining what types of interactions govern the energy landscapes over LC interfaces.[293] Moreover, understanding interactions between nanoparticles and LC is difficult since they are below the diffraction limit, and potential mean force measurements for interparticle interactions are much weaker than predicted by simulations.[287] Consequently, the main challenge is to develop an assay that non-invasively measures time-averaged energy landscapes on LC-aqueous interfaces with kT-sensitivity and nanometer resolution, reconcile experimental observations with simulations and, subsequently, predict ordering near LC defects.

In this work, we tackle this challenge by probing energy landscapes using a well-established assay integrating video microscopy of concentrated diffusing colloids[294] over polymerized LCs. In experimental observations of freely diffusing, sterically stabilized colloids over a polymerized LC surface, we measure density differences and how they vary with distance from the defect. Using inverse Monte Carlo simulations based on the experimental results, we present three-dimensional free energy and potential energy landscapes with equilibrium, time-averaged sampling. Our integrated method exploits stochastic thermal motion as a natural gauge of kT-scale energy landscape features to take advantage of stochastic or thermal motion, in addition to accurately determining energy landscapes with well-established theoretical groundwork on van der Waals interactions by considering small-scale roughness, retardation, and screening.[78, 294] Variations in energy between individual particles and the wall are proportional to the effects of patterned

surfaces on either van der Walls interactions or polymer brush thickness with limited adjustable parameters. The reported equilibrium method and results provide a basis for further study on the meso- and nano-scale potentials of colloidal interactions with LC interfaces specifically targeted at using molecular orientation to drive density-based self-assembly.

6.3 Theory

Particle-wall potentials

The net potential energy, u_N, of colloids interacting with a planar substrate is the superposition of potentials due to van der Waals, u_V, sterics, u_S, and gravity, u_G, as Jumai'an et al

$$u_N(h) = u_V(h) + u_S(h) + u_G(h) \qquad (1)$$

where h is the particle−wall separation. The gravitational potential energy is,

$$u_G(h) = \frac{4}{3}\pi a^3 hg\left(\rho_p - \rho_f\right) \qquad (2)$$

where a is the particle radius, ρ_p and ρ_f are particle and fluid densities, and g is acceleration due to gravity. The van der Waals interaction for a sphere and a plate using the Derjaguin approximation is,[81]

$$u_V(h) = \frac{a}{6}\int_h^\infty \frac{A_{LC}(l)}{l^2}\,dl \qquad (3)$$

where $A(l)$ is the Hamaker constant. For the silica colloids and LC substrates in this work, the Hamaker constant can be obtained from Lifshitz theory to include retardation and screening by,[81]

$$A(l) = \frac{1}{2}\left[1 + 2\kappa l\right]\exp\left[-2\kappa l\right]A_{\nu=0} + A_{\nu>0}\left(\frac{1+\left(b_f/a_f\right)l}{1+c_f l + d_f l^2}\right) \tag{4}$$

where κ is the Debye length, and a_f, b_f, c_f, and d_f are constants. $A_{\nu=0}$ and $A_{\nu>0}$ are the zero frequency and dispersion energy contributions which can be calculated for a three material system as,[295]

$$\begin{aligned} A_{\nu=0} &= \frac{3}{4}kT\left(\frac{\varepsilon_1-\varepsilon_3}{\varepsilon_1+\varepsilon_3}\right)\left(\frac{\varepsilon_2-\varepsilon_3}{\varepsilon_2+\varepsilon_3}\right), \\ A_{\nu>0} &= \frac{3h_p\nu_e}{8\sqrt{2}}\frac{\left(n_1^2-n_3^2\right)\left(n_2^2-n_3^2\right)}{\left(n_1^2+n_3^2\right)^{0.5}\left(n_2^2+n_3^2\right)^{0.5}\left[\left(n_1^2+n_3^2\right)^{0.5}+\left(n_2^2+n_3^2\right)^{0.5}\right]} \end{aligned} \tag{5}$$

where ε is the static dielectric constant and n is the refractive index for each material, 1, 2, and 3. Additionally, h_p is the Planck's constant, ν_e is the main dielectric adsorption frequency, k is the Boltzmann constant, and T is temperature.

Steric repulsion between adsorbed macromolecules can be modeled as,[35, 149]

$$u_S\left(h,\Gamma_S\right) = \Gamma_S\exp\left[-\delta\cdot h\right] \tag{6}$$

where δ and Γ_S are constants obtained from previous fits to PEG-PEG interaction potential profiles. The uncompressed polymer brush thickness L_o is,

$$2L_o = \frac{-1}{\delta}\ln\left[\frac{0.1kT}{\Gamma}\right] \tag{7}$$

which defines the thickness of the polymer layers at contact, defined at 0.1 kT, which is the limit of sensitivity of TIRM, as described in previous work.[149]

Particle-particle potentials

The pair-potential energy, $u_{pp,}$ of sterically stabilized colloids interacting is,[150, 295] _ENREF_17

$$u_{pp}(r) = 0.5\Gamma_S \exp\left[-\delta(r-2a)\right] \qquad (8)$$

where r is the center-to-center separation of the particle.

6.4 Experimental Section

Materials

LC films Chemicals were used as received from the manufacturers without additional purification. The nematic LC 4-cyano-4′-pentylbiphenyl (5CB, >99.5%) was obtained from Jiangsu Hecheng Advanced Materials Co., Ltd. (Nanjing, China). Reactive mesogen 1,4-bis[4-(3-acryloxyloxypropyloxy]-2-methylbenzene (RM257, >95%) was obtained from BOC Sciences (Shirley, NY). The photo-initiator, 2-dimethoxy-2-phenylacetophenone (DMPA, >99%), toluene (≥99.5%), dimethyloctadecyl[3-(trimethoxysilyl)propyl] ammonium chloride (DMOAP, 42 wt% in methanol), and glycerol (≥99.5%) were obtained from Sigma-Aldrich (St. Louis, MO). Fisherfinest premium grade glass slides were purchased from Fisher Scientific (Pittsburgh, PA). Copper transmission electron microscope grids (286 μm x 286 μm x 18 μm) were obtained from Electron Microscopy Sciences (Hatfield, PA). Purification of water (18.2 MΩ cm resistivity at 25 °C) was performed using a Milli-Q water system (Millipore, Bedford, MA, USA).

Polymer and Colloidal Probes The commercial PEO_{141}-PPO_{51}-PEO_{141} (F108) copolymer (M_w/M_n=1.2) was donated by BASF. Silica colloids of nominal 2.2 μm diameter (Bangs Laboratories) were rendered hydrophobic by coating with 1-octadecanol

(Sigma-Aldrich), and will be referred to, hereon, as OD silica for brevity.

Methods

Preparation of polymerized LC Films All thin LC films of 5CB were synthesized from mixtures of 5CB, RM257, and DMPA (20 wt% RM257/5CB) placed into the pores of a 75 mesh copper TEM grid supported on a DMOAP coated glass slide to promote homeotropic surface anchoring at the glass-LC surface. The LC mixture was prepared by vortexing 20 mg of RM257, 2 mg of DMPA, 80 μL of 5CB, and 40 μL of toluene (a cosolvent to facilitate mixing) in a glass vial. After the solids were dissolved, the vial was loosely covered with aluminum foil and left open to atmosphere overnight in a fume hood to evaporate off the toluene. Immersion of the supported LC-filled grid under a water-glycerol mixture (50/50 v/v) imparted planar surface anchoring at the LC-aqueous interface. Polymerization of the films was initiated by exposing the sample to long-wave ultraviolet (365 nm, Spectroline ® E-Series Spectronics Corporation, Westbury, NY) for 10 minutes (2.5 mW/m^2 at a distance of 5 cm) at room temperature. Films were rinsed with additional water (20x volume of 50/50 water/glycerol mixture) after polymerization before further analysis.

Polymer Adsorption on LC film 1000 ppm PEOtb was dissolved in DI water and added to vacuum grease-sealed O-rings on the TEM grid with the 5CB LC film and left to equilibrate overnight under a coverslip.

Sedimentation Fractionation of PEGtb-coated OD silica 250 μL of hydrophobically modified 2 μm OD silica were added to 2 mL of 1000 ppm PEOtb in DI water and left on an inverter overnight. Afterwards, the dispersion was sonicated for 2 minutes and placed in a clean glass tube with a cap, where it was left to sediment for 1

hour. Then, an aliquot at a constant height in the tube was taken and placed in a second clean glass tube. The original dispersion was sonicated again, and the volume removed was replaced with an equal volume of 1000 ppm PEOtb in DI water. The original tube was left to sediment again and fractionation at a constant height was repeated twice to achieve a homogenous sample of PEGtb coated particles. 30 μL of these fractionated particles were placed in an O-ring on the TEM grid with the polymerized LC film and left to sediment around the defect of choice for 5 minutes before recording.

Optical Examination of LC Films using Cross Polarization The orientation of LC films was examined with optical microscopy by using plane-polarized light in transmission mode on an Olympus BX41 microscope with two rotating polarizers and a 10.0 MP Moticam camera with 4x, 20x, and 50x objectives.

Optical Examination of LC Films using PolScope A CRI PolScope affixed to a separate Olympus BX41 microscope was used to measure the optical retardance of the LC films. The samples were illuminated with circularly polarized light (λ = 546.5 nm) and collected with a 10.0 MP Moticam camera.

Optical Examination of Colloids on LC Films using Video Microscopy Videos of diffusing colloidal probe tracking of F108-coated silica particles over F108-coated LC films were captured using a 63× objective (LD Plan-NEOFLUAR) and a 12-bit CCD Camera (Hamamatsu Orca-ER) on an upright optical microscope (Axio Imager A1m, Zeiss) [0.75 numerical aperture]. Images were recorded at 16 frames/s for 90 minutes to produce image stacks ~89000 frames. 55x41 μm^2 images were obtained with 608 x 404 resolution to produce 100 nm pixels which allowed for centroid location using typical particle tracking algorithms described below.

Computer Simulations A standard MC algorithm in the canonical (NVT) ensemble replicates experimental conditions listed in Table 1.[296] The number of particles and simulation box size are based on tracked experimental recordings and the simulation is constrained to a two-dimensional plane analogous to gravity in experiments. The steric repulsion in eq. (8) are accurate for sterically stabilized silica particles from precedent literature in both experiments and simulations.[149, 297] Equilibrium distribution functions were obtained using 10^5 steps after an equilibration of 10^6 steps for initialization or 10^5 steps for an iterative simulation.

The inverse Monte Carlo (MC) algorithm employs iterative forward canonical MC simulations with different guesses for $u_i(x,y)$ until the simulated $\rho_i(x,y)$ is in high agreement with the experimental $\rho(x,y)$. The pixel size for each bin allocated to an individual $u_i(x,y)$ value was determined by a 24 x 24 resolution of the experiment or simulation box. To ensure rapid convergence to a unique solution, an algorithm was used to generate updated guesses for $u_{i+1}(x,y)$ after each iteration i by,[294, 296]

$$u_{i+1}(x,y) = u_i(x,y) + 0.5kT\left[\frac{\rho_i(x,y)}{\rho(x,y)} - 1\right] \quad (9)$$

For the initialization of the algorithm, energy is initialized at 0 ($u_{i=0}(x,y) = 0$ for all positions) and particles start evenly spaced on a hexagonal lattice. The starting positions for all iterative simulations are equivalent to the final configuration of the previous run. Iterations continue until the root-mean-square error, χ, averaged over all pixels is minimized using,[294]

$$\chi_i = \sum_x \sum_y \left[\left(\rho_i(x,y) - \rho(x,y)\right)^2\right]^{0.5} \quad (10)$$

Upon convergence, the simulation energy, $u_i(x,y)$, was converted into the simulated particle wall potential, $u_{i,pw}(x,y)$, by,

$$u_{i,pw}(x,y) = u_i(x,y) - u_G(x,y) \qquad (11)$$

Where $u_G(x,y)$ is the gravitational planar tilt energy at every pixel calculated by fitting a 2D plane to the simulation energy. This represents the average tilt of the locally flat LC surface.

Weighted Average Energy

Theoretical energy profiles that depend on particle-wall separation, h, were converted to a weighted average value, $\langle u(h) \rangle$, by,

$$\langle u(h) \rangle = \frac{\sum_{h=0}^{\infty} [u(h) - u_m(h_m)]\, p(h)}{\sum_{h=0}^{\infty} p(h)} + u_m(h_m) \qquad (12)$$

where u_m the most probable energy calculated at the most probably height h_m. Probability distribution $p(h)$ is calculated by the Boltzmann distribution function,[298]

$$p(h) = p(h_m) \exp\left[\frac{u_N(h) - u_m(h_m)}{kT} \right]. \qquad (13)$$

considering net particle-wall potential, u_N, from eq. (1).

LC Interfacial Interaction Models

Three unique methods are used to interpret the vdW and repulsive interactions between the particles and LC substrate from the converged simulation energy.

All models are based on the net particle-wall interaction,

$$u_N(x,y,h) = X_{VDW}(x,y)u_V^{perp}(h) + u_S(h,\Gamma_S(x,y)) + u_G(h) \quad (14)$$

with different applications of the vdW fitting parameter, $X_{vdW(x,y)}$, and repulsive fitting parameter, $\Gamma_{S(x,y)}$. Steric potential, $u_{S(h)}$, and gravitational potential, $u_{G(h)}$, are given in eq. (6) and eq. (2), while the vdW attraction, $u_{v,perp(h)}$, uses eq. (3). Expected parameters from previous particle-wall experiments in Table 1 and considered consistent across the entire surface.

In the first model, the vdW potential at the defect with perpendicular alignment is the reference value for the vdW fitting parameter such that $X_{VDW}(x_{ref}, y_{ref}) = 1$ at the defect. The fitting parameter is then adjusted for every pixel in the simulation using the weighted average format in eq. (12) referenced to the defect pixel.

In the second model, precedent values for parallel and perpendicular vdW potentials define the possible range of the vdW fitting parameter. Starting from the net potential from eq. (14) and $X_{VDW}(x_{ref}, y_{ref}) = 1$ at the defect, the maximum and minimum simulation energies are used as bounds for a precedent-based vdW fitting parameter. The minimum pixel energy, u^{min}, corresponding to the planar LC surface while the maximum energy, u^{max}, is located at the defect. The maximum vdW fitting parameter at parallel LC interface is then calculated to be,

$$1.3 = \frac{X_{VDW}(u^{\min})}{X_{VDW}(u^{\max})} = \frac{\int_{0nm}^{40nm} u_v^{plan} dh}{\int_{0nm}^{40nm} u_v^{perp} dh} \quad (15)$$

for close approach separations between h=0nm and h=40nm and the properties in Table 1. For every simulated particle-wall energy pixel, $u_{i,pw}$, the vdW fitting parameter is,

$$X_{VDW}(x,y) = 1 + (1.3-1)u_{i,pw}(x,y) \Big/ \left(u_i^{\min}\right) \qquad (16)$$

to stay within the bounds of $X_{VDW}\left(u^{\max}\right) = 1$ and $X_{VDW}\left(u^{\min}\right) = 1.3$ for the extremes of perpendicular and parallel LC interfaces. Next, the steric constant, $\Gamma_S(x,y)$, is adjusted in eq. (6) used to minimize error at every pixel between the simulated particle-wall energy and the weighted average energy calculated from eq.(11) and eq.(12), respectively.

The third and final model considers an adjustable repulsion that varies with position. Starting from the X_{vdW} parameter from eq. (16) and net energy is from eq.(14) , the steric constant at the defect is fixed to the precedent value of $\Gamma_s^k\left(x_{ref}, y_{ref}\right) = 1986kT$ given in Table 1. $\Gamma_S(x,y)$ is then adjusted for all other pixels to minimize error between the simulated particle-wall energy and the weighted average energy calculated from eq.(11) and eq.(12), respectively, for every energy bin.

6.5 Results & Discussion

6.5.1 Surface Characterization

We begin by characterizing the LC surface and the point defects over which colloids will be dispersed over in aqueous solution. **Fig. 1(a)** illustrates optical images (from crossed polars) of the LC confined to a copper grid, demonstrating the synthesis of polymerized liquid crystals with multiple escaped radial defects due to homeotropic anchoring as described in previous work. The orientation of the liquid crystal at the aqueous-liquid crystal interface is parallel to the interface and appears bright with dark radial lines emanating from defects when viewed with crossed polarizers. **Fig. 1(b)** shows an isolated point defect with an escaped radial configuration that was used for analysis in subsequent figures. This image reveals spatially varying optical textures across the LC

surface in the vicinity of a surface defect, which previous works have determined arise from a near-perpendicular order of LC near the surface defect at the LC-water interface to planar order far from the surface defect. Combined with **Fig. 1(a)**, these images also demonstrate the birefringence of LC materials which, which in turn can tune the van der Waals potentials of materials interacting with these surfaces. Inspection of the birefringence map of **Fig. 1(c)** illustrates additional nuances in the order of LC in the vicinity of the defect in **Fig. 1(b)**, enabling quantification of the local average tilt angle inside of a liquid crystal film region and identification of potential local asymmetries in LC order. Lastly, **Fig. 1(d)** provides micron-height variations within 50 microns of the point defect in the center of the image and an inset with the corresponding AFM characterization of surface roughness. It is clear from this figure that the surface near the defect is optically diverse and topographically smooth.

It is important to relate the optical properties of a LC surface with point defects to their effects on colloidal interactions. Based on previous work by Abbott et al on examining van der Waals interactions near LC defects, patterned orientations of the LCs may be used to program van der Waals interactions between the LC films and colloids that approach the surfaces of the LC, therefore, accurate modeling on van der Waals interactions is necessary to predict ordering and self-assembly of particles near defects. Numerous measurements of van der Waals interactions from Israelshvilli,[299] Ducker,[300-301] and Milling[302] consider strong interactions between spheres and plates at separation distances where the van der Waals interactions are stronger and retardation effects are negligible. However, interactions at separations greater than 20 nm, relevant to work in this paper, are retarded and much weaker. Additionally, small-scale roughness further weakens the magnitude of

van der Waals attraction, as explained in Bevan et al.[78] Therefore, the synthesis of topographically smooth surfaces near the LC point defect in **Fig. 1** eliminates any large-scale gravitational variations and ensures small-scale smoothness of the surface near the defect that can impact measurements of van der Waals potentials between colloids dispersed over the LC defect.

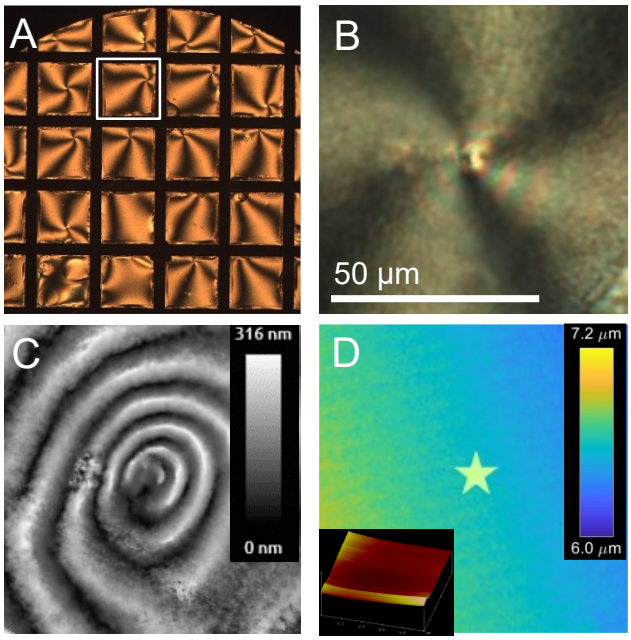

Figure 6-1 **Characterization of polymerized liquid crystal interface.** (A) The polymerized LC sample in TEM grid with grid size of 300 µm imaged by cross-polarizers, with the white box selected as a (B) escaped radial point defect imaged by cross-polarizers. (C) Average tilt angle and birefringence inside the LC film imaged with a PolScope with the same scale as (B). Measurements of the surface height profiles of the LC sample near the defect using optical profilometry (D) with the defect located at the center (star), and AFM (inset) for the 1µm by 1 µm region around a similar defect over a height scale of 200 nm.

6.5.2 Diffusing Colloids to Probe Energy Landscapes on Polymerized LC

Fig. 2 shows a snapshot of levitated concentrated colloids with adsorbed Pluronic, from our video microscopy experiment outline above, diffusing freely over and organized around the LC defect in **Fig. 2(b)**, with an adsorbed layer of Pluronic, dispersed in DI water. **Fig. 2(a)** qualitatively shows that there may be variations in the density profile of

colloids over the defect and these particles are largely homogenous in size. Particle tracking algorithms generate equilibrium diffusion trajectories over 90,000 frames, corresponding to 1.5 hours of PEG-coated particles as shown in **Fig. 2(b)** and **Fig. 2(c)**. **Fig. 2** summarizes the density distribution from experimental data divided into pixels of $2\mu m^2$ based on the location of the particle center. As measured by the optical imaging in **Fig. 1**, the defect is located within the coordinate of *(x,y) = (-4, -8)* μm, where it is evident that particles are less dense on top over the defect, but density increases further from the defect. This observation was consistent over time, which supports the significance of these average density profiles that show equilibrated Brownian motion and local variations.

Work by Bahukudumbi et al on imaging energy landscapes with concentrated particles explains that tracking freely diffusing particles over surface patterns or features is useful for measuring potential energy variations in *x,y*.[294] The observation time required for a single particle to statistically sample an entire landscape is long, motivating the use of concentrated ensembles to increase sampling of large area and energy profiles greater than ~kT. To maximize statistical sampling at the aqueous-LC interface, the particle density chosen ensures diffusion over all surface features without overcrowding. We note that unsampled areas in trajectory profile in **Fig. 2(c)** result from deposited particles due to unavoidable impurities in the sample that may cause surface heterogeneities. Slight variations in particle density over time in **Fig. 2(d)** cause some particles further from the defect to change their position in the focal plane. We believe these changes result from minor global gravitation tilt of the TEM slide; therefore, we focus our equilibrium analysis on the local density profile near the defect.

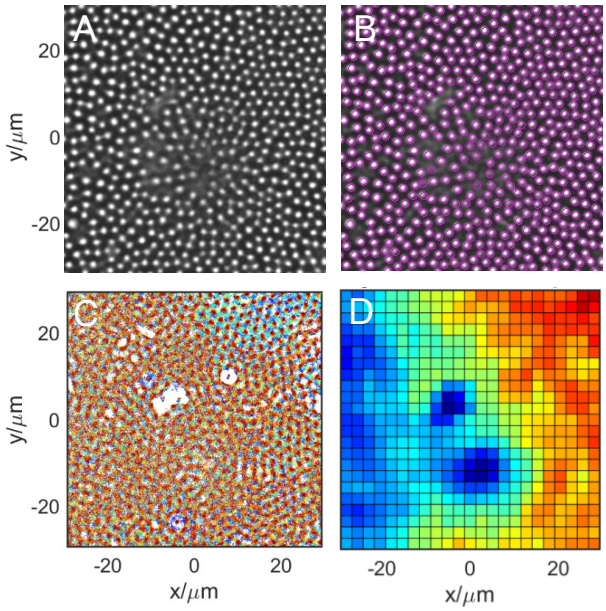

Figure 6-2 **Particles freely diffusing over LC polymerized surface.** Representative snapshot of particles imaged by optical microscopy (A) before and (B) after tracking particle centers where field of view is 60um x 60um. (C) Particle trajectories determined from equilibrium recordings where plotting scans from 0 min (blue) to 90 min (red). (D) Density distribution from the 90-minute equilibrium recordings where ρ/<ρ> = 0.7 (blue) – 1.3 (red).

6.5.2.1 **Table 1: Experiment and simulation parameters.** Values obtained from (a) precedent values from silica-silica studies on PEG interfaces[149], (b) handbook values[303], (c) precedent studies on LC interfaces,[304-305] and (d) eq. (5).

Parameter	Value	unit
$\Gamma_{S,si\text{-}si}$ [a]	1984	kT
δ [a]	0.283	nm^{-1}
a [a]	1.09	μm
ρ_p [a]	1960	g/cm^3
ρ_f [b]	1000	g/cm^3
ν_e [c]	2.83×10^{15}	s^{-1}
κ^{-} [a]	0.033	nm^{-1}
ε (silica[b], water[b], LC plan[c], LC perp[c])	3, 78, 18.4, 6.8	-
n (silica[b], water[b], LC plan[c], LC perp[c])	1.46, 1.6, 1.71, 1.53	-
A_{total} (plan, perp)[d]	1.12, 0.89	10^{-20} J
$A_{v=0}$ (plan, perp)[d]	0.21, 0.24	10^{-20} J
$A_{v>0}$ (plan, perp)[d]	0.91, 0.65	10^{-20} J

6.5.3 Potential energy at the LC surface

Because the density profiles are from non-invasive measurements of equilibrium interactions, we can interpret nonuniform distribution near the defect to understand how the anchoring and orientation of the point defect impacts interfacial interactions. The measured concentrated density profile, *p(x,y)*, in **Fig. 2 (d)** considers all particles in the system, and must be interpreted to determine single particle-wall interactions without the presence of multiparticle effects. Inverse MC simulations of the colloidal probe experiment are used to determine position-dependent potentials from ensemble behavior from the experimental density profile. Using the algorithm described in *Methods*, iterative simulations with density profiles $p_i(x,y)$ are compared to the experimental *p(x,y)* until conversion using eq. (9) and eq. (10).

Initialized by the parameters in **Table 1**, all energy fluctuations are dependent on the pixelized potential energy landscape, $u_i(x,y)$. The converged iteration of the simulation algorithm is shown in **Fig. 3**. The simulation rendering (**Fig. 3 (a)**) shares the same qualitative particle distribution as the experiment video (**Fig. 2 (a)**) with fewer particles located near the defect at *(x,y) = (4,-8)* and more particles in the top-right corner than the bottom-left. High agreement is also observed when comparing the density profiles of the simulation (**Fig. 3 (b)**) and experiment (**Fig. 2 (c)**) with lower density near the defect and an overall density gradient attributed by planar sample tilt. The simulations also capture the low density aggregate at *(x,y) = (-4,2)* demonstrating the diverse ability of the simulation method to interpret any feature based on the starting density profile. However, since this feature is unrelated to the aqueous-LC interface, we will disregard the density and energy variance at this location moving forward.

The position-dependent particle-wall energy of an individual colloidal probe, $u_{i,pw}(x,y)$, at each pixel determined by the converged simulations is shown in **Fig. 3 (c)**. The effect of sample tilt is considered in eq. (11) resulting in a planar energy landscape where the significant variations of >1kT occur near the anchoring defect at $(x,y) = (4,-8)$. As expected from the Boltzmann relationship, the positions of higher potential energy (**Fig. 3 (c)**) directly correlate with less statistically sampled positions from the simulated density profile (**Fig. 3 (b)**). The continuous boundary conditions and time-averaged multiparticle interactions in the simulations account for the entropic effects of ensemble particle behavior. Therefore, the position-dependent energy profile from the simulation can be entirely contributed to particle-wall effects at the aqueous-LC interface with a difference of ~4kT for a silica colloid at the given ensemble concentration. In our experimental observations, positions with increased particle-wall attraction led to higher measured particle densities as individual colloids diffuse to reduce their internal potential energy. To minimize the total free energy of the system, freely diffusing particles would continue to sample less attractive regions based on the differences in density and energy.[33] Our simulated energy landscape agrees with these observations with higher densities and lower potentials in the planar LC bulk, and lower densities and higher potentials at the LC defect.

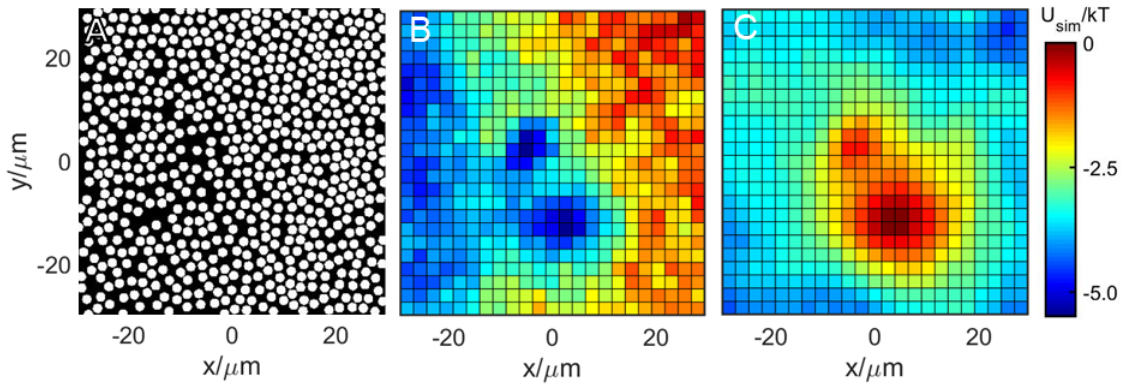

Figure 6-3 **Simulations of freely diffusing spheres using iMC method to compare experimental results in Fig. 2.** (A) Representative rendering of a simulation configuration at equilibrium. (B) Density distribution from the simulation with ρ/<ρ> = 0.7 (blue) – 1.3 (red). (C) Interfacial energy contribution from particle-wall interactions alone $u_{i,pw}$ at each pixel determined by eq. (11).

6.5.4 Interpreting the energy landscape

Further insights into the particle-LC interaction are found by interpreting the simulated energy landscape $u_{MC,pw}(x,y)$ using the net superposition particle-wall potential in eq. (1). However, neither the video microscopy technique nor the MC simulations include any information on particle height or separation relative to the substrate. In reality, the particles are constantly diffusing normal to the substrate based on Brownian motion and their particle-wall potential. To capture all sampled separations through theory, we consider the weighted average potential energy, $\langle u(h) \rangle$, from eq. (12). This method has the benefit of allowing for direct comparison between a height-dependent theoretical potential to the simulated energy value at each individual pixel. We use this technique to compare the measured and theoretical interactions with three different models described in *Methods* and discussed in detail below.

To understand the position-dependent energy landscape from the simulations, we first consider the superposition of attractive gravitational (eq. (2)), van der Waals (eq. (3)), and repulsive steric (eq. (6)) interactions from physiosorbed PEG on both particle and

LC wall, at individual pixels.[85] As explained in the first model in *Methods*, the potential of the pixel at the LC defect ($(x_{ref},y_{ref}) = (4,-8)$) is fixed based on previous polymerized LC studies and parameters given in **Table 1**. Using eq. (14), $X_{vdW}(x,y)$ is fit to every simulation pixel using $u_{i,pw}(x,y)$ using the weighted average in eq. (12), as in **Fig. 4(d)**. The fitting parameter is fixed at the defect pixel to $X_{VDW}(x_{ref}, y_{ref}) = 1$ and gradually increases to a constant value radially.

In **Fig. 4(a)**, the vdW potential is evaluated for every pixel of 2D energy landscape at initial contact between the polymer brushes, calculated by $X_{VDW}(x,y)u_V^{perp}(2Lo)$. The polymer brush length is the average of the adsorbed PEG on both the microparticle and the LC surface, at contact (where the interaction is equal to 0.1 kT, defined as the limit of sensitivity of our interaction measurements as described in previous publications (eq. (7)). As with the fitting parameter, the vdW landscape varies radially from the defect to a constant value at the bulk where the LC orientation is consistantly planar. At all positions, the vdW potential is attractive towards the substrate, verifying the need for steric stabilization to prevent deposition in this system. **Fig. 4 (g)** is a height-dependent profile of the vdW potential across the defect at $y=-8\mu m$. As expected, vdW potentials decay as separation between surfaces increase, with the degree of attraction upon approach varying based on proximity to the LC defect at $x=4\mu m$.

The validity of this model is supported by the explanation of experimental results and selection of fitting parameter. First, the greater vdW attraction in the LC bulk is consistent with the higher densities in experiments and simulations. Since gravitational and steric interactions are equivalent at all positions in this model, the driving potential energy gradient for particle densification is the vdW landscape. Therefore, as individual colloids

diffuse towards the planar bulk LC, an effective repulsion of the homeotropic LC defect occurs, leading to the density profiles observed in **Fig. 2(d)** and **Fig. 3(b)**. Through the iterative simulation method, these position-dependent density variations are interpreted as a vdW potential landscape.

Adjusting the multiplier for the vdW potential, X_{vdW}, is consistent with changing the Hamaker constant, $A(l)$. Because refractive index directly correlates to the Hamaker constant of the vdW potential, it is reasonable to assume that LC orientation, which affects optical properties, could impact the Hamaker constant as well.[295] Previous experimental and theoretical studies also calculate variations in Hamaker values based on interfacial LC anchoring.[293] We observe a continuous change in X_{vdW} from the bulk to the defect with a gradual change from parallel to perpendicular interfacial anchoring. Additionally, images from cross polarizer in **Fig. 1** show changes in the bulk refractive index with position relative the defect. Connecting the LC optical properties, vdW theory, and interfacial potentials verifies that changes to X_{vdW} is consistent with a multiplier to the Hamaker constant in this case. While the transition of the vdW multiplier with LC orientation is consistent with precedent ($X_{planar}>X_{vdW}(x_{ref},y_{ref})$), the magnitude of this change does not agree with previous findings (3.2 vs. 1.3, see *Methods*).[293] This inconsistency motivates a further investigation on the effect of steric layer thickness and electrostatic repulsion on particle-wall interactions at polymerized LC interfaces.

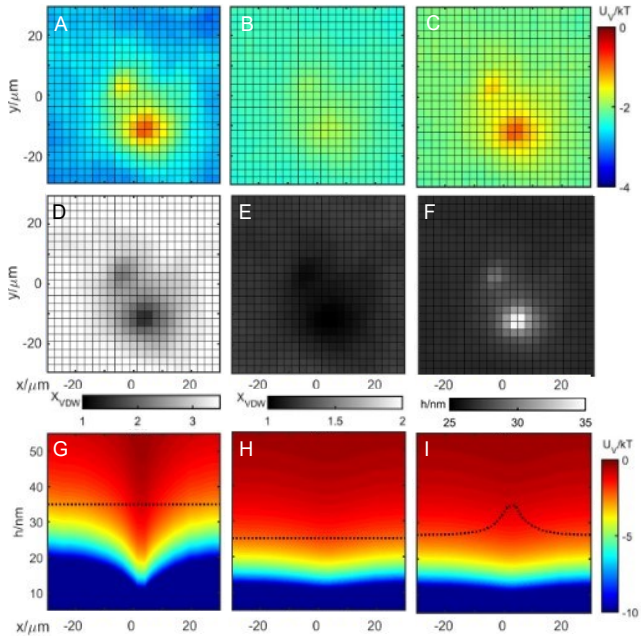

Figure 6-4 **Energy landscapes between silica particles and a polymerized LC interface from the converged simulation and experimental data.** (A, D) vdW component of the particle-wall energy from eq. (14) at $h = 2Lo$ with vdW fitting parameter, $X_{vdW}(x,y)$ from 1 (black) to 3.5 (white) calculated by fitting eq. (12) to each simulation pixel, calculated at 2Lo. (B, E) vdW component of the particle-wall energy from eq. (14) at $h = 2Lo$ with vdW fitting parameter, $X_{vdW}(x,y)$, fixed between 1 and 1.3, and Γ_S=134kT fit for all pixels. (C, F) vdW component of the particle-wall energy from eq. (14) where $\Gamma_S(x,y)$ is fit individually to each pixel leading to polymer brush thickness, $2Lo$, that varies with position by eq. (7). (G-I) Height-dependent vdW energy landscapes at y = -8 μm energy from the vdW component of eq. (14) with the dashed line at $h = 2Lo$ from eq. (7).

In **Fig. 4(b,e,h)**, the simulated energy landscapes are interpreted by considering the expected Hamaker and vdW potentials from precedent with an adjustable repulsion as a second model for analysis.[293] As explained in *Methods* and in eq. (16), the vdW fitting parameter at each pixel, $X_{vdW}(x,y)$, is fixed to known values (**Fig. 4(e)**) and the polymer brush density, $\Gamma_S(x,y)$, is adjusted equally across the entire surface to account for any changes in surface repulsion. The resulting energy profile at $2Lo$ evaluated for every pixel using eq. (7), and the height-dependent profile of the vdW potential across the defect at y=-$8\mu m$ in **Fig. 4(b)** and **Fig. 4(h)** respectively. As with the previous model, LC with parallel orientation is more attractive than the perpendicular defect. Given that gravitational and repulsive potentials are equal across the surface, the particles diffuse from areas of

higher to lower energy based on the vdW potentials alone, leading to the density profiles observed experimentally and through simulation. Compared to the first model, the weaker repulsion allows for closer approach of the silica particles to the LC surface leading to similar gradients in vdW potentials and equivalent density profiles in experiment and simulation at a different separation.

One interpretation of the adjustable repulsion is due to changes to the polymer brush thickness at the aqueous-LC interface. In this first method, we assumed that PEG forms equivalent brushes at aqueous-LC interfaces and the aqueous-silica interfaces. However, the calculated *2Lo* from eq. (7) is much smaller in this case. Numerous studies demonstrate the consistency of PEG layer formation on the silica colloids is consistently $Lo=17nm$.[34, 149] Therefore, the remaining change in *2Lo* can be attributed to a short brush thickness of $Lo=6nm$ at the aqueous-LC interface. Previous studies on ionic surfactants and phospholipids show different brush formation at aqueous-LC interfaces than at aqueous-solid interfaces due to molecular realignment and penetration at the interface.[306-307] Even though we do not expect this realignment in our polymerized LC surface, the brush formation could still differ at aqueous-LC interfaces. We posit that the difference in hydrophobicity between the LC and the octadecanol-functionalized silica colloids may create asymmetry in adsorbed mass density of the PEG triblock copolymer. Briefly, the adsorbed amount of polymer on a surface and its architecture depends on a balance of relative segment, solvent, and surface interactions. Based on our results, it is clear that the OD-silica colloids are more hydrophobic than the LC and consistently form 17nm thick PEG layers, therefore, lateral crowding of PEG molecules in the adsorbed layer forces the PEO tails in the triblock further into solution, while the PPO block remains anchored,

compared to the slightly thinner layer architecture on the LC.[39, 46]

However, by adjusting repulsion equally across the entire surface, kT-scale error exists when comparing theory to simulation. In **Fig. 4(c,f,i)**, the repulsion, $\Gamma_S(x,y)$, is individually fit to every simulation pixel given the precedent-based vdW fitting parameter from eq. (16), as explained in *Methods*. This model eliminates all error between theory, simulation, and experiment by allowing additional adjustability each pixel.

Variation in the fitted repulsion can also guide our understanding of how LC orientation affects interfacial interactions. Using the precedent-based theoretical vdW potentials and the fixed gravitational potential, all remaining changes to particle-wall interactions can be attributed to changes in either steric or electrostatic repulsion. In general, increased repulsion exists near the defect than in the bulk sample. If all variation in repulsion is attributed to steric repulsion, polymer brush thickness, *Lo* from eq. (7), can be examined in **Fig. 4(f)** with a thicker layer near the defect. Given a thickness of $Lo=17nm$ on the silica particle, the defect and parallel bulk LC have polymer brush thicknesses of $Lo=15nm$ and $Lo=7nm$, respectively. We can therefore conclude that interfacial LC orientation has a strong effect of hydrophobicity driving competitive adsorption of PEG to the defect over the bulk. Changes in the range of repulsion between the parallel and perpendicular LC interface could also be attributed to variation in electrostatic repulsion through zeta potential. Based on previous work by Mathai and Ottwewill, adsorption on nonionic surfactants on hydrophobic surfaces causes a shift in the plane of shear, which leads to a decrease in the zeta potential.[308-309] However, as new studies on weak interactions at aqueous-LC interfaces emerge, any of these models may reveal to be the most accurate.

6.5.5 Reproducibility and Applicability

Three total replicates of the colloidal probe experiment and IMC simulation analysis were performed. Each experiment is summarized in **Fig. 5** using the energy landscape from the third model (as in **Fig. 4(i)**) and the optical characterization from cross polarizer and polscope images (as in **Fig. 1(b,c)**). Full analyses of the sample in **Fig. 5(b)** and **Fig. 5(c)** are shown in **SI.1** and **SI.2**, respectively. Each experiment was performed on a different polymerized LC defect in an individual TEM grid. The three replicates were measured to be topographically smooth and optically diverse with a point defect identified by cross polarized profiles. Each sample has a unique polscope measurement that we attribute to differences in the number of birefringence orders that occur between the defect and the 'far-field' LC for the samples. This difference occurs due to differences in the thicknesses of the LC samples. Thicker samples will progress through these additional birefringence orders and have more of the concentric black and white fringes in the PolScope images. We stress that though these differences in birefringence order through the thickness of the LC film may differ, that the LC order nearest the LC-aqueous surface encodes differences in vdW potentials. The vdW attraction and 2*Lo* profiles are strikingly similar among the three cases and characterized by a gradient that decays over ~5μm into the parallel bulk LC.

In our observations, the interfacial interactions decay at approximately the same rate from the homeotropic defect to the planar bulk LC regardless of PolScope imaging for these equivalently produced samples. Typically, surface-to-surface interactions at small separations are only impacted by material properties equivalent distance into the sample.[299] Therefore, bulk realignment creating the gradients in the PolScope image are uncorrelated

to the resulting interfacial energy profiles beyond the location of the defect. To further support the claim that the surfaces are reproducible, the LC order near the surface is what we believe is controlling the van der Waals interactions. We focus on defects and nearby regions as these surface regions are where we expect the greatest amount of change in LC order and, accordingly, van der Waals interactions. Understanding the connection between LC orientation, optical properties and interactions at an aqueous interface are critical to developing assembly-based applications. The energy landscapes uncovered in this study are on the scale of ~10kT, within the scope of tunable interactions for controlled self-assembly for colloidal and nanoscale systems.[310] While these experiments and simulations revealed interesting characteristics of aqueous-LC interfaces, the same method can be applied to a wide variety of aqueous surface systems. Given that particles can be sterically stabilized, interfacial interactions profiles can be uncovered including gravitational, vdW, electrostatic or steric interactions, as discussed previously. For LC interfaces specifically, future studies could reveal interactions at other topological defects or with other macromolecules adsorbed to the surface. Controlling the LC alignment, surfactant concentration, or electrolyte quality during a single measurement could reveal time-dependent surface features not possible in equilibrium studies. Overall, we reveal consistent vdW attraction and steric layer profiles based on molecular orientation at aqueous-LC interfaces in three different samples, demonstrating unique insights that drive interfacial assembly.

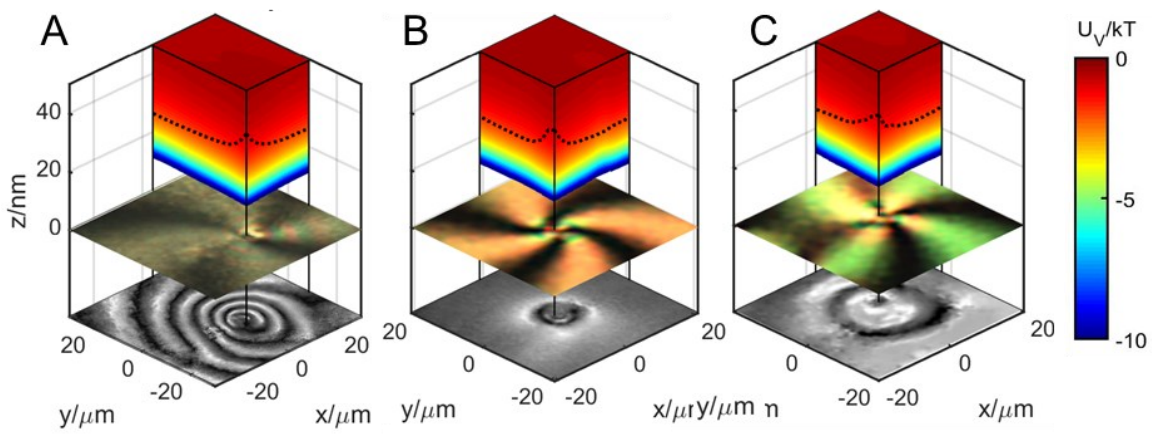

Figure 6-5 **Experimentally determined potential between silica particles and polymerized LC substrate.** One quadrant of the energy landscape is plotted such that the cut-out is located at the defect and the dashed line is the expected brush thickness, *2Lo,* from eq. (7) using the method for Fig. 4 (C, F, I). Potentials are shown for the current case (A), and addition experiments outlined for (B) in SI.1 and (C) in SI.2.

6.6 Conclusions

Diffusing colloidal probe experiments and simulations use concentrated ensembles of diffusing silica particles at an aqueous-LC interface to understand the orientation-dependent surface potentials of the polymerized LC substrate. Colloids were stabilized from aggregation and deposition using non-ionic polymers adsorbed to both the particle and surface, and then imaged at equilibrium freely diffusing over a LC point defect. Initial observations show lower particle densities near the perpendicular defect than the parallel bulk LC despite the sample being topographically flat. Replicating the measurements using an inverse MC simulation technique reveals a potential energy gradient that decreases from a maximum at the defect to a plateaued minimum in the bulk. Each position-based pixel in the 2D simulation converges to a potential energy value that describes the density gradient of freely diffusing particles at the substrate.

Given that the net particle-substrate interaction is the superposition of gravitational, steric, and vdW potentials normal to the surface, theoretical models provide insight on the

effect each interaction on their ordering near the defect. Relative to the defect, vdW attraction is stronger for LC interfaces with parallel molecular orientation than perpendicular orientation. Additional heterogeneities were attributed to changes in steric repulsion due to surface potential changes and subsequent changes in adsorbed layer architecture. In general, we observe weaker adsorption of polymer brushes at the aqueous-LC interface than on the silica colloids due to differences in hydrophobicity. Repulsive gradients along the LC interface are also be attributed to variations in molecular orientation: hydrophobicity (brush thickness and steric repulsion) and surface charge (zeta potential and electrostatic repulsion) both depend on the interfacial anchoring of the polymerized LC. Some combination of a thicker polymer layer, stronger surface charge and weaker vdW attraction led to a significantly weaker attraction at the LC defect than the bulk material. Since the diffusing probe measurements are colloidal-scale systems, the same interactions can be applied to nanoscale and micro-scale features where self-assembly is determined by potentials on the scale of kT.

6.7 Supporting Information

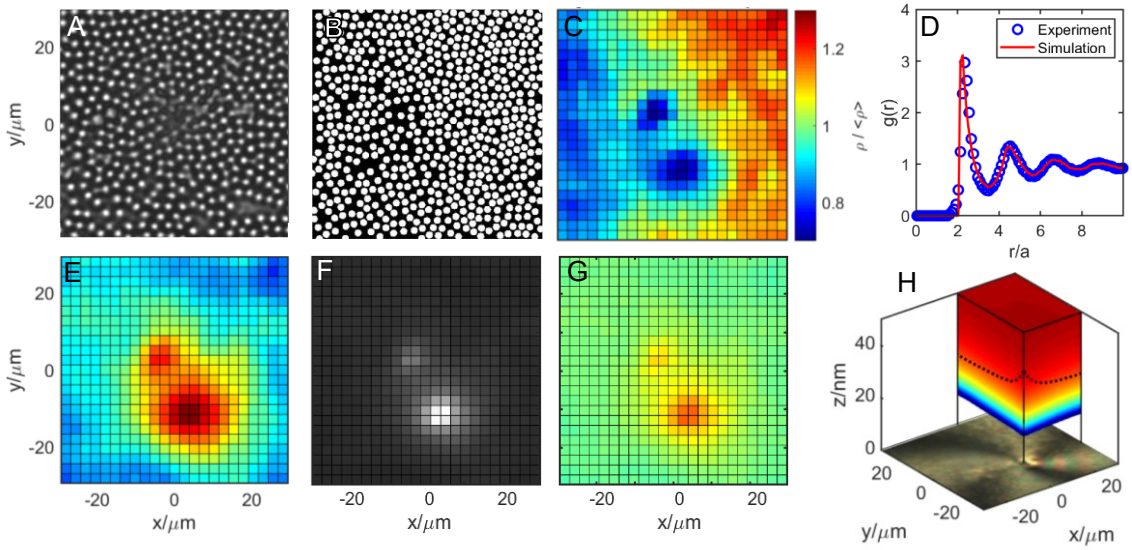

Figure 6-6 **Summary of diffusing colloidal probe experiment results and findings from the sample in Fig. 5.(a).** Representative snapshot of particles imaged by optical microscopy (A) and rendering from equilibrium simulations (B). (C) Density map constructed from experimental particle sampling used to find agreement between experiment and simulation. (D) Pair correlation function for all particles in experiment (blue circles) and simulation (red lines). (E) Interfacial energy contribution from particle-wall interactions alone at each pixel determined by eq. (11) between $u_{i,pw}$= -6kT (blue) and $u_{i,pw}$=0kT (red). (F) Polymer brush thickness, *2Lo* from eq. (7)., varying by position between *h*=25nm (black) and *h*=35nm (white). (G) van der Waals component of the particle-wall energy from eq. (14) where $\Gamma_S(x,y)$ is fit individually to each pixel between calculated at *h* = *2Lo* from -4kT (red) to 0kT (blue). (H) One quadrant of the energy landscape is plotted such that the cut-out is located at the defect and the dashed line is the expected particle-wall separation, *2Lo,* with the cross-polarizer image shown at *z*=0nm as explained in Fig. 5. (a).

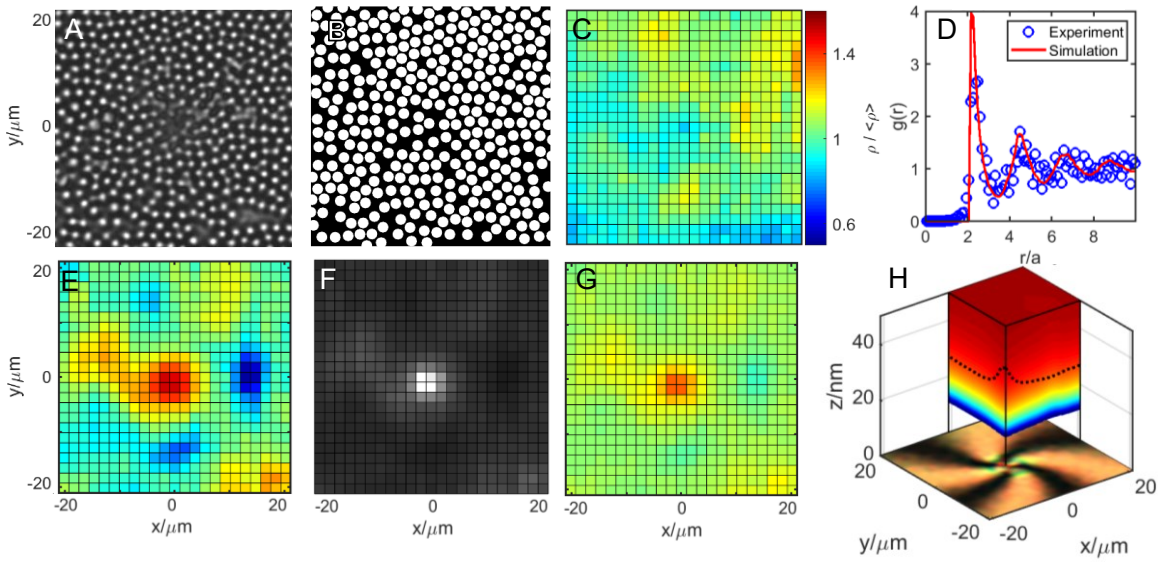

Figure 6-7 **Summary of diffusing colloidal probe experiment results and findings from the sample in Fig. 5.(b).** Representative snapshot of particles imaged by optical microscopy (A) and rendering from equilibrium simulations (B). (C) Density map constructed from experimental particle sampling used to find agreement between experiment and simulation. (D) Pair correlation function for all particles in experiment (blue circles) and simulation (red lines). (E) Interfacial energy contribution from particle-wall interactions alone at each pixel determined by eq. (11) between $u_{i,pw}$= -6kT (blue) and $u_{i,pw}$=0kT (red). (F) Polymer brush thickness, *2Lo* from eq. (7)., varying by position between *h*=25nm (black) and *h*=35nm (white). (G) van der Waals component of the particle-wall energy from eq. (14) where $\Gamma_S(x,y)$ is fit individually to each pixel between calculated at *h = 2Lo* from -4kT (red) to 0kT (blue). (H) One quadrant of the energy landscape is plotted such that the cut-out is located at the defect and the dashed line is the expected particle-wall separation, *2Lo,* with the cross-polarizer image shown at *z*=0nm as explained in Fig. 5. (b).

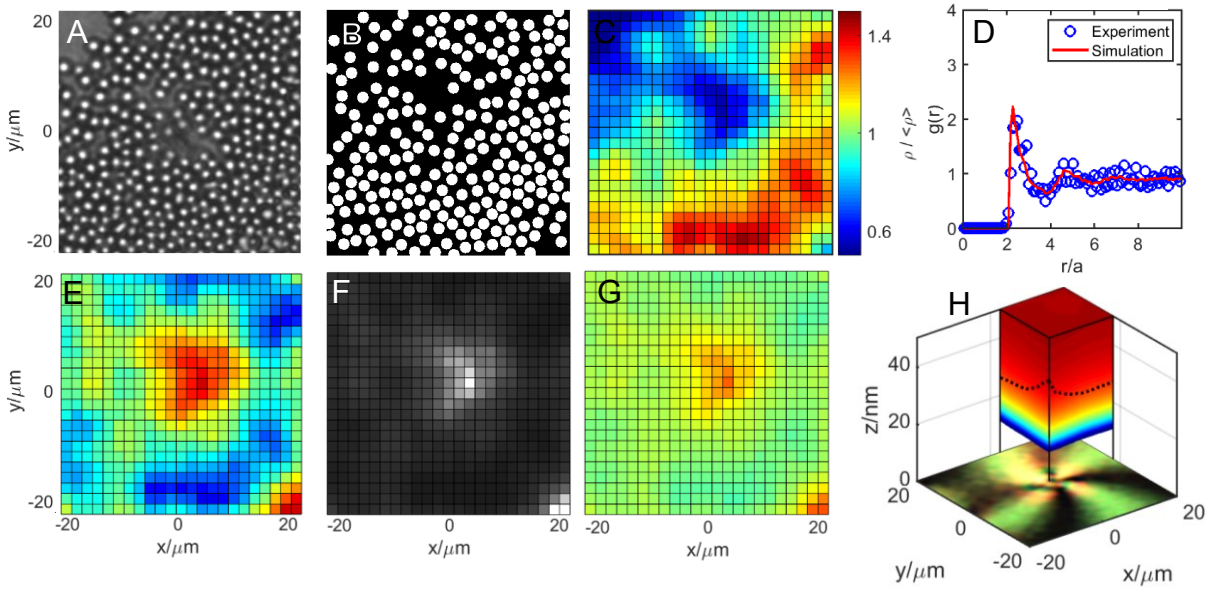

Figure 6-8 **Summary of diffusing colloidal probe experiment results and findings from the sample in Fig. 5.(c).** Representative snapshot of particles imaged by optical microscopy (A) and rendering from equilibrium simulations (B). (C) Density map constructed from experimental particle sampling used to find agreement between experiment and simulation. (D) Pair correlation function for all particles in experiment (blue circles) and simulation (red lines). (E) Interfacial energy contribution from particle-wall interactions alone at each pixel determined by eq. (11) between $u_{i,pw}$= -6kT (blue) and $u_{i,pw}$=0kT (red). (F) Polymer brush thickness, *2Lo* from eq. (7)., varying by position between *h*=25nm (black) and *h*=35nm (white). (G) van der Waals component of the particle-wall energy from eq. (14) where $\Gamma_S(x,y)$ is fit individually to each pixel between calculated at *h* = *2Lo* from -4kT (red) to 0kT (blue). (H) One quadrant of the energy landscape is plotted such that the cut-out is located at the defect and the dashed line is the expected particle-wall separation, *2Lo,* with the cross-polarizer image shown at *z*=0nm as explained in Fig. 5. (c).

7 CONCLUSIONS AND OUTLOOK

7.1 Summary and Conclusion

This dissertation contained three main focuses. First, the fundamental understanding of ethylene oxide (PEG) and zwitterionic polymer (ZI) layer solution thermodynamics mediated by specific ion or Hofmeister effects. Second, interactions and dimensions of PEG and ZI copolymer layers when large blood proteins are added to solution. Last, a measure of asymmetric interactions between PEG and ZI coated microparticles and adsorbed layers of mucin in various solution conditions. The last chapter

presents work done in a collaboration project that led to a first-author publication, however, the dissertation conclusions will focus on the three main aims. The following conclusions are based on each of these focuses as presented in this dissertation.

7.1.1 Specific Ion Effects on Dimensions and Interactions of Adsorbed PEG and ZI Copolymers

The effect of divalent salts on dimensions and interactions of zwitterionic copolymer coatings compared to PEG was explored. MgSO4, the choice of divalent salt, is a known water structure breaker, whereas NaCl does not break water structure therefore, specific ion effects are explored using salt mixtures. An assay was developed to systematically explore symmetric interactions of PEG, PMAPS, and PMPC with various NaCl and MgSO4 salt concentrations. Experimentation and modeling interactions using a superposition of attractive and repulsive colloidal interactions reveals unique behavior for each copolymer: PEG layer dimensions are insensitive to NaCl (nonspecific effect), but collapse at over 200 mM MgSO4, regardless of the initial concentration of NaCl. PMAPS layers exhibit typical antipolyelectrolyte effect with NaCl, where increasing NaCl extends PMAPS brushes to ~85% of their contour length. PMAPS layers also collapse with MgSO4, but the amount of MgSO4 required to collapse PMAPS layers scales proportionally with the initial NaCl condition. In stark contrast, PMPC layers are insensitive to both NaCl and excess MgSO4, demonstrating a nonspecific effect even with salts that typically break water structure. Findings include a significant understanding of the balance of polymer brush structure, dipole moments, and the balance between enthalpic and entropic contributions of solvent quality mediated interactions. This work demonstrates that PEG has a lower dipole moment than ZI polymers and exhibits typical

phase behavior with chaotropic salts showing that water structure (entropy) is responsible for the phase separation of PEG from water. PMAPS layer collapse demonstrate a competition between initial solvation of PMAPS layers with NaCl and the degree of water structure breaking required for phase separation.

7.1.2 Blood Protein Exclusion from Adsorbed PEG and Zwitterionic Copolymer Brushes

We used the two most abundant blood proteins, serum albumin and IgG and found that neither protein forms a 'protein corona' around adsorbed layers of PEG. We developed a carefully controlled experimental assay and performed equilibrium analysis to reveal quantitatively and qualitatively interesting behavior for both proteins, even though they differ in shape, function, and biophysical properties. Layer thickness and colloidal interactions revealed that PEG layer thickness remained constant, and the origin of increased attraction is from progressively increasing depletion of the protein from the polymer layer. Careful theoretical modeling reveals that depletion attraction can be modeled using modified AO theory and systematic adjustments of the osmotic pressure difference and excluded volume effects, reflecting the need to adapt traditional models to describe soft interactions between the proteins and polymers. Our theoretical models of depletion of soft proteins from soft polymer layers show that both proteins can penetrate the PEG layer to some degree and may partition between the polymer gap and the bulk solution. We used available theory of hard sphere exclusion from hard surfaces systematically adjusted the osmotic pressure term and excluded volume term to self-consistently approximate the origin of weakened blood protein exclusion from PEG

brushes. Our assay is free from surface heterogeneities, and we believe that this could be a useful tool for probing polymer interactions with numerous biomacromolecules.

Ultimately, our results provide a strong foundation to study protein interactions with polymer coated surfaces for drug delivery applications with minimal invasiveness and maximum sensitivity, and statistical significance. Future work includes developing an accurate theoretical model to describe the balance of globular protein exclusion and penetration between two soft polymer layers. Additionally, we recognize the importance of including a study on the synergistic effects of these proteins, and the effect of grafting the polymer layers.

3D trajectories and *kT*-scale interactions potentials were also used to examine symmetric interactions of adsorbed zwitterionic triblock (ZItb) copolymers, PMPCtb and PMAPStb, at high and low molecular mediated by solutions of high molecular weight blood proteins, BSA and IgG. BSA, at physiological concentrations, was found to be weakly excluded from high Mw PMPCtb but formed an adsorbed layer (corona) on high Mw PMAPStb. IgG, an order of magnitude higher Mw than both copolymers lead to the formation of defective layers on the particle and wall. Similar symmetric interaction assays with lower Mw PMPCtb and PMAPStb confirmed the hypothesis that proteins may be displacing zwitterionic copolymers off the surface leading to defective layers that cause local binding events on heterogenous surfaces. Normal trajectories show a succession of increasing timescales of intermittent binding events until colloids are completely deposited at 2.5 g/L IgG and 40 g/L BSA for both copolymers.

Our results in this work are significant in that they contrast significantly with similarly physiosorbed systems with PEG that did not show desorption, i.e., PEG was irreversibly adsorbed to the colloid and wall and the layer was intact at high BSA and IgG concentrations. Our results therefore indicate not only a molecular weight-driven displacement, which has been suggested I previous literature, but suggests an interplay of segment, surface, protein, solvent interactions that favor protein adsorption on the surface compared to zwitterionic copolymers. Even though TIRM was not used to measure kinetics of displaced layers, equilibrium analysis shows the effect of long-term displacement on the intactness of the adsorbed layer and suggests a potential examination of the kinetics of zwitterionic polymer-protein displacement. Ultimately, our results show that while adsorbed systems are easy, scalable, and seem to form intact layers with PEG copolymers, zwitterionic copolymers have more complex, nonnegligible interactions with blood proteins and may not be inert to blood proteins at physiological conditions when these copolymers are physiosorbed to the surface.

7.1.3 kT-Scale Repulsion between Polymer-Coated Colloids and Mucin

We employed three dimensional random walks, with nanometer resolution, from super resolution microscopy and evanescent wave scattering couple with equilibrium statistical mechanical analysis of polymer-mucin interactions. We found that PEG, PMPC, and PMAPS triblock copolymer coated microparticles exhibit net repulsive interactions with adsorbed mucin, no intermittent binding indicating any bridges or mucoadhesive interactions at the kT-scale. Intensity analysis reveals mucin makes 250 nm thick layers in 150 mM NaCl. Control experiments show that F108, PMPC, and PMAPS architecture and layer thickness are unperturbed by low pH and 100 mM $CaCl_2$. Addition of excess DTT

may have stiffened and decreased the thickness of mucin layers according to the steepness of the repulsion, but the net measured interactions are consistently repulsive regardless of the solvent condition or copolymer molecular weight.

Net repulsive asymmetric interactions between ethylene oxide and zwitterionic synthetic macromolecules and mucin indicate PEG, PMPC, and PMAPS are suitable mucopenetrating coatings for nanoparticles. pH and calcium may impact the structure/layer architecture of adsorbed mucin, i.e., mucin- mucin interactions, but mucin remains extended when adsorbed to hydrophobic surfaces. Ultimately, our interactions provide a strong foundation for reconciling conflicting views on mucoadhesion and mucopenetration and provide a template for designing particles with chemically modified coatings of PEG and ZI polymers to employ integrated mucopenetrating and mucoadhesive properties with specific interactions mediated by solvent conditions.

7.2 Future Work

This dissertation demonstrates our understanding of the molecular scale interactions of PEG and zwitterionic copolymer adsorbed layers in various solution conditions. We altered ionic strength and valency, added high concentrations of the most abundant blood proteins, and introduced asymmetric interactions between these polymers and mucus. Our findings lend themselves to interesting future directions in both protein and mucus interactions with polymer-coated colloids.

7.2.1 An intermediate strategy between grafting and physisorbing

Well-defined graft copolymers have attracted increasing attention for the applications as well as the physical properties. In addition, the grafting technique provides a stable platform against desorption and establishes long-term chemical stability because of its covalent nature in contrast to surface coating modifications which are unstable over time and do not prevent desorption.[311] Two methods of forming polymer layers include grafting or physisorbing. As mentioned previously, physisorbing is a simple, scalable, and industrially realistic method for steric stabilization. However, our results show that not all polymer coatings adsorb irreversibly. Therefore, chemically grafting layers seems to be a promising and robust solution. However, grafting from and to surfaces is typically much more difficult practically to scale up to industrial processes. Grafting-from method has limitation that include the difficulty of characterizing the side chains, lack of accurate characterization of the number of side chains introduced as well as the degree of polymerization and molecular weight distribution which may require the side chains be dissected from the backbone polymers. Chemical grafting limitations generally are impeded since the synthesis of homopolymer as a by-product may be difficult to extract, and harsh chemical are typically used. Moreover, radiation grafting may lead to serious degradation and/or decomposition of the polymer.[312] Therefore, there is a need to find a metho that is a union of grafting and adsorbing.

Metal catalyzed azide/alkyne ‘click’ reactions represent one of the few highly efficient functionalization reactions, combining both high efficiency with a high tolerance of functional groups and solvents. The reaction in the context of click reactions on surfaces is especially important since over 200 publications have been published and dozens of

patents filed using click chemistry to functionalize surfaces.[313-316] One of the main advantages of click reactions is the tunability of polymeric functional groups. On surfaces specifically, a large variety of click reactions on self-assembled monolayers, polymeric surfaces, layer by layer assemblies, block copolymer micelles, and liposomes have been reported. Click chemistries applied to polymers on surfaces have been applied to both grafting-to and grafting-from techniques to enhance the attachment of polymers onto surfaces.

Current work in our group in conjunction with Dr. Margarita Herrera-Alonso's group at Colorado State University involves click chemistry methods to graft zwitterionic copolymers onto azido-silane hydrophobic surfaces via a copper-catalyzed click reaction. Preliminary data shows that this reaction successfully leads to thick, solvated zwitterionic brushes on azide-silane modified glass colloids and slides and has potential to prevent desorption when IgG is introduced into solution. Future work includes the robust characterization of these layers in more concentrated solutions of IgG and protein mixtures to fully evaluate the stability and intactness of these layers against biological macromolecules with higher molecular weights and interactions with the solvent and surface. Additionally, we can use this chemistry to form robustly stable layers of zwitterionic coatings and use a combination of flow assays previously done in our group to flow a mixture of blood proteins, i.e. human serum, and be able to understand multiple protein-polymer interactions and see what structures are formed.

7.2.2 pH-tunable weak attraction between polymer coated colloids and mucins

By employing Total Internal Reflection Microscopy (TIRM) we will work to directly and non-intrusively measure kT and nanometer scale interactions between particles and mucus, with and without boronic acid targeting moieties. Boronic acids were previously introduced to nanocarriers because of their rapid and reversible reaction with 1,2- or 1,3-diols and have been demonstrated to be useful in the selective recognition of sialic acids. The affinity and selectivity of boronic acids to sialic acids, as well as their non-immunogenic and chemical versatility, can be harnessed to prolong retention times through a mucoadhesive effect. Sialic acids exist as the terminal units of cell surface glycans or glycolipids and glycoproteins, making them important molecular targets for delivery to cells with altered cellular status and environments. Boronic acid binding affinity and kinetics are, however, highly sensitive to the chemical structure of the boronic acid, the diol-bearing compound, as well as system pH. Our group will study the combined effects of boronic acid chemistry and surface presentation using three types of boronic acid derivatives: a Wulff-type boronic acid (WBA), benzoboroxole (BOX), and 3-phenylboronic acid (3PBA). These differ in the pKa of their acids (5.2, 7.2 and 8.2, respectively), hence their complexation pH which is relevant for mucus in various regions physiologically that differ in their pH milieu. We will also study the effect of boronic acid multivalent presentation on polymer-mucus interaction using different densities of peripheral functionality.

7.2.3 Colloid transport through mucus

Previous work in the group by Julia Swavola on transport of colloids through mucus was motivated by comparing gradient and self-diffusion enables a thorough analysis of

governing interactions to determining a complete empirical solution for diffusion. While colloidal diffusion is known to many fields, specifically in mucosal drug transport, direct, simple, and rigorous experimental techniques to measure diffusion experimentally are limited. Preceding work by Swavola elucidated specific and nonspecific interactions that affect colloidal diffusion as applied to diffusion of drug delivery particles though mucus using fluorescence recovery after photo-bleaching (FRAP) to measure self-diffusion and an assembly of a microfluidic device to measure flow at low Reynolds numbers. Swavola's work examined self-diffusion of bovine serum albumin (BSA) and Conconavalin-A (ConA) polymers and colloidal probes coated with BSA and Pluronic colloids and diffusion into mucus. Future work includes resuscitating this protocol and exploring diffusion of PEG and ZI coated particles in mucus in various solution conditions, motivated by results that show that net interactions of PEG and ZI coated microparticles with mucin layers are net repulsive, and particles remain thermodynamically stable.

As mentioned previously in *Chapter 5*, carrier transport rate across mucus is enhanced if carriers are small enough to avoid steric blocking, hydrophilic so as to circumvent hydrophobic interactions with the non-glycosylated protein regions, and electrically neutral. Although mucoadhesion had been explored to facilitate drug delivery several decades ago, more recent research has shown that nonadheisve PEG-coated particles show enhanced penetration and transport through mucus. Investigating weak biding is based on our hypothesis that viruses penetrate and transport through mucus via kT-scale attractive interactions that provides a thermodynamic driving force for partitioning but is also weak enough to allow for Brownian motion and diffusive transport.

Zwitterionic-coated particles are stable in the presence of mucus in various conditions, which may affect mucus architecture, and has repulsive interactions with mucus in various solution conditions that affect mucus architecture, as we show clearly in Chapter 5. Our future directions include checking its diffusivity in mucus using FRAP, and we plan to then measure diffusion into mucus in the microfluidic device bult by Swavola. These experiments would provide a model to attach boronic acids that provide weak attraction to mucus based on TIRM measurements, and the check how adding such attraction affects thermodynamic driving forces for partitioning of NPs into mucus films across their interface.

On the modeling side, we will use our knowledge of weak interactions to rigorously model particle partitioning and diffusion in mucus pores. Based on foundational work by Ongston,[317-318] Anderson,[231] and Radke,[236] we will adapt hard sphere partitioning equations that include hydrodynamics and excluded volume terms and incorporate weak attractive interactions and soft polymer layers and mucus pores to accurately model data and predict permeation and diffusion of ZI and PEG coated colloids through mucus.

8 REFERENCES

1. Finbloom, J. A.; Sousa, F.; Stevens, M. M.; Desai, T. A., Engineering the drug carrier biointerface to overcome biological barriers to drug delivery. *Advanced Drug Delivery Reviews* 2020, *167*, 89-108.

2. Corbo, C.; Molinaro, R.; Tabatabaei, M.; Farokhzad, O. C.; Mahmoudi, M., Personalized protein corona on nanoparticles and its clinical implications. *Biomaterials science* **2017,** *5* (3), 378-387.

3. Corbo, C.; Molinaro, R.; Parodi, A.; Toledano Furman, N. E.; Salvatore, F.; Tasciotti, E., The impact of nanoparticle protein corona on cytotoxicity, immunotoxicity and target drug delivery. *Nanomedicine* **2016,** *11* (1), 81-100.

4. Taherali, F.; Varum, F.; Basit, A. W., A slippery slope: On the origin, role and physiology of mucus. *Advanced Drug Delivery Reviews* **2018,** *124*, 16-33.

5. Cone, R., Mucus. Mucosal Immunology. San Diego: Academic Press: 1999.

6. Netschey, D. H. N. A., Studies of the Steric Stabilization of Colloidal Particles. *Journal of Colloid and Interface Science* **1971**.

7. Florin, E.; Kjellander, R.; Erikson, J. C., Salt Effects on the Cloud Point of the Poly(ethylene oxide)+Water System. *J. Chem. Soc., Faraday Trans. I* **1984,** *80*, 2889-2910.

8. Kjellander, R.; Florin, E., Water Structure and Changes in Thermal Stability of the System Poly(ethylene oxide)-Water. *J. Chem. Soc., Faraday Trans. I* **1981,** *77*, 2053-2077.

9. Taipaleenmäki, E.; Städler, B., Recent advancements in using polymers for intestinal mucoadhesion and mucopenetration. *Macromolecular Bioscience* **2020,** *20* (3), 1900342.

10. Taipaleenmäki, E. M.; Mouritzen, S. A.; Schattling, P. S.; Zhang, Y.; Städler, B., Mucopenetrating micelles with a PEG corona. *Nanoscale* **2017,** *9* (46), 18438-18448.

11. Gref, R.; Lück, M.; Quellec, P.; Marchand, M.; Dellacherie, E.; Harnisch, S.; Blunk, T.; Müller, R., 'Stealth'corona-core nanoparticles surface modified by polyethylene glycol (PEG): influences of the corona (PEG chain length and surface density) and of the core composition on phagocytic uptake and plasma protein adsorption. *Colloids and Surfaces B: Biointerfaces* **2000,** *18* (3-4), 301-313.

12. Webster, R.; Elliott, V.; Park, B. K.; Walker, D.; Hankin, M.; Taupin, P., PEG and PEG conjugates toxicity: towards an understanding of the toxicity of PEG and its relevance to PEGylated biologicals. *PEGylated protein drugs: Basic science and clinical applications* **2009**, 127-146.

13. Zhang, X.-D.; Di Wu, X. S.; Liu, P.-X.; Yang, N.; Zhao, B.; Zhang, H.; Sun, Y.-M.; Zhang, L.-A.; Fan, F.-Y., Size-dependent in vivo toxicity of PEG-coated gold nanoparticles. *International journal of nanomedicine* **2011,** *6*, 2071.

14. Chang, C.-J.; Chen, C.-H.; Chen, B.-M.; Su, Y.-C.; Chen, Y.-T.; Hershfield, M. S.; Lee, M.-T. M.; Cheng, T.-L.; Chen, Y.-T.; Roffler, S. R.; Wu, J.-Y., A genome-wide association study identifies a novel susceptibility locus for the immunogenicity of polyethylene glycol. *Nature Communications* **2017,** *8* (1), 522.

15. Schneck, E.; Berts, I.; Halperin, A.; Daillant, J.; Fragneto, G., Neutron reflectometry from poly (ethylene-glycol) brushes binding anti-PEG antibodies: Evidence of ternary adsorption. *Biomaterials* **2015,** *46*, 95-104.
16. Wang, Y. Y.; Lai, S. K.; Suk, J. S.; Pace, A.; Cone, R.; Hanes, J., Addressing the PEG mucoadhesivity paradox to engineer nanoparticles that "slip" through the human mucus barrier. *Angewandte Chemie* **2008,** *120* (50), 9872-9875.
17. Vaisocherová, H.; Yang, W.; Zhang, Z.; Cao, Z.; Cheng, G.; Piliarik, M.; Homola, J.; Jiang, S., Ultralow Fouling and Functionalizable Surface Chemistry Based on a Zwitterionic Polymer Enabling Sensitive and Specific Protein Detection in Undiluted Blood Plasma. *Analytical Chemistry* **2008,** *80* (20), 7894-7901.
18. Chen, M.; Briscoe, W. H.; Armes, S. P.; Cohen, H.; Klein, J., Polyzwitterionic brushes: Extreme lubrication by design. *European polymer journal* **2011,** *47* (4), 511-523.
19. de Grooth, J.; Ogieglo, W.; de Vos, W. M.; Gironès, M.; Nijmeijer, K.; Benes, N. E., Swelling dynamics of zwitterionic copolymers: The effects of concentration and type of anion and cation. *European polymer journal* **2014,** *55*, 57-65.
20. Zhang, Z.; Moxey, M.; Alswieleh, A.; Morse, A. J.; Lewis, A. L.; Geoghegan, M.; Leggett, G. J., Effect of Salt on Phosphorylcholine-based Zwitterionic Polymer Brushes. *Langmuir : the ACS journal of surfaces and colloids* **2016,** *32* (20), 5048-57.
21. Kobayashi, M.; Terayama, Y.; Yamaguchi, H.; Terada, M.; Murakami, D.; Ishihara, K.; Takahara, A., Wettability and antifouling behavior on the surfaces of superhydrophilic polymer brushes. *Langmuir : the ACS journal of surfaces and colloids* **2012,** *28* (18), 7212-7222.
22. Chen, X.; Qiu, X.; Hou, M.; Wu, X.; Dong, Y.; Ma, Y.; Yang, L.; Wei, Y., Differences in Zwitterionic Sulfobetaine and Carboxybetaine Dextran-Based Hydrogels. *Langmuir : the ACS journal of surfaces and colloids* **2019,** *35* (5), 1475-1482.
23. García, K. P.; Zarschler, K.; Barbaro, L.; Barreto, J. A.; O'Malley, W.; Spiccia, L.; Stephan, H.; Graham, B., Zwitterionic‐coated "stealth" nanoparticles for biomedical applications: recent advances in countering biomolecular corona formation and uptake by the mononuclear phagocyte system. *Small* **2014,** *10* (13), 2516-2529.
24. Schlenoff, J. B., Zwitteration: coating surfaces with zwitterionic functionality to reduce nonspecific adsorption. *Langmuir : the ACS journal of surfaces and colloids* **2014,** *30* (32), 9625-9636.
25. Cedervall, T.; Lynch, I.; Lindman, S.; Berggård, T.; Thulin, E.; Nilsson, H.; Dawson, K. A.; Linse, S., Understanding the nanoparticle–protein corona using methods to quantify exchange rates and affinities of proteins for nanoparticles. *Proceedings of the National Academy of Sciences* **2007,** *104* (7), 2050-2055.
26. Lundqvist, M., Nanoparticles: tracking protein corona over time. *Nature nanotechnology* **2013,** *8* (10), 701-702.
27. Lundqvist, M.; Stigler, J.; Cedervall, T.; Berggard, T.; Flanagan, M. B.; Lynch, I.; Elia, G.; Dawson, K., The evolution of the protein corona around nanoparticles: a test study. *ACS nano* **2011,** *5* (9), 7503-7509.

28. Efremova, N.; Huang, Y.; Peppas, N.; Leckband, D., Direct measurement of interactions between tethered poly (ethylene glycol) chains and adsorbed mucin layers. *Langmuir : the ACS journal of surfaces and colloids* **2002,** *18* (3), 836-845.
29. Deacon, M. P.; McGurk, S.; Roberts, C. J.; Williams, P. M.; Tendler, S. J. B.; Davies, M. C.; Davis, S. S.; Harding, S. E., Atomic force microscopy of gastric mucin and chitosan mucoadhesive systems. *Biochemical Journal* **2000,** *348* (3), 557-563.
30. Biggs, S.; Prieve, D. C.; Dagastine, R. R., Direct comparison of atomic force microscopic and total internal reflection microscopic measurements in the presence of nonadsorbing polyelectrolytes. *Langmuir : the ACS journal of surfaces and colloids* **2005,** *21* (12), 5421-5428.
31. Prieve, D. C., Measurement of colloidal forces with TIRM. *Advances in Colloid and Interface Science* **1999,** *82* (1-3), 93-125.
32. Napper, D. H., *Polymeric Stabilization of Colloidal Dispersions*. Academic Press: New York, 1983.
33. Russel, W. B.; Saville, D. A.; Schowalter, W. R., *Colloidal Dispersions*. Cambridge University Press: New York, 1989.
34. Everett, W. N.; Wu, H.-J.; Anekal, S. G.; Sue, H.-J.; Bevan, M. A., Diffusing colloidal probes of protein and synthetic macromolecule interactions. *Biophys. J.* **2007,** *92*, 1005-1013.
35. Eichmann, S. L.; Meric, G.; Swavola, J. C.; Bevan, M. A., Diffusing Colloidal Probes of Protein–Carbohydrate Interactions. *Langmuir* **2013,** *29* (7), 2299-2310.
36. Everett, W. N.; Bevan, M. A., kT-Scale interactions between supported lipid bilayers. *Soft Matter* **2014**.
37. Duncan, G. A.; Fairbrother, D. H.; Bevan, M. A., Diffusing colloidal probes of cell surfaces. *Soft Matter* **2016,** *12* (21), 4731-4738.
38. Swavola, J. C.; Edwards, T. D.; Bevan, M. A., Direct Measurement of Macromolecule-Coated Colloid–Mucus Interactions. *Langmuir* **2015,** *31* (33), 9076-9085.
39. Bevan, M. A.; Prieve, D. C., Forces and hydrodynamic interactions between polystyrene surfaces with adsorbed PEO-PPO-PEO. *Langmuir* **2000,** *16* (24), 9274-9281.
40. Fernandes, G. E.; Bevan, M. A., Equivalent Temperature and Specific Ion Effects in Macromolecule Coated Colloid Interactions. *Langmuir* **2007,** *23*, 1500-1506.
41. Najafi, H.; Jerri, H. A.; Valmacco, V.; Petroff, M. G.; Hansen, C.; Benczédi, D.; Bevan, M. A., Synergistic Polymer–Surfactant-Complex Mediated Colloidal Interactions and Deposition. *ACS Appl. Mat. Interfac.* **2020,** *12* (12), 14518-14530.
42. Petroff, M. G.; Garcia, E. A.; Dengler, R. A.; Herrera-Alonso, M.; Bevan, M. A., kT-Scale Interactions and Stability of Colloids with Adsorbed Zwitterionic and Ethylene Oxide Copolymers. *Macromolecules* **2018,** *51* (22), 9156-9164.
43. Langer, R.; Peppas, N. A., Advances in Biomaterials, Drug Delivery, and Bionanotechnology. *AIChE J.* **2003,** *49* (12), 2990-3006.
44. Zhulina, E. B.; Borisov, O. V.; Pryamitsyn, V. A.; Birshtein, T. M., Coil-Globule Type Transitions in Polymers. 1. Collapse of Layers of Grafted Polymer Chains. *Macromolecules* **1991,** *24*, 140.

45. Fleer, G. J.; Stuart, M. A. C.; Scheutjens, J. M. H. M.; Cosgrove, T.; Vincent, B., *Polymers at Interfaces*. Chapman & Hall: New York, 1993.
46. Bevan, M. A.; Prieve, D. C., Effect of Physisorbed Polymers on the Interaction of Latex Particles And Their Dispersion Stability. In *Polymers in Particulate Systems: Properties and Applications*, Hackley, V. A.; Somasundran, P.; Lewis, J. A., Eds. Marcel Dekker: New York, 2001; Vol. 104.
47. Napper, D. H., Steric Stabilization and the Hofmeister Series. *J. Colloid. Interface Sci.* **1969,** *33* (3), 384-392.
48. Hwang, K.; Wu, H.-J.; Bevan, M. A., Specific Ion-Dependent Attraction and Phase Behavior of Polymer-Coated Colloids. *Langmuir* **2004,** *20* (26), 11393-11401.
49. Collins, K. D.; Washabaugh, M. W., The Hofmeister effect and the behaviour of water at interfaces. *Quart. Rev. Biophys.* **1985,** *18*, 323-422.
50. Cacace, M. G.; Landau, E. M.; Ramsden, J. J., The Hofmeister series: salt and solvent effects on intefacial phenomena. *Quart. Rev. Biophys.* **1997,** *30* (3), 241-277.
51. Skolnick, J.; Fixman, M., Electrostatic Persistence Length of a Wormlike Polyelectrolyte. *Macromolecules* **1977,** *10* (5), 944-948.
52. Odijk, T., Polyelectrolytes near the rod limit. *Journal of Polymer Science: Polymer Physics Edition* **1977,** *15* (3), 477-483.
53. Kikuchi, M.; Terayama, Y.; Ishikawa, T.; Hoshino, T.; Kobayashi, M.; Ogawa, H.; Masunaga, H.; Koike, J. I.; Horigome, M.; Ishihara, K.; Takahara, A., Chain dimension of polyampholytes in solution and immobilized brush states. *Polymer Journal* **2012,** *44*, 121-130.
54. Higaki, Y.; Inutsuka, Y.; Sakamaki, T.; Terayama, Y.; Takenaka, A.; Higaki, K.; Yamada, N. L.; Moriwaki, T.; Ikemoto, Y.; Takahara, A., Effect of Charged Group Spacer Length on Hydration State in Zwitterionic Poly(sulfobetaine) Brushes. *Langmuir* **2017,** *33*, 8404-8412.
55. Weers, J. G.; Rathman, J. F.; Axe, F. U.; Crichlow, C. A.; Foland, L. D.; Scheuing, D. R.; Wiersema, R. J.; Zielske, A. G., Effect of the intramolecular charge separation distance on the solution properties of betaines and sulfobetaines. *Langmuir : the ACS journal of surfaces and colloids* **1991,** *7* (5), 854-867.
56. Kobayashi, M.; Ishihara, K.; Takahara, A., Neutron reflectivity study of the swollen structure of polyzwitterion and polyeletrolyte brushes in aqueous solution. *J. Biomat. Sci.* **2014,** *25*, 1673-1686.
57. Mary, P.; Bendejacq, D. D.; Labeau, M.-P.; Dupuis, P., Reconciling Low-and High-Salt Solution Behavior of Sulfobetaine Polyzwitterions. *J. Phys. Chem. B* **2007,** *111*, 7767-7777.
58. Kikuchi, M.; Terayama, Y.; Ishikawa, T.; Hoshino, T.; Kobayashi, M.; Ohta, N.; Jinnai, H.; Takahara, A., Salt Dependence of the Chain Stiffness and Excluded-Volume Strength for the Polymethacrylate-Type Sulfopropylbetaine in Aqueous NaCl Solutions. *Macromolecules* **2015,** *48*, 7194-7204.
59. Wang, F.; Yang, J.; Zhao, J., Understanding anti-polyelectrolyte behavior of a well-defined polyzwitterion at the single-chain level. *Polymer International* **2015,** *64* (8), 999-1005.

60. Kobayashi, M.; Terayama, Y.; Kikuchi, M.; Takahara, A., Chain dimensions and surface characterization of superhydrophilic polymer brushes with zwitterion side groups. *Soft Matter* **2013,** *9*, 5138.
61. Kato, T.; Takahashi, A., Excluded Volume Effects of Sulphobetaine Polymers. *Ber. Bunenges. Phys. Chem.* **1996,** *100*, 784-787.
62. Dong, Z.; Mao, J.; Yang, M.; Wang, D.; Bo, S.; Ji, X., Phase behavior of poly(sulfobetaine methacrylate)-grafted silica nanoparticles and their stability in protein solutions. *Langmuir* **2011,** *27*, 15282-15291.
63. Higgs, P. G.; Joanny, J. F., Theory of polyampholyte solutions. *J. Chem. Phys.* **1991,** *94* (2), 1543-1554.
64. Xiao, S.; Ren, B.; Huang, L.; Shen, M.; Zhang, Y.; Zhong, M.; Yang, J.; Zheng, J., Salt-responsive zwitterionic polymer brushes with anti-polyelectrolyte property. *Current Opinion in Chemical Engineering* **2018,** *19*, 86-93.
65. Petroff, M. G.; Garcia, E. A.; Herrera-Alonso, M.; Bevan, M. A., Ionic Strength-Dependent Interactions and Dimensions of Adsorbed Zwitterionic Copolymers. *Langmuir* **2019,** *35* (14), 4976-4985.
66. Delgado, J. D.; Schlenoff, J. B., Static and dynamic solution behavior of a polyzwitterion using a Hofmeister salt series. *Macromolecules* **2017,** *50* (11), 4454-4464.
67. Sakamaki, T.; Inutsuka, Y.; Igata, K.; Higaki, K.; Yamada, N. L.; Higaki, Y.; Takahara, A., Ion-Specific Hydration States of Zwitterionic Poly(sulfobetaine methacrylate) Brushes in Aqueous Solutions. *Langmuir : the ACS journal of surfaces and colloids* **2019,** *35* (5), 1583-1589.
68. Tairy, O.; Kampf, N.; Driver, M. J.; Armes, S. P.; Klein, J., Dense, highly hydrated polymer brushes via modified atom-transfer-radical-polymerization: structure, surface interactions, and frictional dissipation. *Macromolecules* **2015,** *48* (1), 140-151.
69. Chen, M.; Briscoe, W. H.; Armes, S. P.; Cohen, H.; Klein, J., Polyzwitterionic brushes: Extreme lubrication by design. *European Polym. J.* **2011,** *47* (4), 511-523.
70. Yang, J.; Chen, H.; Xiao, S.; Shen, M.; Chen, F.; Fan, P.; Zhong, M.; Zheng, J., Salt-Responsive Zwitterionic Polymer Brushes with Tunable Friction and Antifouling Properties. *Langmuir* **2015,** *31*, 9125-9133.
71. Inoue, Y.; Onodera, Y.; Ishihara, K., Preparation of a thick polymer brush layer composed of poly (2-methacryloyloxyethyl phosphorylcholine) by surface-initiated atom transfer radical polymerization and analysis of protein adsorption resistance. *Colloids and Surfaces B: Biointerfaces* **2016,** *141*, 507-512.
72. Estephan, Z. G.; Schlenoff, P. S.; Schlenoff, J. B., Zwitteration as an alternative to PEGylation. *Langmuir : the ACS journal of surfaces and colloids* **2011,** *27* (11), 6794-6800.
73. de Grooth, J.; Ogieglo, W.; de Vos, W. M.; Gironès, M.; Nijmeijer, K.; Benes, N. E., Swelling dynamics of zwitterionic copolymers: The effects of concentration and type of anion and cation. *European Polym, journal* **2014,** *55*, 57-65.
74. Sakota, K.; Tabata, D.; Sekiya, H., Macromolecular Crowding Modifies the Impact of Specific Hofmeister Ions on the Coil–Globule Transition of PNIPAM. *J. Phys. Chem. B* **2015,** *119* (32), 10334-10340.

75. Zhang, Y.; Furyk, S.; Bergbreiter, D. E.; Cremer, P. S., Specific Ion Effects on the Water Solubility of Macromolecules: PNIPAM and the Hofmeister Series. *J. Am. Chem. Soc.* **2005,** *127*, 14505-14510.
76. Narayanan Krishnamoorthy, A.; Holm, C.; Smiatek, J., Specific ion effects for polyelectrolytes in aqueous and non-aqueous media: the importance of the ion solvation behavior. *Soft Matter* **2018,** *14* (30), 6243-6255.
77. Wong, J. E.; Zastrow, H.; Jaeger, W.; von Klitzing, R., Specific Ion versus Electrostatic Effects on the Construction of Polyelectrolyte Multilayers. *Langmuir* **2009,** *25* (24), 14061-14070.
78. Bevan, M. A.; Prieve, D. C., Direct measurement of retarded van der Waals attraction. *Langmuir* **1999,** *15* (23), 7925-7936.
79. Dzyaloshinskii, I. E.; Lifshitz, E. M.; Pitaevskii, L. P., The general theory of van der Waals forces. *Adv. Phys.* **1961,** *10*, 165-209.
80. Prieve, D. C.; Russel, W. B., Simplified Predictions of Hamaker Constants from Lifshitz Theory. *J. Coll. Interfac. Sci.* **1988,** *125*, 1.
81. Bitter, J. L.; Duncan, G. A.; Beltran-Villegas, D. J.; Fairbrother, D. H.; Bevan, M. A., Anomalous Silica Colloid Stability and Gel Layer Mediated Interactions. *Langmuir* **2013,** *29* (28), 8835-8844.
82. Milner, S. T., Compressing Polymer Brushes - a Quantitative Comparison of Theory and Experiment. *Europhys. Lett.* **1988,** *7* (8), 695-699.
83. Shar, J. A.; Obey, T. M.; Cosgrove, T., Adsorption studies of polyethers Part 1. Adsorption onto hydrophobic surfaces. *Colloids and Surfaces A: Physicochemical and Engineering Aspects* **1998,** *136* (1), 21-33.
84. van Helden, A. K.; Jansen, J. W.; Vrij, A., Preparation and Characterization of Spherical Monodisperse Silica Dispersions in Non-Aqueous Solvents. *J. Coll. Interfac. Sci.* **1981,** *81* (2), 354-368.
85. Wu, H.-J.; Bevan, M. A., Direct Measurement of Single and Ensemble Average Particle-Surface Potential Energy Profiles. *Langmuir* **2005,** *21* (4), 1244-1254.
86. Prieve, D. C., Measurement of Colloidal Forces with TIRM. *Adv. Colloid Interface Sci.* **1999,** *82* (1-3), 93-125.
87. Chew, H.; Wang, D. S.; Kerker, M., Elastic Scattering of Evanescent Electromagnetic Waves. *Appl. Opt.* **1979,** *18*, 2679.
88. Coughlan, A. C. H.; Torres-Diaz, I.; Jerri, H. A.; Bevan, M. A., Direct Measurements of kT-Scale Capsule–Substrate Interactions and Deposition Versus Surfactants and Polymer Additives. *ACS Appl. Mat. Interfac.* **2018,** *10* (32), 27444-27453.
89. Dagastine, R. R.; Bevan, M. A.; White, L. R.; Prieve, D. C., Calculation of van der Waals forces with diffuse coatings: Applications to roughness and adsorbed polymers. *J. Adhesion* **2004,** *80* (5), 365-394.
90. Pedersen, J. S.; Sommer, C., Temperature dependence of the virial coefficients and the chi parameter in semi-dilute solutions of PEG. In *Scattering methods and the properties of polymer materials*, Springer: 2005; pp 70-78.

91. Marcus, Y., Thermodynamics of solvation of ions. Part 6.—The standard partial molar volumes of aqueous ions at 298.15 K. *J. Chem. Soc. Faraday Trans.* **1993,** *89* (4), 713-718.
92. Ayranci, E.; Sahin, M., Interactions of polyethylene glycols with water studied by measurements of density and sound velocity. *The Journal of Chemical Thermodynamics* **2008,** *40* (8), 1200-1207.
93. Yamaguchi, N.; Sato, M., Dipole moment of poly (ethylene oxide) in solution and its dependence on molecular weight and temperature. *Polymer journal* **2009,** *41* (8), 588-594.
94. Mathis, A.; Zheng, Y. L.; Galin, J. C., Random ethylacrylate zwitterionic copolymers: 3. Microphase separation as a function of the zwitterion structure. *Polymer* **1991,** *32*, 3080-3085.
95. Terayama, Y.; Arita, H.; Ishikawa, T.; Kikuchi, M.; Mitamura, K.; Kobayashi, M.; Yamada, N. L.; Takahara, A., Chain dimensions in free and immobilized brush states of polysulfobetaine in aqueous solution at various salt concentrations. *Journal of Physics: Conference Series* **2011,** *272*.
96. Ishihara, K.; Mu, M.; Konno, T.; Inoue, Y.; Fukazawa, K., The unique hydration state of poly(2-methacryloyloxyethyl phosphorylcholine). *J. Biomat. Sci.* **2017,** *28*, 884-899.
97. Mashaghi, A.; Partovi-Azar, P.; Jadidi, T.; Nafari, N.; Maass, P.; Tabar, M. R. R.; Bonn, M.; Bakker, H. J., Hydration strongly affects the molecular and electronic structure of membrane phospholipids. *J. Chem. Phys.* **2012,** *136*, 114709.
98. Morozova, S.; Hu, G.; Emrick, T.; Muthukumar, M., Influence of Dipole Orientation on Solution Properties of Polyzwitterions. *ACS Macro Letters* **2016,** *5*, 118-122.
99. Matsuda, Y.; Kobayashi, M.; Annaka, M.; Ishihara, K.; Takahara, A., UCST-Type Cononsolvency Behavior of Poly(2-methacryloxyethyl phosphorylcholine) in the Mixture of Water and Ethanol. *Polymer Journal* **2008,** *40* (5), 479-483.
100. Gunkel, G.; Huck, W. T., Cooperative adsorption of lipoprotein phospholipids, triglycerides, and cholesteryl esters are a key factor in nonspecific adsorption from blood plasma to antifouling polymer surfaces. *Journal of the American Chemical Society* **2013,** *135* (18), 7047-7052.
101. Monopoli, M. P.; Walczyk, D.; Campbell, A.; Elia, G.; Lynch, I.; Baldelli Bombelli, F.; Dawson, K. A., Physical− chemical aspects of protein corona: relevance to in vitro and in vivo biological impacts of nanoparticles. *Journal of the American Chemical Society* **2011,** *133* (8), 2525-2534.
102. Tenzer, S.; Docter, D.; Kuharev, J.; Musyanovych, A.; Fetz, V.; Hecht, R.; Schlenk, F.; Fischer, D.; Kiouptsi, K.; Reinhardt, C., Rapid formation of plasma protein corona critically affects nanoparticle pathophysiology. *Nature nanotechnology* **2013,** *8* (10), 772.
103. Giulimondi, F.; Digiacomo, L.; Pozzi, D.; Palchetti, S.; Vulpis, E.; Capriotti, A. L.; Chiozzi, R. Z.; Laganà, A.; Amenitsch, H.; Masuelli, L., Interplay of protein corona and immune cells controls blood residency of liposomes. *Nature communications* **2019,** *10* (1), 1-11.

104. Harris, J. M.; Chess, R. B., Effect of pegylation on pharmaceuticals. *Nature reviews Drug discovery* **2003,** *2* (3), 214-221.
105. Bevan, M. A.; Scales, P. J., Solvent Quality Dependent Interactions and Phase Behavior of Polystyrene Particles with Physisorbed PEO− PPO− PEO. *Langmuir : the ACS journal of surfaces and colloids* **2002,** *18* (5), 1474-1484.
106. Kjellander, R.; Florin, E., Water structure and changes in thermal stability of the system poly (ethylene oxide)–water. *Journal of the Chemical Society, Faraday Transactions 1: Physical Chemistry in Condensed Phases* **1981,** *77* (9), 2053-2077.
107. Florin, E.; Kjellander, R.; Eriksson, J. C., Salt effects on the cloud point of the poly (ethylene oxide)+ water system. *Journal of the Chemical Society, Faraday Transactions 1: Physical Chemistry in Condensed Phases* **1984,** *80* (11), 2889-2910.
108. Singh, R. L., J. W. Jr., Nanoparticle-based targeted drug delivery. *Experimental and molecular pathology* **2009,** *86* (3), 215-23.
109. Abbott, N. L.; Blankschtein, D.; Hatton, T. A., Protein partitioning in two-phase aqueous polymer systems. 1. Novel physical pictures and a scaling thermodynamic formulation. *Macromolecules* **1991,** *24* (15), 4334-4348.
110. Abbott, N. L.; Blankschtein, D.; Hatton, T. A., Protein partitioning in two-phase aqueous polymer systems. 2. On the free energy of mixing globular colloids and flexible polymers. *Macromolecules* **1992,** *25* (15), 3917-3931.
111. Abbott, N. L.; Blankschtein, D.; Hatton, T. A., Protein partitioning in two-phase aqueous polymer systems. 3. A neutron scattering investigation of the polymer solution structure and protein-polymer interactions. *Macromolecules* **1992,** *25* (15), 3932-3941.
112. Abbott, N. L.; Blankschtein, D.; Hatton, T. A., Protein partitioning in two-phase aqueous polymer systems. 4. Proteins in solutions of entangled polymers. *Macromolecules* **1992,** *25* (20), 5192-5200.
113. Topchieva, I.; Sorokina, E.; Efremova, N.; Ksenofontov, A., Noncovalent complexes between poly (ethylene glycol) and proteins. *Biochemistry. Biokhimiia* **1998,** *63* (11), 1312-1318.
114. Cleland, J. L.; Builder, S. E.; Swartz, J. R.; Winkler, M.; Chang, J. Y.; Wang, D. I., Polyethylene glycol enhanced protein refolding. *Bio/Technology* **1992,** *10* (9), 1013-1019.
115. Faulón Marruecos, D.; Saleh, L. S.; Kim, H. H.; Bryant, S. J.; Schwartz, D. K.; Kaar, J. L., Stabilization of fibronectin by random copolymer brushes inhibits macrophage activation. *ACS Applied Bio Materials* **2019,** *2* (11), 4698-4702.
116. Chao, S.-H.; Matthews, S. S.; Paxman, R.; Aksimentiev, A.; Gruebele, M.; Price, J. L., Two structural scenarios for protein stabilization by PEG. *The Journal of Physical Chemistry B* **2014,** *118* (28), 8388-8395.
117. Schöttler, S.; Becker, G.; Winzen, S.; Steinbach, T.; Mohr, K.; Landfester, K.; Mailänder, V.; Wurm, F. R., Protein adsorption is required for stealth effect of poly (ethylene glycol)-and poly (phosphoester)-coated nanocarriers. *Nature nanotechnology* **2016,** *11* (4), 372.
118. Riedel, T.; Riedelova-Reicheltova, Z.; Májek, P.; Rodriguez-Emmenegger, C.; Houska, M.; Dyr, J. E.; Brynda, E., Complete identification of proteins responsible for

human blood plasma fouling on poly (ethylene glycol)-based surfaces. *Langmuir : the ACS journal of surfaces and colloids* **2013,** *29* (10), 3388-3397.
119. Pinals, R. L.; Chio, L.; Ledesma, F.; Landry, M. P., Engineering at the nano-bio interface: harnessing the protein corona towards nanoparticle design and function. *Analyst* **2020,** *145* (15), 5090-5112.
120. Farruggia, B.; Nerli, B.; Di Nuci, H.; Rigatusso, R.; Picó, G., Thermal features of the bovine serum albumin unfolding by polyethylene glycols. *International journal of biological macromolecules* **1999,** *26* (1), 23-33.
121. Farruggia, B.; Nerli, B.; Picó, G., Study of the serum albumin-polyethyleneglycol interaction to predict the protein partitioning in aqueous two-phase systems. *Journal of Chromatography B* **2003,** *798* (1), 25-33.
122. Bosker, W.; Iakovlev, P.; Norde, W.; Stuart, M. C., BSA adsorption on bimodal PEO brushes. *Journal of colloid and interface science* **2005,** *286* (2), 496-503.
123. Currie, E.; Van der Gucht, J.; Borisov, O.; Stuart, M. C., Stuffed brushes: theory and experiment. *Pure and applied chemistry* **1999,** *71* (7), 1227-1241.
124. Norde, W.; Gage, D., Interaction of bovine serum albumin and human blood plasma with PEO-tethered surfaces: influence of PEO chain length, grafting density, and temperature. *Langmuir : the ACS journal of surfaces and colloids* **2004,** *20* (10), 4162-4167.
125. Halperin, A.; Fragneto, G.; Schollier, A.; Sferrazza, M., Primary versus ternary adsorption of proteins onto PEG brushes. *Langmuir : the ACS journal of surfaces and colloids* **2007,** *23* (21), 10603-10617.
126. Halperin, A.; Kroger, M., Ternary protein adsorption onto brushes: strong versus weak. *Langmuir : the ACS journal of surfaces and colloids* **2009,** *25* (19), 11621-11634.
127. Acuña, S. M.; Bastías, J. M.; Toledo, P. G., Direct measurement of interaction forces between bovine serum albumin and poly (ethylene oxide) in water and electrolyte solutions. *Plos one* **2017,** *12* (3), e0173910.
128. Del Pino, P.; Pelaz, B.; Zhang, Q.; Maffre, P.; Nienhaus, G. U.; Parak, W. J., Protein corona formation around nanoparticles–from the past to the future. *Materials Horizons* **2014,** *1* (3), 301-313.
129. Jedlovszky-Hajdu, A.; Bombelli, F. B.; Monopoli, M. P.; Tombacz, E.; Dawson, K. A., Surface coatings shape the protein corona of SPIONs with relevance to their application in vivo. *Langmuir : the ACS journal of surfaces and colloids* **2012,** *28* (42), 14983-14991.
130. Wang, X.; Berger, R.; Ramos, J. I.; Wang, T.; Koynov, K.; Liu, G.; Butt, H.-J.; Wu, S., Nanopatterns of polymer brushes for understanding protein adsorption on the nanoscale. *Rsc Advances* **2014,** *4* (85), 45059-45064.
131. Bevan, M. A.; Petris, S. N.; Chan, D. Y., Solvent quality dependent continuum van der Waals attraction and phase behavior for colloids bearing nonuniform adsorbed polymer layers. *Langmuir : the ACS journal of surfaces and colloids* **2002,** *18* (21), 7845-7852.
132. Halperin, A.; Zhulina, E., Stretching polymer brushes in poor solvents. *Macromolecules* **1991,** *24* (19), 5393-5397.
133. Wijmans, C.; Zhulina, E. B., Polymer brushes at curved surfaces. *Macromolecules* **1993,** *26* (26), 7214-7224.

134. Clark, P. L.; Plaxco, K. W.; Sosnick, T. R., Water as a good solvent for unfolded proteins: Folding and collapse are fundamentally different. *Journal of molecular biology* **2020,** *432* (9), 2882-2889.
135. Watanabe, H.; Tirrell, M., Measurement of forces in symmetric and asymmetric interactions between diblock copolymer layers adsorbed on mica. *Macromolecules* **1993,** *26* (24), 6455-6466.
136. Asakura, S.; Oosawa, F., On interaction between two bodies immersed in a solution of macromolecules. *The Journal of chemical physics* **1954,** *22* (7), 1255-1256.
137. Vrij, A., Pure Appl. Chem: 1976.
138. De Gennes, P. d., Polymer solutions near an interface. Adsorption and depletion layers. *Macromolecules* **1981,** *14* (6), 1637-1644.
139. De Gennes, P. G., Polymers at an interface. 2. Interaction between two plates carrying adsorbed polymer layers. *Macromolecules* **1982,** *15* (2), 492-500.
140. Lekkerkerker, H. N.; Tuinier, R., Depletion interaction. In *Colloids and the depletion interaction*, Springer: 2011; pp 57-108.
141. Vilker, V. L.; Colton, C. K.; Smith, K. A., The osmotic pressure of concentrated protein solutions: effect of concentration and pH in saline solutions of bovine serum albumin. *Journal of Colloid and Interface Science* **1981,** *79* (2), 548-566.
142. Yousef, M.; Datta, R.; Rodgers, V., Free-solvent model of osmotic pressure revisited: application to concentrated IgG solution under physiological conditions. *Journal of colloid and interface science* **1998,** *197* (1), 108-118.
143. Smilgies, D.-M.; Folta-Stogniew, E., Molecular weight-gyration radius relation of globular proteins: a comparison of light scattering, small-angle X-ray scattering and structure-based data. *J Appl Crystallogr* **2015,** *48* (Pt 5), 1604-1606.
144. Vivares, D.; Belloni, L.; Tardieu, A.; Bonnete, F., Catching the PEG-induced attractive interaction between proteins. *The European Physical Journal E* **2002,** *9* (1), 15-25.
145. Tardieu, A.; Bonneté, F.; Finet, S.; Vivares, D., Understanding salt or PEG induced attractive interactions to crystallize biological macromolecules. *Acta Crystallographica Section D: Biological Crystallography* **2002,** *58* (10), 1549-1553.
146. McPherson Jr, A., Crystallization of proteins from polyethylene glycol. *Journal of Biological Chemistry* **1976,** *251* (20), 6300-6303.
147. Kulkarni, A. M.; Chatterjee, A. P.; Schweizer, K. S.; Zukoski, C. F., Effects of polyethylene glycol on protein interactions. *The Journal of chemical physics* **2000,** *113* (21), 9863-9873.
148. Halperin, A.; Kroger, M.; Zhulina, E., Colloid-brush interactions: The effect of solvent quality. *Macromolecules* **2011,** *44* (9), 3622-3638.
149. Jumai'an, E.; Garcia, E.; Herrera-Alonso, M.; Bevan, M. A., Specific Ion Effects on Adsorbed Zwitterionic Copolymers. *Macromolecules* **2020,** *53* (22), 9769-9778.
150. Edwards, T. D.; Bevan, M. A., Depletion-Mediated Potentials and Phase Behavior for Micelles, Macromolecules, Nanoparticles, and Hydrogel Particles. *Langmuir : the ACS journal of surfaces and colloids* **2012,** *28* (39), 13816-13823.
151. De Gennes, P. d., *Scaling concepts in polymer physics*. 1979.

152. Dobrovolskaia, M. A.; McNeil, S. E., Immunological properties of engineered nanomaterials. *Nanoscience And Technology: A Collection of Reviews from Nature Journals* **2010**, 278-287.
153. Dobrovolskaia, M. A.; Germolec, D. R.; Weaver, J. L., Evaluation of nanoparticle immunotoxicity. *Nature Nanotechnology* **2009,** *4* (7), 411-414.
154. Dobrovolskaia, M. A.; Aggarwal, P.; Hall, J. B.; McNeil, S. E., Preclinical studies to understand nanoparticle interaction with the immune system and its potential effects on nanoparticle biodistribution. *Molecular pharmaceutics* **2008,** *5* (4), 487-495.
155. Owens III, D. E.; Peppas, N. A., Opsonization, biodistribution, and pharmacokinetics of polymeric nanoparticles. *International journal of pharmaceutics* **2006,** *307* (1), 93-102.
156. Frank, M. M.; Fries, L. F., The role of complement in inflammation and phagocytosis. *Immunology today* **1991,** *12* (9), 322-326.
157. Peracchia, M.; Harnisch, S.; Pinto-Alphandary, H.; Gulik, A.; Dedieu, J.; Desmaele, D.; d'Angelo, J.; Müller, R.; Couvreur, P., Visualization of in vitro protein-rejecting properties of PEGylated stealth® polycyanoacrylate nanoparticles. *Biomaterials* **1999,** *20* (14), 1269-1275.
158. Ngadi, N.; Abrahamson, J.; Fee, C.; Morison, K., Are PEG molecules a universal protein repellent. *Int. J. Biol. Life Sci* **2009,** *1* (3), 116-120.
159. Ahmed, S. T.; Leckband, D. E., Protein adsorption on grafted zwitterionic polymers depends on chain density and molecular weight. *Advanced Functional Materials* **2020,** *30* (30), 2000757.
160. Higaki, Y.; Kobayashi, M.; Murakami, D.; Takahara, A., Anti-fouling behavior of polymer brush immobilized surfaces. *Polymer Journal* **2016,** *48* (4), 325-331.
161. Chen, S.; Zheng, J.; Li, L.; Jiang, S., Strong resistance of phosphorylcholine self-assembled monolayers to protein adsorption: insights into nonfouling properties of zwitterionic materials. *Journal of the American Chemical Society* **2005,** *127* (41), 14473-14478.
162. Schönemann, E.; Laschewsky, A.; Wischerhoff, E.; Koc, J.; Rosenhahn, A., Surface modification by polyzwitterions of the sulfabetaine-type, and their resistance to biofouling. *Polymers* **2019,** *11* (6), 1014.
163. Schönemann, E.; Koc, J.; Aldred, N.; Clare, A. S.; Laschewsky, A.; Rosenhahn, A.; Wischerhoff, E., Synthesis of novel sulfobetaine polymers with differing dipole orientations in their side chains, and their effects on the antifouling properties. *Macromolecular rapid communications* **2020,** *41* (1), 1900447.
164. Kisley, L.; Miller, K. A.; Davis, C. M.; Guin, D.; Murphy, E. A.; Gruebele, M.; Leckband, D. E., Soluble zwitterionic poly (sulfobetaine) destabilizes proteins. *Biomacromolecules* **2018,** *19* (9), 3894-3901.
165. Yang, W.; Chen, S.; Cheng, G.; Vaisocherova, H.; Xue, H.; Li, W.; Zhang, J.; Jiang, S., Film thickness dependence of protein adsorption from blood serum and plasma onto poly (sulfobetaine)-grafted surfaces. *Langmuir : the ACS journal of surfaces and colloids* **2008,** *24* (17), 9211-9214.
166. Yoshimoto, K.; Hirase, T.; Madsen, J.; Armes, S. P.; Nagasaki, Y., Non‐fouling character of poly [2‐(methacryloyloxy) ethyl phosphorylcholine]‐modified gold

surfaces fabricated by the ‘grafting to’ method: Comparison of its protein resistance with poly (ethylene glycol) - modified gold surfaces. *Macromolecular rapid communications* **2009,** *30* (24), 2136-2140.
167. Fukuhara, Y.; Kyuzo, M.; Tsutsumi, Y.; Nagai, A.; Chen, P.; Hanawa, T., The effect of different component ratios in block polymers and processing conditions on electrodeposition efficiency onto titanium. *Applied Surface Science* **2015,** *355*, 784-791.
168. Leckband, D.; Sheth, S.; Halperin, A., Grafted poly (ethylene oxide) brushes as nonfouling surface coatings. *Journal of Biomaterials Science, Polymer Edition* **1999,** *10* (10), 1125-1147.
169. Szleifer, I., Protein adsorption on surfaces with grafted polymers: a theoretical approach. *Biophysical journal* **1997,** *72* (2), 595-612.
170. Jiang, S.; Cao, Z., Ultralow - fouling, functionalizable, and hydrolyzable zwitterionic materials and their derivatives for biological applications. *Advanced materials* **2010,** *22* (9), 920-932.
171. Wu, J.-J.; Zhou, J.; Rong, J.-Q.; Lu, Y.; Dong, H.; Yu, H.-Y.; Gu, J.-S., Grafting branch length and density dependent performance of zwitterionic polymer decorated polypropylene membrane. *Chinese Journal of Polymer Science* **2018,** *36* (4), 528-535.
172. He, M.; Gao, K.; Zhou, L.; Jiao, Z.; Wu, M.; Cao, J.; You, X.; Cai, Z.; Su, Y.; Jiang, Z., Zwitterionic materials for antifouling membrane surface construction. *Acta biomaterialia* **2016,** *40*, 142-152.
173. Li, Q.; Imbrogno, J.; Belfort, G.; Wang, X. L., Making polymeric membranes antifouling via “grafting from” polymerization of zwitterions. *Journal of Applied Polymer Science* **2015,** *132* (21).
174. Liu, P.-S.; Chen, Q.; Wu, S.-S.; Shen, J.; Lin, S.-C., Surface modification of cellulose membranes with zwitterionic polymers for resistance to protein adsorption and platelet adhesion. *Journal of Membrane Science* **2010,** *350* (1-2), 387-394.
175. Chang, Y.; Shih, Y.-J.; Lai, C.-J.; Kung, H.-H.; Jiang, S., Blood-Inert Surfaces via Ion-Pair Anchoring of Zwitterionic Copolymer Brushes in Human Whole Blood. *Advanced Functional Materials* **2013,** *23* (9), 1100-1110.
176. Kalasin, S.; Letteri, R. A.; Emrick, T.; Santore, M. M., Adsorbed Polyzwitterion Copolymer Layers Designed for Protein Repellency and Interfacial Retention. *Langmuir : the ACS journal of surfaces and colloids* **2017,** *33* (47), 13708-13717.
177. Wang, S.-Y.; Fang, L.-F.; Cheng, L.; Jeon, S.; Kato, N.; Matsuyama, H., Improved antifouling properties of membranes by simple introduction of zwitterionic copolymers via electrostatic adsorption. *Journal of Membrane Science* **2018,** *564*, 672-681.
178. Wang, S.-Y.; Fang, L.-F.; Matsuyama, H., Construction of a stable zwitterionic layer on negatively-charged membrane via surface adsorption and cross-linking. *Journal of Membrane Science* **2020,** *597*, 117766.
179. Sharma, S.; Johnson, R. W.; Desai, T. A., XPS and AFM analysis of antifouling PEG interfaces for microfabricated silicon biosensors. *Biosensors and Bioelectronics* **2004,** *20* (2), 227-239.

180. Adibnia, V.; Olszewski, M.; De Crescenzo, G.; Matyjaszewski, K.; Banquy, X., Superlubricity of Zwitterionic Bottlebrush Polymers in the Presence of Multivalent Ions. *Journal of the American Chemical Society* **2020,** *142* (35), 14843-14847.
181. Vroman, L.; Adams, A.; Fischer, G.; Munoz, P., Interaction of high molecular weight kininogen, factor XII, and fibrinogen in plasma at interfaces. **1980**.
182. Dijt, J. C.; Cohen Stuart, M. A.; Fleer, G. J., Competitive Adsorption Kinetics of Polymers Differing in Length Only. *Macromolecules* **1994,** *27* (12), 3219-3228.
183. Dijt, J. C.; Cohen Stuart, M. A.; Fleer, G. J., Surface Exchange Kinetics of Chemically Different Polymers. *Macromolecules* **1994,** *27* (12), 3229-3237.
184. Fleer, G.; Scheutjens, J., Adsorption of interacting oligomers and polymers at an interface. *Advances in Colloid and Interface Science* **1982,** *16* (1), 341-359.
185. Kolthoff, I. M.; Gutmacher, R. G., Sorption of GR-S Type of Polymer on Carbon Black. III. Sorption by Commercial Blacks. *The Journal of Physical Chemistry* **1952,** *56* (6), 740-745.
186. Johnson, H. E.; Granick, S., New Mechanism of Nonequilibrium Polymer Adsorption. *Science* **1992,** *255* (5047), 966-968.
187. Enriquez, E. P.; Schneider, H. M.; Granick, S., PMMA adsorption over previously adsorbed PS studied by polarized FTIR-ATR. *Journal of Polymer Science Part B: Polymer Physics* **1995,** *33* (17), 2429-2437.
188. Thies, C., The Adsorption of Polystyrene-Poly(methyl methacrylate) Mixtures at a Solid-Liquid Interface1. *The Journal of Physical Chemistry* **1966,** *70* (12), 3783-3790.
189. Dhoot, S.; Tirrell, M., Competitive adsorption of binary mixtures of diblock copolymers onto solid substrates. *Macromolecules* **1995,** *28* (10), 3692-3701.
190. Santore, M.; Fu, Z., Direct measurement of molecular-weight driven competition during polymer adsorption. *Macromolecules* **1997,** *30* (26), 8516-8517.
191. Fu, Z.; Santore, M. M., Kinetics of competitive adsorption of PEO chains with different molecular weights. *Macromolecules* **1998,** *31* (20), 7014-7022.
192. Dijt, J. C., *Kinetics of polymer adsorption, desorption and exchange*. Wageningen University and Research: 1993.
193. Van der Beek, G., *Displacement of Adsorbed Polymers: A Systematic Study of Segment–Surface Interactions*. Wageningen University and Research: 1991.
194. Fu, Z.; Santore, M. M., Competitive Adsorption of Poly(ethylene oxide) Chains with and without Charged End Groups. *Langmuir : the ACS journal of surfaces and colloids* **1998,** *14* (15), 4300-4307.
195. Fleer, G., Multicomponent polymer adsorption A useful approximation based upon ground-state solutions. *Colloids and Surfaces A: Physicochemical and Engineering Aspects* **1995,** *104* (2-3), 271-284.
196. Pagac, E. S.; Prieve, D. C.; Tilton, R. D., Kinetics and mechanism of cationic surfactant adsorption and coadsorption with cationic polyelectrolytes at the silica− water interface. *Langmuir : the ACS journal of surfaces and colloids* **1998,** *14* (9), 2333-2342.
197. Kusumo, A.; Bombalski, L.; Lin, Q.; Matyjaszewski, K.; Schneider, J. W.; Tilton, R. D., High capacity, charge-selective protein uptake by polyelectrolyte brushes. *Langmuir : the ACS journal of surfaces and colloids* **2007,** *23* (8), 4448-4454.

198. Tran, Y.; Auroy, P.; Lee, L.; Stamm, M., Polyelectrolyte brushes: Counterion distribution and complexation properties. *Physical Review E* **1999,** *60* (6), 6984.
199. Ishihara, K.; Nomura, H.; Mihara, T.; Kurita, K.; Iwasaki, Y.; Nakabayashi, N., Why do phospholipid polymers reduce protein adsorption? *Journal of Biomedical Materials Research: An Official Journal of The Society for Biomaterials, The Japanese Society for Biomaterials, and the Australian Society for Biomaterials* **1998,** *39* (2), 323-330.
200. Stuart, M. C.; Fleer, G., Adsorbed polymer layers in nonequilibrium situations. *Annual review of materials science* **1996,** *26* (1), 463-500.
201. Bansil, R.; Turner, B. S., Mucin structure, aggregation, physiological functions and biomedical applications. *Current opinion in colloid & interface science* **2006,** *11* (2-3), 164-170.
202. Bansil, R.; Turner, B. S., The biology of mucus: Composition, synthesis and organization. *Advanced drug delivery reviews* **2018,** *124*, 3-15.
203. Lieleg, O.; Ribbeck, K., Biological hydrogels as selective diffusion barriers. *Trends in cell biology* **2011,** *21* (9), 543-551.
204. Song, D.; Iverson, E.; Kaler, L.; Bader, S.; Scull, M. A.; Duncan, G. A., Modeling Airway Dysfunction in Asthma Using Synthetic Mucus Biomaterials. *ACS Biomaterials Science & Engineering* **2021,** *7* (6), 2723-2733.
205. Lai, S. K.; Wang, Y.-Y.; Wirtz, D.; Hanes, J., Micro- and macrorheology of mucus. *Advanced Drug Delivery Reviews* **2009,** *61* (2), 86-100.
206. Zappone, B.; Patil, N. J.; Madsen, J. B.; Pakkanen, K. I.; Lee, S., Molecular Structure and Equilibrium Forces of Bovine Submaxillary Mucin Adsorbed at a Solid–Liquid Interface. *Langmuir : the ACS journal of surfaces and colloids* **2015,** *31* (15), 4524-4533.
207. Thornton, D. J.; Rousseau, K.; McGuckin, M. A., Structure and function of the polymeric mucins in airways mucus. *Annu. Rev. Physiol.* **2008,** *70*, 459-486.
208. Leal, J.; Smyth, H. D.; Ghosh, D., Physicochemical properties of mucus and their impact on transmucosal drug delivery. *International journal of pharmaceutics* **2017,** *532* (1), 555-572.
209. Schattling, P.; Taipaleenmäki, E.; Zhang, Y.; Städler, B., A polymer chemistry point of view on mucoadhesion and mucopenetration. *Macromolecular bioscience* **2017,** *17* (9), 1700060.
210. Schuster, B. S.; Suk, J. S.; Woodworth, G. F.; Hanes, J., Nanoparticle diffusion in respiratory mucus from humans without lung disease. *Biomaterials* **2013,** *34* (13), 3439-3446.
211. Khanvilkar, K.; Donovan, M. D.; Flanagan, D. R., Drug transfer through mucus. *Advanced drug delivery reviews* **2001,** *48* (2-3), 173-193.
212. Cone, R. A., Barrier properties of mucus. *Advanced drug delivery reviews* **2009,** *61* (2), 75-85.
213. Lai, S. K.; O'Hanlon, D. E.; Harrold, S.; Man, S. T.; Wang, Y.-Y.; Cone, R.; Hanes, J., Rapid transport of large polymeric nanoparticles in fresh undiluted human mucus. *Proceedings of the National Academy of Sciences* **2007,** *104* (5), 1482-1487.

214. Curnutt, A.; Smith, K.; Darrow, E.; Walters, K. B., Chemical and Microstructural Characterization of pH and [Ca 2+] Dependent Sol-Gel Transitions in Mucin Biopolymer. *Scientific Reports* **2020,** *10* (1), 1-12.
215. Crowther, R.; Marriott, C.; James, S., Cation induced changes in the rheological properties of purified mucus glycoprotein gels. *Biorheology* **1984,** *21* (1-2), 253-263.
216. Meldrum, O. W.; Yakubov, G. E.; Bonilla, M. R.; Deshmukh, O.; McGuckin, M. A.; Gidley, M. J., Mucin gel assembly is controlled by a collective action of non-mucin proteins, disulfide bridges, Ca2+-mediated links, and hydrogen bonding. *Scientific Reports* **2018,** *8* (1), 1-16.
217. Espinosa, M.; Noe, G.; Troncoso, C.; Ho, S.; Villalon, M., Acidic pH and increasing [Ca2+] reduce the swelling of mucins in primary cultures of human cervical cells. *Human Reproduction* **2002,** *17* (8), 1964-1972.
218. Hughes, G. W.; Ridley, C.; Collins, R.; Roseman, A.; Ford, R.; Thornton, D. J., The MUC5B mucin polymer is dominated by repeating structural motifs and its topology is regulated by calcium and pH. *Scientific Reports* **2019,** *9* (1), 17350.
219. McNiff, E.; Clemente, E.; Fung, H.-L., In-Vitro Comparison of the Mucolytic Activity of Sodium Metabisulfite, N-Acetylcysteine and Dithiothreitol. *Drug Development Communications* **1974,** *1* (6), 507-516.
220. Khan, M.; Wolf, D.; Litt, M., Effect of mucolytic agents on the rheological properties of tracheal mucos. *Biochimica et Biophysica Acta (BBA)-General Subjects* **1976,** *444* (2), 369-373.
221. Poole, P.; Black, P. N.; Cates, C. J., Mucolytic agents for chronic bronchitis or chronic obstructive pulmonary disease. *Cochrane Database of systematic reviews* **2012,** (8).
222. Rogers, D. F., Mucoactive agents for airway mucus hypersecretory diseases. *Respiratory Care* **2007,** *52* (9), 1176-1197.
223. Wagner, C. E.; Wheeler, K. M.; Ribbeck, K., Mucins and Their Role in Shaping the Functions of Mucus Barriers. *Annual Review of Cell and Developmental Biology* **2018,** *34* (1), 189-215.
224. Yuan, S.; Hollinger, M.; Lachowicz-Scroggins, M. E.; Kerr, S. C.; Dunican, E. M.; Daniel, B. M.; Ghosh, S.; Erzurum, S. C.; Willard, B.; Hazen, S. L., Oxidation increases mucin polymer cross-links to stiffen airway mucus gels. *Science translational medicine* **2015,** *7* (276), 276ra27-276ra27.
225. Peppas, N. A.; Huang, Y., Nanoscale technology of mucoadhesive interactions. *Advanced drug delivery reviews* **2004,** *56* (11), 1675-1687.
226. Bechinger, C.; Di Leonardo, R.; Löwen, H.; Reichhardt, C.; Volpe, G.; Volpe, G., Active Brownian particles in complex and crowded environments. *Rev. Mod. Phys*.
227. Crater, J. S.; Carrier, R. L., Barrier properties of gastrointestinal mucus to nanoparticle transport. *Macromolecular bioscience* **2010,** *10* (12), 1473-1483.
228. Zhang, X.; Hansing, J.; Netz, R. R.; DeRouchey, J. E., Particle transport through hydrogels is charge asymmetric. *Biophysical journal* **2015,** *108* (3), 530-539.
229. Rossi, S.; Vigani, B.; Sandri, G.; Bonferoni, M. C.; Caramella, C. M.; Ferrari, F., Recent advances in the mucus-interacting approach for vaginal drug delivery: From

mucoadhesive to mucus-penetrating nanoparticles. *Expert Opinion on Drug Delivery* **2019,** *16* (8), 777-781.
230. Rossi, S.; Vigani, B.; Bonferoni, M. C.; Sandri, G.; Caramella, C.; Ferrari, F., Rheological analysis and mucoadhesion: A 30 year-old and still active combination. *Journal of Pharmaceutical and Biomedical Analysis* **2018,** *156*, 232-238.
231. Tong, J.; Anderson, J. L., Partitioning and diffusion of proteins and linear polymers in polyacrylamide gels. *Biophysical journal* **1996,** *70* (3), 1505-1513.
232. Bevan, M. A.; Prieve, D. C., Hindered diffusion of colloidal particles very near to a wall: Revisited. *The Journal of chemical physics* **2000,** *113* (3), 1228-1236.
233. Merrill, E. W.; Dennison, K. A.; Sung, C., Partitioning and diffusion of solutes in hydrogels of poly (ethylene oxide). *Biomaterials* **1993,** *14* (15), 1117-1126.
234. Marczynski, M.; Käsdorf, B. T.; Altaner, B.; Wenzler, A.; Gerland, U.; Lieleg, O., Transient binding promotes molecule penetration into mucin hydrogels by enhancing molecular partitioning. *Biomaterials science* **2018,** *6* (12), 3373-3387.
235. Mitragotri, S.; Johnson, M. E.; Blankschtein, D.; Langer, R., An analysis of the size selectivity of solute partitioning, diffusion, and permeation across lipid bilayers. *Biophysical journal* **1999,** *77* (3), 1268-1283.
236. Dursch, T. J.; Taylor, N. O.; Liu, D. E.; Wu, R. Y.; Prausnitz, J. M.; Radke, C. J., Water-soluble drug partitioning and adsorption in HEMA/MAA hydrogels. *Biomaterials* **2014,** *35* (2), 620-629.
237. Liu, D. E. Solute Partitioning and Hindered Diffusion in Hydrogels. UC Berkeley, 2016.
238. Knop, K.; Hoogenboom, R.; Fischer, D.; Schubert, U. S., Poly (ethylene glycol) in drug delivery: pros and cons as well as potential alternatives. *Angewandte chemie international edition* **2010,** *49* (36), 6288-6308.
239. Maisel, K.; Reddy, M.; Xu, Q.; Chattopadhyay, S.; Cone, R.; Ensign, L. M.; Hanes, J., Nanoparticles coated with high molecular weight PEG penetrate mucus and provide uniform vaginal and colorectal distribution in vivo. *Nanomedicine* **2016,** *11* (11), 1337-1343.
240. Huckaby, J. T.; Lai, S. K., PEGylation for enhancing nanoparticle diffusion in mucus. *Advanced drug delivery reviews* **2018,** *124*, 125-139.
241. Olmsted, S. S.; Padgett, J. L.; Yudin, A. I.; Whaley, K. J.; Moench, T. R.; Cone, R. A., Diffusion of macromolecules and virus-like particles in human cervical mucus. *Biophysical journal* **2001,** *81* (4), 1930-1937.
242. Wang, Y. Y.; Lai, S. K.; Suk, J. S.; Pace, A.; Cone, R.; Hanes, J., Addressing the PEG mucoadhesivity paradox to engineer nanoparticles that "slip" through the human mucus barrier. *Angewandte Chemie International Edition* **2008,** *47* (50), 9726-9729.
243. Huang, Y. B.; Leobandung, W.; Foss, A.; Peppas, N. A., Molecular aspects of muco- and bioadhesion: Tethered structures and site-specific surfaces. *JOURNAL OF CONTROLLED RELEASE* **2000,** *65* (1-2), 63-71.
244. Sahlin, J. J.; Peppas, N. A., Enhanced hydrogel adhesion by polymer interdiffusion: Use of linear poly(ethylene glycol) as an adhesion promoter. *JOURNAL OF BIOMATERIALS SCIENCE-POLYMER EDITION* **1997,** *8* (6), 421-436.

245. De Ascentiis, A.; deGrazia, J. L.; Bowman, C. N.; Colombo, P.; Peppas, N. A., Mucoadhesion of poly (2-hydroxyethyl methacrylate) is improved when linear poly (ethylene oxide) chains are added to the polymer network. *Journal of controlled release* **1995,** *33* (1), 197-201.
246. Yoncheva, K.; Gómez, S.; Campanero, M. A.; Gamazo, C.; Irache, J. M., Bioadhesive properties of pegylated nanoparticles. *Expert opinion on drug delivery* **2005,** *2* (2), 205-218.
247. Bures, P.; Huang, Y.; Oral, E.; Peppas, N. A., Surface modifications and molecular imprinting of polymers in medical and pharmaceutical applications. *Journal of Controlled Release* **2001,** *72* (1-3), 25-33.
248. Wu, H.-J.; Bevan, M. A., Direct measurement of single and ensemble average particle− surface potential energy profiles. *Langmuir : the ACS journal of surfaces and colloids* **2005,** *21* (4), 1244-1254.
249. Taipaleenmäki, E.; Brodszkij, E.; Städler, B., Mucopenetrating Zwitterionic Micelles. *ChemNanoMat* **2020,** *6* (5), 744-750.
250. Lai, S. K.; Wang, Y.-Y.; Wirtz, D.; Hanes, J., Micro-and macrorheology of mucus. *Advanced drug delivery reviews* **2009,** *61* (2), 86-100.
251. Lai, S. K.; Wang, Y.-Y.; Hanes, J., Mucus-penetrating nanoparticles for drug and gene delivery to mucosal tissues. *Advanced drug delivery reviews* **2009,** *61* (2), 158-171.
252. Yu, M.; Wang, J.; Yang, Y.; Zhu, C.; Su, Q.; Guo, S.; Sun, J.; Gan, Y.; Shi, X.; Gao, H., Rotation-Facilitated Rapid Transport of Nanorods in Mucosal Tissues. *Nano Letters* **2016,** *16* (11), 7176-7182.
253. Bhattacharjee, S., DLS and zeta potential–what they are and what they are not? *Journal of controlled release* **2016,** *235*, 337-351.
254. Curnutt, A.; Smith, K.; Darrow, E.; Walters, K. B.; Vasquez, E. S.; Kundu, S. In *Physicochemical Characterization of Mammalian Mucus and Mucin Solutions in Response to pH and [Ca2+]*, Fluids Engineering Division Summer Meeting, American Society of Mechanical Engineers: 2019; p V004T06A016.
255. Georgiades, P.; Pudney, P. D.; Thornton, D. J.; Waigh, T. A., Particle tracking microrheology of purified gastrointestinal mucins. *Biopolymers* **2014,** *101* (4), 366-377.
256. Wang, Y.-Y.; Lai, S. K.; Ensign, L. M.; Zhong, W.; Cone, R.; Hanes, J., The Microstructure and Bulk Rheology of Human Cervicovaginal Mucus Are Remarkably Resistant to Changes in pH. *Biomacromolecules* **2013,** *14* (12), 4429-4435.
257. Harvey, N. M.; Yakubov, G. E.; Stokes, J. R.; Klein, J., Normal and Shear Forces between Surfaces Bearing Porcine Gastric Mucin, a High-Molecular-Weight Glycoprotein. *Biomacromolecules* **2011,** *12* (4), 1041-1050.
258. Iijima, M.; Yoshimura, M.; Tsuchiya, T.; Tsukada, M.; Ichikawa, H.; Fukumori, Y.; Kamiya, H., Direct Measurement of Interactions between Stimulation-Responsive Drug Delivery Vehicles and Artificial Mucin Layers by Colloid Probe Atomic Force Microscopy. *Langmuir : the ACS journal of surfaces and colloids* **2008,** *24* (8), 3987-3992.
259. Cleary, J.; Bromberg, L.; Magner, E., Adhesion of polyether-modified poly (acrylic acid) to mucin. *Langmuir : the ACS journal of surfaces and colloids* **2004,** *20* (22), 9755-9762.

260. Prieve, D. C.; Frej, N. A., Total internal reflection microscopy: a quantitative tool for the measurement of colloidal forces. *Langmuir : the ACS journal of surfaces and colloids* **1990,** *6* (2), 396-403.
261. Alexandridis, P.; Hatton, T. A., Poly (ethylene oxide) · poly (propylene oxide) · poly (ethylene oxide) block copolymer surfactants in aqueous solutions and at interfaces: thermodynamics, structure, dynamics, and modeling. *Colloids and Surfaces A: Physicochemical and Engineering Aspects* **1995,** *96* (1-2), 1-46.
262. Alexandridis, P.; Holzwarth, J. F.; Hatton, T. A., Micellization of poly (ethylene oxide)-poly (propylene oxide)-poly (ethylene oxide) triblock copolymers in aqueous solutions: thermodynamics of copolymer association. *Macromolecules* **1994,** *27* (9), 2414-2425.
263. Eichmann, S. L.; Meric, G.; Swavola, J. C.; Bevan, M. A., Diffusing colloidal probes of protein-carbohydrate interactions. *Langmuir : the ACS journal of surfaces and colloids* **2013,** *29*, 2299-310.
264. Najafi, H.; Jerri, H. A.; Valmacco, V.; Petroff, M. G.; Hansen, C.; Benczedi, D.; Bevan, M. A., Synergistic polymer–surfactant-complex mediated colloidal interactions and deposition. *ACS Applied Materials & Interfaces* **2020,** *12* (12), 14518-14530.
265. Celli Jonathan, P.; Turner Bradley, S.; Afdhal Nezam, H.; Keates, S.; Ghiran, I.; Kelly Ciaran, P.; Ewoldt Randy, H.; McKinley Gareth, H.; So, P.; Erramilli, S.; Bansil, R., Helicobacter pylori moves through mucus by reducing mucin viscoelasticity. *Proceedings of the National Academy of Sciences* **2009,** *106* (34), 14321-14326.
266. Bansil, R.; Celli, J.; Chasan, B.; Erramilli, S.; Hong, Z.; Afdhal, N. H.; Bhaskar, K. R.; Turner, B. S., pH-dependent gelation of gastric mucin. *MRS Online Proceedings Library (OPL)* **2005,** *897*.
267. Paz, H. B.; Tisdale, A. S.; Danjo, Y.; Spurr-Michaud, S. J.; Argüeso, P.; Gipson, I. K., The role of calcium in mucin packaging within goblet cells. *Experimental eye research* **2003,** *77* (1), 69-75.
268. Han, S. K.; Jhun, B. H., Effect of additives on the cloud point of polyethylene glycols. *Archives of Pharmacal Research* **1984,** *7* (1), 1-9.
269. Ataman, M., Properties of aqueous salt solutions of poly (ethylene oxide). Cloud points, θ temperatures. *Colloid and polymer science* **1987,** *265* (1), 19-25.
270. Thiyagarajan, P.; Chaiko, D.; Hjelm Jr, R., A neutron scattering study of poly (ethylene glycol) in electrolyte solutions. *Macromolecules* **1995,** *28* (23), 7730-7736.
271. Button, B.; Goodell, H. P.; Atieh, E.; Chen, Y.-C.; Williams, R.; Shenoy, S.; Lackey, E.; Shenkute, N. T.; Cai, L.-H.; Dennis, R. G., Roles of mucus adhesion and cohesion in cough clearance. *Proceedings of the National Academy of Sciences* **2018,** *115* (49), 12501-12506.
272. Hammerschlag, M. R.; Harding, L.; Macone, A.; Smith, A. L.; Goldmann, D. A., Bacteriology of sputum in cystic fibrosis: evaluation of dithiothreitol as a mucolytic agent. *Journal of Clinical Microbiology* **1980,** *11* (6), 552-557.
273. Khutoryanskiy, V. V., Beyond PEGylation: alternative surface-modification of nanoparticles with mucus-inert biomaterials. *Advanced Drug Delivery Reviews* **2018,** *124*, 140-149.

274. Shan, W.; Zhu, X.; Tao, W.; Cui, Y.; Liu, M.; Wu, L.; Li, L.; Zheng, Y.; Huang, Y., Enhanced oral delivery of protein drugs using zwitterion-functionalized nanoparticles to overcome both the diffusion and absorption barriers. *ACS applied materials & interfaces* **2016,** *8* (38), 25444-25453.
275. Forstner, J.; Forstner, G., Effects of calcium on intestinal mucin: implications for cystic fibrosis. *Pediatric Research* **1976,** *10* (6), 609-613.
276. Verdugo, P.; Aitken, M.; Langley, L.; Villalon, M. J., Molecular mechanism of product storage and release in mucin secretion. II. The role of extracellular Ca ++. *Biorheology* **1987,** *24*, 625-633.
277. Raynal, B. D.; Hardingham, T. E.; Sheehan, J. K.; Thornton, D. J., Calcium-dependent protein interactions in MUC5B provide reversible cross-links in salivary mucus. *Journal of Biological Chemistry* **2003,** *278* (31), 28703-28710.
278. Ambort, D.; Johansson Malin, E. V.; Gustafsson Jenny, K.; Nilsson Harriet, E.; Ermund, A.; Johansson Bengt, R.; Koeck Philip, J. B.; Hebert, H.; Hansson Gunnar, C., Calcium and pH-dependent packing and release of the gel-forming MUC2 mucin. *Proceedings of the National Academy of Sciences* **2012,** *109* (15), 5645-5650.
279. Seisenberger, G.; Ried, M. U.; Endreß, T.; Büning, H.; Hallek, M.; Bräuchle, C., Real-Time Single-Molecule Imaging of the Infection Pathway of an Adeno-Associated Virus. *Science* **2001,** *294* (5548), 1929-1932.
280. Saxton, M. J.; Jacobson, K., Single-particle tracking: applications to membrane dynamics. *Annual review of biophysics and biomolecular structure* **1997,** *26*, 373-99.
281. De Gennes, P.-G.; Prost, J., *The physics of liquid crystals*. Oxford university press: 1993.
282. Miller, D. S.; Carlton, R. J.; Mushenheim, P. C.; Abbott, N. L., Introduction to optical methods for characterizing liquid crystals at interfaces. *Langmuir* **2013,** *29* (10), 3154-3169.
283. Modes, C. D.; Warner, M. In *The activated morphology of grain boundaries in nematic solid sheets*, Emerging Liquid Crystal Technologies VII, International Society for Optics and Photonics: 2012; p 82790Q.
284. Wang, X.; Miller, D. S.; Bukusoglu, E.; De Pablo, J. J.; Abbott, N. L., Topological defects in liquid crystals as templates for molecular self-assembly. *Nature materials* **2016,** *15* (1), 106-112.
285. McConney, M. E.; Martinez, A.; Tondiglia, V. P.; Lee, K. M.; Langley, D.; Smalyukh, I. I.; White, T. J., Topography from topology: photoinduced surface features generated in liquid crystal polymer networks. *Advanced Materials* **2013,** *25* (41), 5880-5885.
286. Wang, L.; Urbas, A. M.; Li, Q., Nature‐inspired emerging chiral liquid crystal nanostructures: from molecular self‐assembly to DNA mesophase and nanocolloids. *Advanced Materials* **2020,** *32* (41), 1801335.
287. Bai, Y.; Abbott, N. L., Recent advances in colloidal and interfacial phenomena involving liquid crystals. *Langmuir* **2011,** *27* (10), 5719-5738.
288. Koenig Jr, G. M.; Gettelfinger, B. T.; De Pablo, J. J.; Abbott, N. L., Using localized surface plasmon resonances to probe the nanoscopic origins of adsorbate-driven

ordering transitions of liquid crystals in contact with chemically functionalized gold nanodots. *Nano letters* **2008,** *8* (8), 2362-2368.
289. Koenig, G. M.; Lin, I.-H.; Abbott, N. L., Chemoresponsive Assemblies of Microparticles at Liquid Crystalline Interfaces. *Proc. Natl. Acad. Sci. U. S. A.* **2010,** *107* (9), 3998-4003.
290. Yang, K.-L.; Cadwell, K.; Abbott, N. L., Mechanistic study of the anchoring behavior of liquid crystals supported on metal salts and their orientational responses to dimethyl methylphosphonate. *the Journal of Physical Chemistry B* **2004,** *108* (52), 20180-20186.
291. Cadwell, K. D.; Alf, M. E.; Abbott, N. L., Infrared spectroscopy of competitive interactions between liquid crystals, metal salts, and dimethyl methylphosphonate at surfaces. *The Journal of Physical Chemistry B* **2006,** *110* (51), 26081-26088.
292. Cadwell, K. D.; Lockwood, N. A.; Nellis, B. A.; Alf, M. E.; Willis, C. R.; Abbott, N. L., Detection of organophosphorous nerve agents using liquid crystals supported on chemically functionalized surfaces. *Sensors and Actuators B: Chemical* **2007,** *128* (1), 91-98.
293. Fuster, H. A.; Wang, X.; Wang, X.; Bukusoglu, E.; Spagnolie, S. E.; Abbott, N. L., Programming van der Waals interactions with complex symmetries into microparticles using liquid crystallinity. *Science Advances* **2020,** *6* (25), eabb1327.
294. Bahukudumbi, P.; Bevan, M. A., Imaging Energy Landscapes using Concentrated Diffusing Colloidal Probes. *J. Chem. Phys.* **2007,** *126*, 244702.
295. Israelachvili, J. N., *Intermolecular and surface forces / Jacob N. Israelachvili*. Academic Press: London ; San Diego, 1991.
296. Allen, M. P.; Tildesley, D. J., *Computer simulation of liquids*. Oxford Science: New York, 1987.
297. Edwards, T. D.; Bevan, M. A., Polymer Mediated Depletion Attraction and Interfacial Colloidal Phase Behavior. *Macromolecules* **2012,** *45* (1), 585-594.
298. Wu, H.-J.; Pangburn, T. O.; Beckham, R. E.; Bevan, M. A., Measurement and Interpretation of Particle−Particle and Particle−Wall Interactions in Levitated Colloidal Ensembles. *Langmuir* **2005,** *21* (22), 9879-9888.
299. Israelachvili, J. N., *Intermolecular and Surface Forces* 2nd ed.; Academic Press: San Diego, 1991.
300. Ducker, W. A.; Senden, T. J.; Pashley, R. M., Measurement of Forces in Liquids Using a Force Microscope. *Langmuir* **1992,** *8* (7), 1831-1836.
301. Ducker, W. A.; Senden, T. J.; Pashley, R. M., Direct measurement of colloidal forces using an atomic force microscope. *Nature* **1991,** *353* (6341), 239-241.
302. Milling, A.; Mulvaney, P.; Larson, I., Direct Measurement of Repulsive van der Waals Interactions Using an Atomic Force Microscope. *J. Colloid Interface Sci.* **1996,** *460*, 460.
303. Lide, D. R., *CRC Handbook of Chemistry and Physics*. CRC Press: New York, 2000; Vol. 80.
304. Horn, R. G., Refractive indices and order parameters of two liquid crystals. *J. Phys. France* **1978,** *39* (1), 105-109.

305. Ratna, B. R.; Shashidhar, R., Dielectric Studies on Liquid Crystals of Strong Positive Dielectric Anisotropy. *Molecular Crystals and Liquid Crystals* **1977,** *42* (1), 113-125.
306. Brake, J. M.; Daschner, M. K.; Abbott, N. L., Formation and characterization of phospholipid monolayers spontaneously assembled at interfaces between aqueous phases and thermotropic liquid crystals. *Langmuir* **2005,** *21* (6), 2218-2228.
307. Gupta, J. K.; Abbott, N. L., Principles for Manipulation of the Lateral Organization of Aqueous-Soluble Surface-Active Molecules at the Liquid Crystal−Aqueous Interface. *Langmuir* **2009,** *25* (4), 2026-2033.
308. Mathai, K. G.; Ottewill, R. H., Stability of hydrophobic sols in the presence of non-ionic surface-active agents. Part 1.—Electrokinetic and adsorption measurements on silver iodide sols and suspensions. *Transactions of the Faraday Society* **1966,** *62* (0), 750-758.
309. Hunter, R. J., *Foundations of Colloid Science*. 2nd ed.; Oxford University Press: London, 2001.
310. Boles, M. A.; Engel, M.; Talapin, D. V., Self-Assembly of Colloidal Nanocrystals: From Intricate Structures to Functional Materials. *Chemical Reviews* **2016,** *116* (18), 11220-11289.
311. Uchida, S., Graft Copolymer Synthesis. In *Encyclopedia of Polymeric Nanomaterials*, Kobayashi, S.; Müllen, K., Eds. Springer Berlin Heidelberg: Berlin, Heidelberg, 2021; pp 1-4.
312. Pillay, V.; Seedat, A.; Choonara, Y. E.; du Toit, L. C.; Kumar, P.; Ndesendo, V. M. K., A review of polymeric refabrication techniques to modify polymer properties for biomedical and drug delivery applications. *AAPS PharmSciTech* **2013,** *14* (2), 692-711.
313. Rahane, S. B.; Hensarling, R. M.; Sparks, B. J.; Stafford, C. M.; Patton, D. L., Synthesis of multifunctional polymer brush surfaces via sequential and orthogonal thiol-click reactions. *Journal of Materials Chemistry* **2012,** *22* (3), 932-943.
314. Cao, Y.; Lai, Z.; Feng, J.; Wu, P., Graphene oxide sheets covalently functionalized with block copolymers via click chemistry as reinforcing fillers. *Journal of Materials Chemistry* **2011,** *21* (25), 9271-9278.
315. Cai, T.; Neoh, K.; Kang, E.; Teo, S., Surface-functionalized and surface-functionalizable poly (vinylidene fluoride) graft copolymer membranes via click chemistry and atom transfer radical polymerization. *Langmuir : the ACS journal of surfaces and colloids* **2011,** *27* (6), 2936-2945.
316. Binder, W. H.; Sachsenhofer, R., ‘Click’ chemistry in polymer and material science: an update. *Macromolecular Rapid Communications* **2008,** *29* (12‐13), 952-981.
317. Ogston, A. G.; Preston, B.; Wells, J., On the transport of compact particles through solutions of chain-polymers. *Proceedings of the Royal Society of London. A. Mathematical and Physical Sciences* **1973,** *333* (1594), 297-316.
318. Ogston, A.; Phelps, C., The partition of solutes between buffer solutions and solutions containing hyaluronic acid. *Biochemical Journal* **1961,** *78* (4), 827.

CURRICULUM VITAE

EDUCATION

Ph.D.

Aug. 2017 − Oct. 2022	Johns Hopkins University, Baltimore, MD
	Department of Chemical and Biomolecular Engineering
	Advisors: Prof. Michael A. Bevan

B.S.

Aug. 2013 − Aug. 2017	Smith College, Northampton, MA
	Department of Engineering Science
	Advisor: Susan Voss and Sarah J. Moore

AWARDS AND HONORS

Cum Laude 2017

PUBLICATIONS

Jumai'an, E.; E Garcia, M Herrera-Alonso; Bevan, M.A, (2020) Specific Ion Effects on Adsorbed Zwitterionic Copolymers. *Macromolecules.*
Jumai'an, E.; Ellingson M**.;** Bevan, M.A., (2022). kT-scale Repulsion between Polymer-Coated Colloids and Mucin. *manuscript in preparation for submission*.
Jumai'an, E.; Zhang, L.; Bevan, M.A., (2022). Blood Protein Exclusion from PEG Brushes. *manuscript in preparation for submission.*
Jumai'an, E.; Bevan, M.A., (2022). Blood Proteins Displace Zwitterionic Copolymers. *manuscript in preparation for submission.*
Hendley, R; Jumai'an, E.*; Fuster, H.; Abbott, N. Bevan, M.A (2022). Energy Landscapes on Polymerized Liquid Crystal Films. manuscript in preparation.
Song Y.; Lamberty Z.D; Liang J.; Pellitero M.A; Wagner J.A; **Jumai'an E.**; Bevan M.A; Frechette J; Arroyo-Currás N.; Katz H.E, (2021). *ACS Applied Nano Materials*.
Julia S. Kim, Allison R. Sirois, Vazquez Cegla A, **Jumai'an E.**, Murata N, Buck M, and Moore SJ, (2019). *Bioconjugate Chemistry*.
Lu H, Z Wang, Wilson BK, McManus S, **Jumai'an J.**, Padakanti P.K, Alavi A.A, Mach R.H, and Prud'homme R (2018). *ACS Applied Materials & Interfaces*.

**Co-first author*